2-Photon-Photoassociation spectroscopy in a mixture of Ytterbium and Rubidium

Inaugural-Dissertation

zur

Erlangung des Doktorgrades der

Mathematisch-Naturwissenschaftlichen Fakultät

der Heinrich-Heine-Universität Düsseldorf

vorgelegt von

Frank Münchow

aus Oldenburg i.O.

Mai 2012

Aus dem Institut für Experimentalphysik
der Heinrich-Heine-Universität Düsseldorf

Gedruckt mit der Genehmigung der
Mathematisch-Naturwissenschaftlichen Fakultät der
Heinrich-Heine-Universität Düsseldorf

Referent:	Prof. Dr. Axel Görlitz
Koreferent:	Prof. Dr. Dr. Carsten Müller
Tag der mündlichen Prüfung:	15.06.2012

Summary

Within the scope of this thesis, possible pathways to the production of Ytterbium-Rubidium (YbRb) molecules were examined by 1-Photon and 2-Photon-Photoassociation spectroscopy in laser-cooled mixtures of Yb and Rb. With the help of 1-Photon-Photoassociation experiments, detailed information about vibrational levels of different isotopes of the excited $^2\Pi_{1/2}$ state was gained. This information was needed for the 2-Photon-Photoassociation spectroscopy which examined the $^2\Sigma_{1/2}$ ground state of the YbRb molecule. The experimentally related Autler-Townes spectroscopy provided first experimental results on the transition strengths and therefore the overlap of the wavefunctions of ground and excited state molecular levels.

The experiments were performed at an apparatus that is designed for the study of YbRb mixtures and molecules and has been used in previous studies [1, 2, 3, 4]. The two atom species are held in a combined magneto-optical trap (MOT) which is continuously loaded. Approximately $4 \cdot 10^8$ Rubidium (Rb) atoms are held in this trap at a temperature of about 125 μK. The density is $6.8 \cdot 10^{10}\,\mathrm{cm}^{-3}$. The Ytterbium (Yb) trap holds much less atoms, namely about $2.4 \cdot 10^6$ atoms when no Rb is present. The Yb atoms have a temperature of about 400 μK at a density of $4.5 \cdot 10^9\,\mathrm{cm}^{-3}$ without Rb. Due to light-assisted collisions, we lose more than 95 % of the Yb atoms and end up with about $0.6 \cdot 10^5$ atoms when the combined trap is used.

In a so-called 1-Photon-Photoassociation (PA) process, two colliding atoms form an electronically excited molecule with the help of a photon. This was already perfomed in previous experiments [5, 3], where we investigated the excited $^2\Pi_{1/2}$ state of the isotopologue ^{176}Yb^{87}Rb and ^{174}Yb^{87}Rb near the Rb D_1 line at 795 nm. With the methods described by LeRoy and Bernstein [6], it was possible to describe a long-range potential $V(r) = C_6/r^6$ of this state with $C_6 = -(5684 \pm 98)\mathrm{E_h a_0^6}$. In the present thesis, we expanded our studies to two more isotopologues, namely ^{170}Yb^{87}Rb and ^{172}Yb^{87}Rb.

Precise knowledge of the energetic position of vibrational levels of the electronically excited state of the YbRb molecule is a prerequisite for the investigation of the electronic ground state by 2-Photon-PA spectroscopy which is the main part of this thesis. For this, the photoassociation laser that creates excited molecules out of two atoms is fixed on a resonance, so that a continuous molecular production is guaranteed. A probe laser is superimposed to the PA laser that induces light shift effects whenever it is on resonance with a molecular bound-bound transition. This leads to a lower molecular production rate and the atom number in the double-species MOT is increased.

In the experiments described in this thesis, the probe laser is slightly red detuned to the first one leading to a coupling between the fixed excited state and some vibrational levels of the molecular ground state. By this, we were able to determine the energetic position

of 6 vibrational levels[1] of the ground state for the isotopologue ^{176}Yb^{87}Rb. For the other isotopes, we investigated 2 resonances for each combination. This leads to altogether 18 molecular ground state levels for the YbRb molecule, for which 12 are in the $F = 1$ and 6 are in the $F = 2$ hyperfine ground state. The energetic positions of the vibrational levels made it possible to determine a C_6 value with the help of the LeRoy-Bernstein formula and to model a Lennard-Jones potential $V(r) = C_{12}/r^{12} + C_6/r^6$ that reproduces all of these levels where a C_{12} value is numerically determined:

$$C_6 = -(2563 \pm 50)\ \mathrm{E_h a_0^6},$$

$$C_{12} = 2.7412 \cdot 10^8\ \mathrm{E_h a_0^{12}}$$

This information about the ground state potential can be used to determine scattering properties, especially the s-wave scattering length to

$$a_{^{87}\mathrm{Rb},^{170}\mathrm{Yb}} = -5a_0$$

$$a_{^{87}\mathrm{Rb},^{172}\mathrm{Yb}} = -131a_0$$

$$a_{^{87}\mathrm{Rb},^{174}\mathrm{Yb}} = 1398a_0$$

$$a_{^{87}\mathrm{Rb},^{176}\mathrm{Yb}} = 225a_0.$$

In [4], we already examined scattering properties in a mixture of ^{87}Rb and different Yb isotopes through thermalization experiments. We got very peculiar findings for the s-wave scattering length in two isotopes. In a mixture of ^{170}Yb and ^{87}Rb, nearly no interaction between the two species was measured. This means that the s-wave scattering length has a value near zero. In ^{174}Yb and ^{87}Rb, the complete opposite happens [7]: The two atom species showed a nearly immediate thermalization and separated spatially. This means, that the s-wave scattering length is huge. These findings for the mixtures of ^{87}Rb and ^{170}Yb respective ^{87}Rb and ^{174}Yb are reproduced in the calculations as expected.

The long term goal of this experiment is the creation of YbRb molecules in the rovibrational ground state. For this, a 2-step process is favorable: First, weakly bound ground state molecules are produced. This can be done either with a 2-Photon process where the positions of the resonances are needed which have been measured in this thesis. Another possibility is to use magnetic Feshbach resonances. Until 2010, it was commonly believed that there is a neglible coupling between different hyperfine ground state levels in mixtures of alkali and earth-alkaline like metals which do not lead to usable magnetic Feshbach resonances. But in [8, 9], it was theoretically shown, that a weak coupling exists and may be used to form Feshbach molecules. In this thesis, this possibility for YbRb molecules will be discussed and possible positions of the magnetic Feshbach resonances will be given. This offers a second path for weakly bound ground state molecules.

In a next step, these weakly bound ground state molecules have to be transferred to the absolute ground state. For this, a 2-Photon process seems to be favorable, as already

[1] Each vibrational state consists of two resonances, one for each hyperfine state of ^{87}Rb.

demonstrated for KRb [10]. A discussion of possible transitions in the molecule will round up this thesis.

In addition to the work on YbRb, I have performed investigations on mixtures of Lithium and Ytterbium (LiYb) in an exchange stay at the university of Washington in Seattle. In this experiment, the two species were cooled and trapped in a combined magneto-optical trap and then transferred into an optical dipole trap, created by a focussed laser beam. During my stay, we examined the scattering properties of Li and Yb and determined the s-wave scattering length of the mixture ^{6}Li and ^{174}Yb to [11]

$$\left|a_{^6\mathrm{Li},^{174}\mathrm{Yb}}\right| = (13 \pm 3)\, a_0.$$

Zusammenfassung

Im Rahmen dieser Arbeit wurden in einem lasergekühlten Gemisch aus Ytterbium und Rubidium mit Hilfe der 1-Photon und 2-Photon-Photoassoziationsspektroskopie mögliche Wege zur Erzeugung von Ytterbium-Rubidium (YbRb) Molekülen untersucht. Detaillierte Informationen über den elektronisch angeregten $^2\Pi_{1/2}$ Zustand wurde mit Hilfe der 1-Photon-Photoassoziation gewonnen. Diese Information ist notwendig für die Untersuchung des $^2\Sigma_{1/2}$ Grundzustands des YbRb Moleküls mittels 2-Photonen-Photoassoziation. Das experimentell ähnliche Verfahren der Autler-Townes Spektroskopie wurde angewandt, um erste experimentelle Ergebnisse über die Übergangwahrscheinlichkeiten und damit dem Überlapp der Wellenfunktionen der beteiligten molekularen Zustände zu erhalten.

Die beschriebenen Experimente wurden an einer Apparatur durchgeführt, an der schon mehrere Forschungsprojekte an Ytterbium-Rubidium Mischungen und Molekülen durchgeführt wurden [1, 2, 3, 4]. Die beiden Atomsorten werden in einer kombinierten magneto-optischen Falle (MOT) gefangen, in der die Atome kontinuierlich geladen werden. Hierin werden ca. $4 \cdot 10^8$ Rubidium (Rb) Atome mit einer Temperatur von etwa 125 μK gefangen. Die Dichte beträgt $6,8 \cdot 10^{10}$ cm^{-3}. In der Falle für Ytterbium (Yb) werden etwa $2,4 \cdot 10^6$ Atome gefangen, wenn kein Rubidium genutzt wird. Die Temperatur der Yb-Atome beträgt hierbei etwa 400 μK bei einer Dichte von $4,5 \cdot 10^9$ cm^{-3}. Aufgrund von Kollisionen von Rb mit angeregten Yb Atomen, verlieren wir mehr als 95 % der Yb Atome und erhalten somit etwa $0,6 \cdot 10^5$ Atome in der kombinierten Falle.

Bei der sogenannten 1-Photon-Photoassoziation bilden zwei kollidierende Atome mit Hilfe eines Photons ein elektronisch angeregtes Molekül. Diese Technik wurde in einem früheren Experiment [3, 5] schon durchgeführt, wobei dort der angeregte Zustand $^2\Pi_{1/2}$ der Isotope ^{174}Yb^{87}Rb und ^{176}Yb^{87}Rb untersucht wurde in der Nähe der Rb D_1-Linie bei 795 nm. Mit den Methoden von LeRoy und Bernstein [6] war es möglich, das langreichweitige Potential $V(R) = C_6/r^6$ von diesem Zustand mit $C_6 = -(5684 \pm 98)\,\mathrm{E_h a_0^6}$ zu beschreiben . In dieser Arbeit wurde dieses Experiment erweitert um die zwei weiteren Isotope ^{170}Yb^{87}Rb und ^{172}Yb^{87}Rb.

Die Position der angeregten molekularen Zustände ist eine notwendige Information für den nächsten Schritt, bei dem der Grundzustand untersucht wird. Dafür wurde der Photoassoziationslaser auf eine 1-Photon-Resonanz frequenzstabilisiert, so dass kontinuierlich Moleküle erzeugt werden. Ein zweiter Laser wird mit dem ersten Laser überlagert. Dieser induziert eine Verschiebung der molekularen Zustände, wenn er resonant mit einem gebundenen Molekülübergang ist. Dies führt zu einer niedrigeren Molekülrate und somit zu mehr Atomen in der MOT.

In den Experimenten, die in dieser Arbeit beschrieben werden, ist der zweite Laser rotverstimmt gegenüber dem ersten Laser und der molekulare Grundzustand wird unter-

sucht. Auf diese Art haben wir 6 verschiedene Vibrationszustände[2] des Grundzustands des ^{176}Yb^{87}Rb Moleküls gefunden. Für die anderen Isotope haben wir jeweils zwei Resonanzen gefunden. Insgesamt wurden 18 Resonanzen gefunden, von denen wir 12 dem $F = 1$ und 6 dem $F = 2$ Hyperfeinzustand zuordnen konnten. Mit dieser Information war es möglich, einen C_6 Koeffizienten mit Hilfe der LeRoy-Bernstein Formel [6] zu bestimmen und ein Lennard-Jones Potential $V(r) = C_{12}/r^{12} + C_6/r^6$ zu modellieren, welches alle gefundenen Zustände reproduziert. Dabei wurde der C_{12} Koeffizient numerisch bestimmt:

$$C_6 = -(2563 \pm 50)\ \mathrm{E_h a_0^6},$$

$$C_{12} = 2.7412 \cdot 10^8\ \mathrm{E_h a_0^{12}}$$

Diese Information über den Grundzustand kann dazu genutzt werden, um das Streuverhalten und insbesondere die s-Wellen Streulänge der verschiedenen Isotope zu bestimmen:

$$a_{^{87}\mathrm{Rb},^{170}\mathrm{Yb}} = -5a_0$$

$$a_{^{87}\mathrm{Rb},^{172}\mathrm{Yb}} = -131a_0$$

$$a_{^{87}\mathrm{Rb},^{174}\mathrm{Yb}} = 1398a_0$$

$$a_{^{87}\mathrm{Rb},^{176}\mathrm{Yb}} = 225a_0$$

In einem früheren Experiment [4] haben wir bereits das Streuverhalten in einem Gemisch aus ^{87}Rb und verschiedenen Yb Isotopen mittels Thermalisierung untersucht. Hierbei bekamen wir erstaunliche Ergebnisse für zwei Isotope: In ^{170}Yb und ^{87}Rb wurde (fast) keine Interaktion zwischen den Spezies festgestellt. Das bedeutet, dass die s-Wellen Streulänge einen Wert nahe Null haben muss. In ^{174}Yb und ^{87}Rb passiert das genaue Gegenteil: Die beiden Sorten thermalisieren nahezu instantan und es tritt eine örtliche Trennung auf. Diese bedeutet, dass die s-Wellen Streulänge sehr groß sein muss. Diese Erkenntnisse für ^{87}Rb und ^{170}Yb beziehungsweise für ^{87}Rb und ^{174}Yb wurden in den berechneten Werten für die s-Wellen Streulänge reproduziert.

Das langfristige Ziel dieses Experiments ist die Erzeugung von ultrakalten YbRb Molekülen im absoluten Grundzustand. Dafür sind zwei Schritte notwendig: Im ersten Schritt werden schwach gebundene Grundzustandsmoleküle erzeugt. Das kann durch einen 2-Photonen-Prozess geschehen. Hierzu sind die genauen Positionen der Resonanzen notwendig, die in dieser Arbeit gemessen wurden. Eine andere Möglichkeit ist die Nutzung sogenannter magnetischer Feshbach Resonanzen. Bis 2010 wurde allgemein angenommen, dass in einem Gemisch aus einem Alkali und einem erdalkaliähnlichem Metall die Kopplung zwischen den Hyperfeinzuständen im Grundzustand zu schwach ist, so dass solche Resonanzen nicht existieren. In [8, 9] wurde jedoch theoretisch gezeigt, dass eine schwache Kopplung zwischen den Hyperfeinzuständen des Grundzustands existiert, die ausreichend ist, um Feshbach Moleküle zu erzeugen. Innerhalb dieser Arbeit wird diese Möglichkeit für

[2] Zu jedem Vibrationszustand wurden zwei Resonanzen gefunden, gemäß dem Hyperfeinsplitting des ^{87}Rb Grundzustands.

das YbRb Molekül diskutiert und mögliche Positionen dieser Resonanzen angegeben. Dies ermöglicht einen weiteren Weg für die Erzeugung schwach gebundener Moleküle.

Im nächsten Schritt werden diese Moleküle in den absoluten Grundzustand transferiert. Hierzu scheint ein 2-Photonen-Prozess die beste Möglichkeit zu sein, wie in Experimenten mit KRb [10] schon erfolgreich gezeigt wurde. Eine Diskussion über mögliche Übergänge runden diese Arbeit ab.

Zusätzlich zu meiner Arbeit an YbRb habe ich ein Gemisch aus Lithium und Ytterbium während eines Austausches mit der University of Washington in Seattle untersucht. In der Gruppe dort werden die beiden Sorten lasergekühlt und anschließend in eine durch einen fokussierten Laserstrahl erzeugte optische Dipolfalle umgeladen. Während meines Aufenthaltes haben wir das Streuverhalten der beiden Atomsorten untersucht und mittels Thermalisierung die s-Wellen Streulänge für ein Gemisch aus ^{6}Li und ^{174}Yb bestimmt zu [11]

$$\left|a_{^6\mathrm{Li},^{174}\mathrm{Yb}}\right| = (13 \pm 3)\, a_0.$$

Contents

1.

Introduction

The long term goal of the research project in which the work for the present thesis was performed is the creation of ultracold Ytterbium-Rubidium molecules in the rovibrational ground state. For this, a 2-step process is favorable. In a first step, weakly bound ground state molecules are produced which are transferred to the absolute ground state in a second step. In this thesis, the first investigations of the ground state potential of the YbRb molecule will be presented that are crucial for the creation of ground state molecules.

This introduction will give an overview of the field of ultracold atoms and molecules. In alkali-alkali mixtures, ultracold molecules in the absolute ground state have already been produced. Current research projects and their path to the absolute ground state will be presented.

Ultracold atoms

The realization and development of slowing [12, 13] and cooling [14] atoms with lasers opened the path for the field of ultracold atomic gases in the 1980s. These techniques allowed the cooling and trapping of an atomic cloud at temperatures below 1 mK. With evaporative cooling [15], it was possible to cool even further down to temperatures in the nK regime. This led in 1995 to the first experimental realization of Bose-Einstein condensates (BEC) in ^{87}Rb [16], ^{23}Na [17] and ^{7}Li [18], a new state of matter predicted already in the 1920s by Einstein and Bose [19]. A lot of new fascinating experiments are now accessible with this technique and consequently, these milestones of laser cooling and trapping and the achievement of a BEC were rewarded with the Nobel prizes in 1997 [20] and 2001 [21].

The number of elements and isotopes that have been cooled to quantum degeneracy has been expanding since then. In 2003 [22], a BEC of Ytterbium atoms was reported.

Ultracold molecules

Due to the complicated internal structure, the known laser cooling techniques can not be used in molecules or only in very rare special cases as demonstrated recently in SrF [23]. Therefore, another path must be used. One possible way is to first cool the atoms species with the known techniques and then convert these atoms to molecules. Here, two methods are possible: the use of magnetic Feshbach resonances [24] or photoassociation [25].

Feshbach resonances make use of the effect that with the help of a homogeneous magnetic field, the energy levels of an atom or molecule are shifted. When a bound molecular level

and the open channel of two free atoms are at the same energy level, a resonance occurs if a coupling between these states exist. This so-called magnetic Feshbach resonance can be used to form molecules out of the two atoms by adiabatically varying the magnetic field across the resonance. Feshbach resonances were first observed in 1998 at ^{85}Rb [26] and ^{23}Na [27]. A lot of experiments nowadays use Feshbach resonances to create weakly bound molecules [24]. In heteronuclear mixtures, magnetic Feshbach resonances were first observed in 2004 in KRb [10] and LiNa [28]. Recently [8, 9], it was proposed, that magnetic Feshbach resonances could also be accessible in mixtures of an alkali metal (like Rb) and an earth-alkaline like metal (like Yb). This opens the path for systems such as RbYb to create molecules in the rovibrational ground state also via Feshbach resonances.

A second way to create molecules is the use of photoassociation [29]. Here, two colliding atoms can form an electronically excited molecule with the help of a photon. The difference of the energy of the red-detuned photon to the atomic transition energy is the binding energy of the molecule. This excited molecule will emit a photon after a short time and decay into a ground state molecule or two free atoms [30]. The first observation of ground state molecules (although in a high vibrational level) produced in this way was in 1998 in Cs [31].

The creation of ground state molecules in a well-defined state is in principle possible with 2 photons. The frequency difference of these two photons is equivalent to the binding energy of the molecule. With a so-called Stimulated Raman Adiabatic Passage (STIRAP) process, atoms could thus be converted coherently into a defined molecular state [30] although it is very challenging experimentally to convert two free atoms to molecules and is not shown yet.

The next step is to transfer the weakly bound molecules to the rovibrational ground state. The successful experiments in this direction use a STIRAP process to do this. In an experiment in Innsbruck [32], Rb atoms are first associated via magnetic Feshbach resonances to a weakly bound molecule and then transferred with a STIRAP process to the absolute ground state. The same method was used in Cs_2 [33]. In heteronuclear mixtures, the absolute ground state was achieved in KRb [34]. The molecules are produced via a Feshbach resonance to weakly bound molecules and then transferred with a STIRAP process to the absolute ground state.

In an experiment with Rb and Cs [35, 36], a 1-Photon-photoassociation process was performed to create excited RbCs* molecules. These molecules decay prominently in one specific molecular ground state. These weakly bound molecules are then transferred to an intermediate excited state and driven to the vibrational ground state by stimulated emission, but not the rotational ground state.

A different approach is possible in experiments with LiCs [37], where the ground state was achieved with only 1 photon: The overlap of the used vibrational level of the excited state and the absolute ground state is high enough that the molecule will spontaneous emit to the ground state.

Polar molecules

Quantum degeneracy has been reached in dipolar atomic gases in chromium [38] and recently in dysprosium [39]. The atoms offer a relatively weak magnetic dipolar interaction. In contrast, polar molecules like YbRb have an internal electric dipole moment which leads to a large dipole-dipole interaction between molecules. However, the degeneracy has not been reached yet in the absolute ground state.

The long-range and anisotropic interactions add new aspects to the physics of ultracold quantum matter [40, 41]. The electric dipole moments can be precisely controlled via the strength and the orientation of an electric field. This offers the basis for a lot of theoretical proposals e.g. in quantum information processing [42, 43], new quantum phases [44] or its transitions [45, 46] and quantum control with external electric and/or magnetic fields [47]. Polar molecules are also a possible candidate for probing fundamental physical symmetries, e.g. the search of a permanent electric dipole moment of the electron where the internal electric field amplifies the effect. Ongoing measurements are performed in YbF molecules [48, 49], but this was recently also discussed for the case of YbRb [50].

Additionally, the study of chemical reactions in the ultracold regime was investigated in [51]. Here, quantum mechanics play an important role: The prepared ultracold fermionic molecules $^{40}K^{87}Rb$ in different spin states will undergo the exothermic chemical reaction $KRb + KRb \rightarrow K_2 + Rb_2$ with an enhancement factor of up to 100 in comparison to molecules in the same internal state due to its fermionic nature where only p-wave collisions are possible when the molecules are identical. In many experiments, exothermic reactions like this are not a desired effect. By placing the molecules in an optical lattice [52] or by creating repulsive interaction between the molecules with electric fields [53], the exothermic reaction can be prevented.

Paramagnetic heteronuclear molecules like YbRb, also allow the realization of lattice-spin-models [54] where the polar molecules are stored in an optical lattice representing a state of matter with topological order. The spin is represented by the single valence electron. This model is proposed to be used e.g. as a quantum memory in quantum computing.

This thesis

The experiments presented in this thesis are the first investigations of the ground state potential in a molecule consisting of an alkali and a rare earth metal. This system has in contrast to the mostly used alkali-alkali mixtures a paramagnetic ground state that can be trapped magnetically and due to its unpaired electron, it can be used in many investigations as discussed before.

In photoassociation experiments, we created molecules in the excited state. First investigations of this were already performed in [3, 5], but are expanded to two more bosonic isotopes of Ytterbium within the present work. We also performed first RbYb photoassociation experiments near the D_2 line of Rb at 780 nm. With the second photoassociation laser, information about the ground state potential of YbRb was gained where only ab-initio calculations [55] exist until now. In this thesis, the determination of 18 weakly bound

vibrational levels of the ground state in different isotopologues will be described and a possible potential for the ground state is shown that reproduces all of the found vibrational levels. With this information, it is possible to show a path on how to create rovibrational ground state molecules.

This thesis begins with a short review of laser cooling and trapping and some basic concepts of molecular physics (chapter 2). Chapter 3 explains the setup of our experiment and the data acquisition methods. The 1-Photon-Photoassociation spectra and resonances are presented in chapter 4 which gives information about the excited state $^2\Pi_{1/2}$. The ground state potential and the corresponding results from the 2-Photon-Photoassociation experiments are described in chapter 5. Autler-Townes spectroscopy was performed on some transitions giving information about the transition strength and is described in chapter 6. Future experiments involving the creation of Feshbach molecules with a calculation of possible Feshbach resonances are presented in chapter 7 and an outlook for possible paths to the rovibrational ground state will be given in chapter 8.

In appendix B, I will present the results that were performed during a half-year stay at the Li-Yb experiment at the University of Washington in Seattle.

2.

Basic experimental and theoretical concepts

In this chapter, the basic concepts of cooling and trapping of atoms are briefly summarized. In our experiment, we use Zeeman slowers for deceleration and trap the atoms in magneto-optical traps which are based on the principle of laser cooling.

Additionally, a short introduction to molecular physics, especially the diatomic case, will be given. This approach is only a short outline of the whole area. There are plenty of textbooks that explain it in detail, e.g. [56, 57, 58].

2.1. Cooling and trapping of atoms

A photon scattering process transfers momentum to atoms. That is the basic principle of laser cooling. The resulting force on the atom depends on the momentum $\hbar\vec{k}$ and the scattering rate Γ [56]:

$$\vec{F} = \hbar\vec{k}\Gamma \tag{2.1}$$

Here, $\vec{k}$ is the wavevector of the involved light field. The wavenumber $\left|\vec{k}\right| = 2\pi/\lambda$ depends on the wavelength λ of the scattered photon. The scattering rate Γ is defined as [56]

$$\Gamma = \frac{\gamma}{2}\frac{S_0}{1 + S_0 + (2\delta/\gamma)^2} \tag{2.2}$$

where γ is the linewidth of the atomic transition. The saturation parameter S_0, defined as $S_0 = I/I_{\mathrm{sat}}$, includes the intensity of the light field I and the saturation intensity [56]

$$I_{\mathrm{sat}} = \frac{\pi hc}{3\lambda^3\tau} \tag{2.3}$$

with λ being the wavelength of the atomic transition and τ being the lifetime of the excited state. This is a value specific for a given atomic species and transition. Important values for our setup are shown in tab. 2.1. For a maximized scattering rate, it is crucial that the detuning δ from the light field to the atomic transition is small and ideally zero. Due to the velocity of the atoms, they experience a Doppler shift which makes the light field red detuned. This shift will vary during the deceleration and can be compensated e.g. by a varying magnetic field.

atomic transition	wavelength λ	linewidth γ	I_{sat}
Rb $^2S_{1/2} \rightarrow^2 P_{1/2}$	795 nm	$2\pi 5.75$ MHz [59]	$1.49\,\mathrm{mW/cm^2}$
Rb $^2S_{1/2} \rightarrow^2 P_{3/2}$	780 nm	$2\pi 6$ MHz [59]	$1.65\,\mathrm{mW/cm^2}$
Yb $^1S_0 \rightarrow^1 P_1$	399 nm	$2\pi 28$ MHz [60]	$57.61\,\mathrm{mW/cm^2}$
Yb $^1S_0 \rightarrow^3 P_1$	556 nm	$2\pi 181$ kHz [60]	$0.14\,\mathrm{mW/cm^2}$

Table 2.1.: *Saturation intensities for important transitions that are used in our experimental studies.*

2.1.1. Zeeman slower

In a trap for ultracold atoms, only slow atoms can be trapped. For that, we use a Zeeman slower that slows down atoms with a velocity lower than a maximum velocity v_0. During that process, the atoms are also cooled. In a typical setup, the slowing laser beam is directed in opposite direction as the atomic beam.

The detuning δ depends on the atomic transition δ_0 and on additional effects like the Doppler shift and magnetic fields[1]:

$$\delta = \delta_0 - \vec{k} \cdot \vec{v} - \frac{\mu' B}{\hbar} \tag{2.4}$$

Here, $\vec{k}$ is again the wavevector of the light field, $\vec{v}$ is the velocity of the atoms and B is the magnetic field with $\mu' = (g_\mathrm{e} m_\mathrm{e} - g_\mathrm{g} m_\mathrm{g})\,\mu_\mathrm{B}$ being the effective magnetic moment with the Landé g-factors g_i and the magnetic quantum numbers m_i of the ground and excited state.

In the process of slowing, the velocity of the atoms changes significantly and thus, the detuning δ is changing. This can be compensated by a spatially varying magnetic field which is the basic idea of a Zeeman slower. For high intensities $I \gg I_{\mathrm{sat}}$ and zero detuning, the maximal deceleration is [56]

$$|a_{\max}| = \frac{F_{\max}}{m} = \frac{\gamma}{2}\frac{\hbar k}{m}. \tag{2.5}$$

The velocity during the slowing process is then $v(z) = \sqrt{v_0^2 - 2\,|a_{\max}|\,z}$. The maximal force is reached with the condition $\delta = 0$. The required magnetic field can be calculated from (2.4) as:

$$B(z) = \frac{\hbar}{\mu'}\left(\delta_0 + k\sqrt{v_0^2 - 2\,|a_{\max}|\,z}\right) \tag{2.6}$$

This magnetic field describes an increasing field geometry Zeeman slower as it is used in our experimental setup (see fig. 2.1). In this configuration, the slowing beam works at a detuning $\delta = -kv_0$ to be resonant with the fast atoms at zero field. This has the advantage, that the slowing beam is not resonant with slow and cold atoms that are held in the trap. Details on the Zeeman slower in our experimental setup can be found in [1, 2, 61].

[1] There are additional effects on the detuning (e.g. electric fields) that should not be considered here.

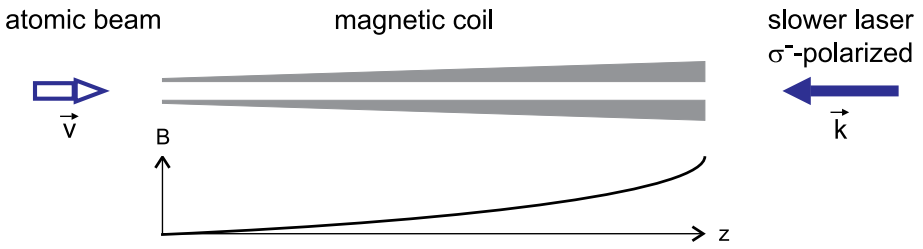

Figure 2.1.: *Principle of Zeeman slowing. The slowing laser beam is directed in the opposite direction of the atomic beam. In the region where the atoms are slowed, an increasing magnetic field is compensating the Doppler shift. Adapted from [2].*

2.1.2. Optical molasses

A set of six pairwise counterpropagating laser beams form an optical molasses [62]. The atoms experience a force proportional to their velocity. In a one-dimensional picture, the forces for the two counterpropagating beams are [56]

$$\vec{F_{\pm}} = \pm\hbar\vec{k}\frac{\gamma}{2}\frac{S_0}{1+S_0+\left(\frac{2(\delta\mp kv)}{\gamma}\right)^2}. \tag{2.7}$$

The total force is the sum of the two parts and acts as a damping force [56]:

$$\vec{F_{\mathrm{OM}}} = \vec{F_{+}} + \vec{F_{-}} = -\beta\vec{v} \tag{2.8}$$

For red detuned laser light ($\delta < 0$), this force damps the atomic motion with

$$\beta = \frac{8\hbar k^2\delta S_0}{\gamma\left(1+S_0+\left(\frac{2\delta}{\gamma}\right)^2\right)^2}. \tag{2.9}$$

This method slows down and cools the atom with the Doppler cooling limit

$$T_{\mathrm{D}} = \frac{\hbar\gamma}{2k_{\mathrm{B}}}. \tag{2.10}$$

This limit determines the lowest achievable temperature and is caused by the need of emission and absorption of photons. This temperature is typically on the order of about 100 μK.

2.1.3. Magneto-optical trap

By adding a magnetic quadrupole field to the laser field, a spatial dependence of the force can be reached and therefore the atoms can be trapped in the center of the magnetic field. Fig. 2.2 shows the basic principle of an one dimensional MOT in the case of Yb. The MOT uses the transition $|^1S_0, J = 0\rangle \rightarrow |^1P_1, J = 1\rangle$. Due to the increasing magnetic field $B(z) = B_0 z$, the upper state splits up into the three Zeeman subcomponents with

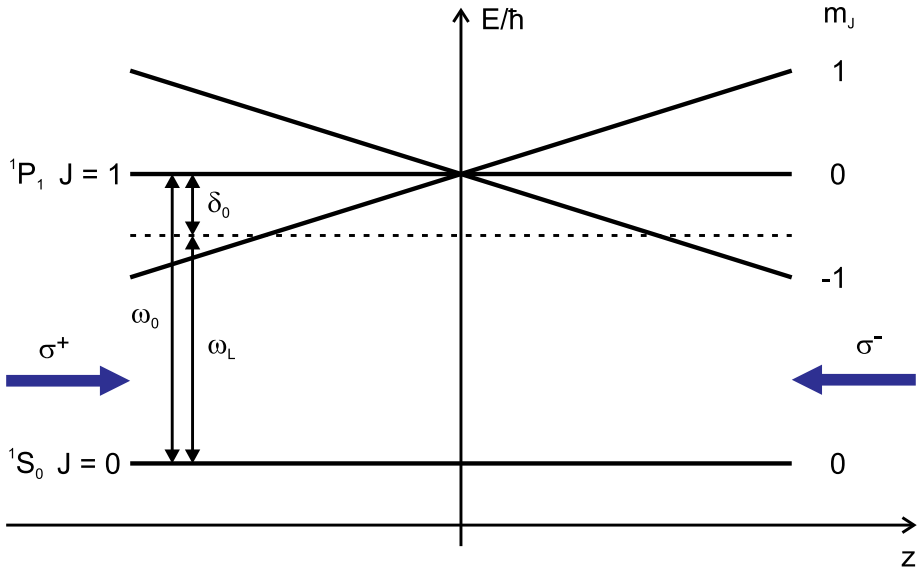

Figure 2.2.: *Basic principle of a MOT in one-dimensional case. The counterpropagating lasers with circular polarization are red detuned from the atomic transition and a spatial varying magnetic field $B(z) = B_0 z$ is applied leading to a splitting into three Zeeman subcomponents of the upper state. Adapted from [2].*

the quantum numbers $m_J = -1, 0, +1$. The MOT beams are circular polarized and red detuned to the atomic transition without magnetic field (represented as the dashed line in the figure). The Zeeman shift due to the magnetic field tunes the $m_J = -1$ component closer to the laser detuning for $z > 0$. Thus, more of the laser light in σ^- polarization is scattered at $z > 0$ leading to a force in the direction of this beam which is the trapping center. For $z < 0$, the same happens for the $m_J = +1$ component and the σ^+ polarized laser light, leading to a force in direction of the trapping center. The total force can be calculated to [56]

$$\vec{F_{\mathrm{MOT}}} \approx \frac{8\hbar k \delta S_0 \vec{v}}{\gamma\left(1 + S_0 + \left(\frac{2\delta}{\gamma}\right)^2\right)^2} + \frac{\mu' B_0}{\hbar} \frac{8\hbar k \delta S_0 \vec{r}}{\gamma\left(1 + S_0 + \left(\frac{2\delta}{\gamma}\right)^2\right)^2} = -\beta\vec{v} - \kappa\vec{r}. \quad (2.11)$$

In this kind of trap called magneto-optical trap (MOT), all atoms with a maximum velocity $v_c = \sqrt{2 r_c \hbar k \gamma / m}$ can be captured in a trap of the radius r_c. To increase the fraction of atoms that will be trapped, many experiments including the one described here use a Zeeman slower to slow down the atoms which then will be captured by the MOT. More on optical molasses and magneto-optical traps (MOT) can be found in [63, 64, 65, 66, 67, 68].

With the help of different techniques e.g. the polarization gradient cooling [69], it is possible to cool atoms below the Doppler limit.

2.1.4. Conservative traps for atoms

The absorption and emission of (near resonant) photons limit the density and the temperature in a MOT. To avoid these effects, different types of traps exist which do not depend on light scattering. A purely magnetic trap [70, 71] uses magnetic fields and its interaction with neutral atoms. This kind of trap only works with paramagnetic atoms like Rb. A magnetic field $\vec{B}$ shifts the energy of an atom with a magnetic moment $\vec{\mu}$:

$$\Delta E = -\vec{\mu} \cdot \vec{B} = g_{\mathrm{F}} m_{\mathrm{F}} \mu_{\mathrm{B}} \left| \vec{B} \right| \tag{2.12}$$

where g_{F} is the Landé g-factor of a state in the hyperfine level F with the magnetic quantum number m_{F}. For atoms with $g_{\mathrm{F}} m_{\mathrm{F}} > 0$, an energy minimum exists at the position of the magnetic minimum where atoms can be trapped. In an Ioffe-Pritchard-trap [72], a magnetic trap is realized by a quadrupole field and an offset field. Further cooling is possible for example through evaporative cooling: By lowering the potential, the hottest atoms are lost from the trap. The rest of the atoms then thermalizes and get colder. By this technique, temperatures below degeneracy can be reached [15].

Yb has a diamagnetic ground state and can therefore not be trapped in a magnetic trap[2]. But atoms can also be trapped in an inhomogeneous electromagnetic field, e.g. a focused laser beam [74]. An electric field $\vec{E}$ with a frequency ω induces a rapidly oscillating atomic dipole moment $\vec{p} = \alpha(\omega)\vec{E}(\vec{r})$ where α is the complex polarizability. This can be calculated [75]:

$$\alpha(\omega) = 6\pi\epsilon_0 c^3 \frac{\gamma/\omega_0^2}{\omega_0^2 - \omega^2 - i\left(\omega^3/\omega_0^2\right)\gamma)} \tag{2.13}$$

Here, ω_0 is the transition frequency and γ the linewidth of an ideal two-level atom. The potential U_{dip} is given by [75]

$$U_{\mathrm{dip}} = -\frac{1}{2}\left\langle \vec{p}\vec{E} \right\rangle = -\mathrm{Re}(\alpha)\left|\vec{E}(\vec{r})\right|^2. \tag{2.14}$$

The dipole force on an atom is then given by

$$\vec{F}_{\mathrm{dip}}(\vec{r}) = -\nabla U_{\mathrm{dip}}(\vec{r}). \tag{2.15}$$

Thus, a red-detuned laser field ($\omega < \omega_0$) creates a potential minimum at a light field maximum, which can be created by a focus in a laser beam. An optical trap is independent of magnetic fields, therefore this is the preferable trap geometry for future experiments on Feshbach resonances (see chap. 7).

By overlapping two laser beams with two different frequencies, it is possible to design optical potentials for Rb and Yb almost independently: The main transitions of Rb are at 780 nm and 795 nm. A laser beam with a wavelength of 1064 nm creates a potential minimum at the position of the focus of a laser beam while the superimposed laser with a wavelength of 532 nm creates a potential maximum. For Yb, both lasers create potential

[2] It is possible to use metastable excited states in Yb where magnetic trapping could be done, for example in the $|^3P_2\rangle$ state [73].

minima in the focus because the main transition of Yb is at 399 nm. Thus, it is possible to adjust the trap depth for the two species independently. More on this trapping geometry can be found in [2, 4].

2.2. Molecules

In this section, I follow the treatment of [58, 76]. Two atoms start interacting when they are brought close enough together. At large distances, the electronic structure of each atom is not changed, but Van-der-Waals interactions and dipole-dipole forces are playing a role. The general potential, where all possible interactions are taken into account is approximately

$$V(r) \approx E_{\mathrm{D}} + \sum_n \frac{C_{\mathrm{n}}}{r^n} \tag{2.16}$$

where E_{D} is the dissociation limit of the potential and C_n are the specific parameters for the potential. In the homonuclear case, that means when both atoms are identical, the long-range potential can be described with a C_3 coefficient. For some specific electronic states, e.g. both atom are in an electronic P state, the potential can be described by a C_5 coefficient [77]. In a (normal) heteronuclear potential, all C_{n} with $n < 6$ are zero in the long-range regime. The potential is then described by C_6/r^6 for large interatomic distances.

Short-range interactions include change of the electronic wavefunction of an atom due to the presence of the second nucleus and Van-der-Waals forces leading to a repulsive potential which can be approximated at first order in the heteronuclear case to the Lennard-Jones potential [78]

$$V(r) \approx E_{\mathrm{D}} + C_{12}/r^{12} + C_6/r^6. \tag{2.17}$$

In this definition, C_6 is negative and C_{12} has to be positive.

A second form which is often used to describe a molecular potential, was introduced by Morse [79], which is giving good results in the short range:

$$V(r) \approx E_{\mathrm{D}} \cdot \left(1 - e^{-\sqrt{\frac{\mu}{2E_D}}\omega_e \cdot (r - R_e)}\right)^2 \tag{2.18}$$

where R_e is the distance of the two atoms with the lowest potential energy and ω_e is a characteristic constant for the molecule.

Sørensen et al. performed high-level four-component coupled cluster calculations of the RbYb potential in 2009 [55]. This made a first assumption of the RbYb potential possible. They calculated a Morse potential (see tab. 2.2 for details) for 4 different electronic states of the molecule. Fig. 2.3 shows the calculated potentials. The ab-initio calculations are very time consuming and up to now they do not agree with the known limiting cases of separated atoms. But the available potentials should represent the shape and the features of the real potentials in a good approximation. More precise calculations are only possible

state	$\Lambda - \Sigma$	R_e (bohr)	ω_e (cm^{-1})	E_D (cm^{-1})
1 0.5 (ground state)	$^2\Sigma^+$	8.85	29.751	865
2 0.5	$^2\Pi$	7.40	69.294	7735
1 1.5	$^2\Pi$	7.43	69.322	7164
3 0.5	$^2\Sigma^+$	8.43	52.789	4423

Table 2.2.: *Calculated values for the Morse potential for the four lowest-lying electronic states of the RbYb molecule. From [55]*

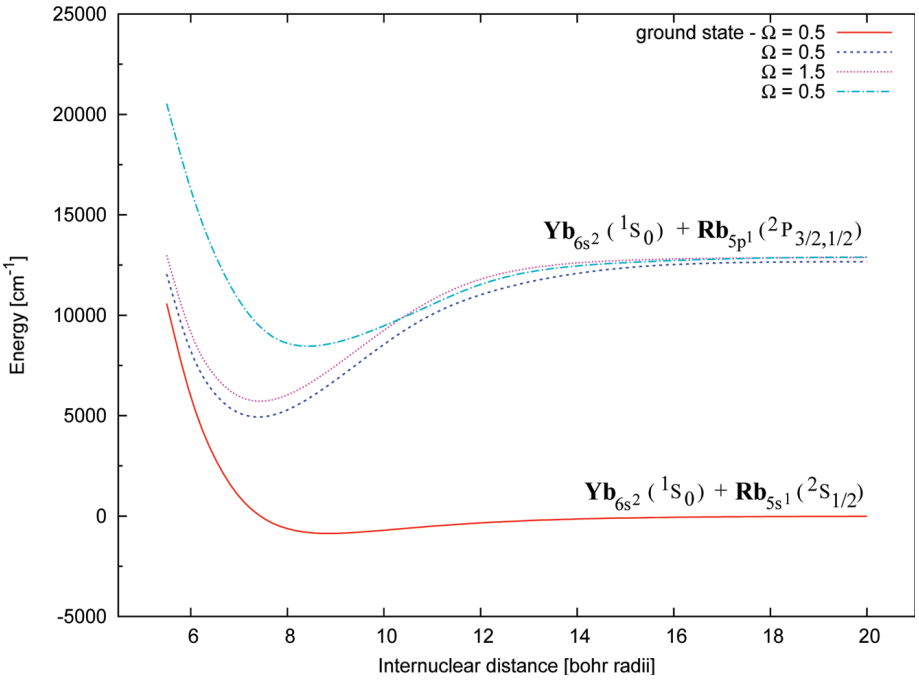

Figure 2.3.: *Ab initio calculations of the four lowest-lying electronic states of the RbYb molecule. From [55]*

with more experimental data, which will be provided in this thesis with the 2-Photon-Photoassociation. A calculation of the long-range part of the potential will be given in this context (see chapter 5.8).

2.2.1. Electronic states

A diatomic molecule consists of two atoms a and b. It has, similar to atoms, different angular momenta. I will use the same notation as in [76]:

- **L** which is the electronic orbital angular momentum. It is the sum of the individual electronic angular momenta from the two atoms: $\vec{L} = \vec{l}_a + \vec{l}_b$,

- **S** is the electronic spin angular momentum which is the sum of the two individual electronic spins of the atoms: $\vec{S} = \vec{s}_a + \vec{s}_b$,
- **F** is the sum of the electronic orbital angular momentum and the spin: $\vec{F} = \vec{L} + \vec{S}$,
- **J** is the sum of all angular momenta including the rotational angular momentum: $\vec{J} = \vec{L} + \vec{S} + \vec{R}$,
- **N** is the total angular momentum excluding the electronic spin, so that $\vec{N} = \vec{J} - \vec{S}$ and
- **R** is the rotational angular momentum of the nuclei, which is $\vec{R} = \vec{N} - \vec{L}$.
- **I** is the nuclear spin angular momenta.

Note that most of the angular momenta of the involved atoms are not conserved in the molecule. Usually, only the projections of the momenta are good quantum numbers, see the next section about the coupling cases.

The naming convention for molecular states is

$$^{2S+1}\Lambda^{\pm}_{\Omega_{g/u}}.$$

Here, Λ is the projection of $\vec{L}$ to the internuclear axis, Σ is the projection of $\vec{S}$ to the internuclear axis and Ω is the sum of Λ and Σ. The parity g/u is only defined for homonuclear diatomic molecules and shows the inversion symmetry of the wavefunction relative to the center of charge. The symmetry of the wavefunction along the internuclear axis is given by $\pm$. Whenever Λ is not defined (see below for the coupling cases), it is also possible to name the states only with its Ω. The definition of Λ depends on the coupling of the different angular momenta which were first classified by Hund [80].

2.2.2. Hund's coupling cases

In contrast to atoms, diatomic molecules are not spherically symmetric, but they are cylindrically symmetric along the internuclear axis of the two atoms. This leads to different types of possible couplings, which were first described by Hund [80] in five[3] idealized different coupling cases. I follow the treatments in [76, chap. 6.7] here.

Hund's coupling case (a)

In Hund's case (a), the orbital angular momentum $\vec{L}$ is strongly coupled to the internuclear axis by electrostatic forces. The electron spin angular momentum $\vec{S}$ is strongly coupled to $\vec{L}$ and therefore, to the internuclear axis. The projection of these two momenta to the internuclear axis is well defined and are denoted Λ for the orbital angular momentum and Σ for the spin. Their sum is denoted $\Omega = \Lambda + \Sigma$. The rotational component $\vec{R}$ is coupled to Ω (pointing along the internuclear axis) and forms the total angular momentum $\vec{J}$. The two projections of Λ and Σ have two possible magnitudes $\pm\Sigma$ and $\pm\Lambda$ which results in a degeneracy which can be removed by molecular rotation. This is the so-called Λ-doubling respective Ω-doubling. Good quantum numbers for this case are $\Lambda, S, \Sigma, J, \Omega$.

[3] Hund identified only 4 different types, but a fifth case is possible.

Hund's coupling case (b)

When the coupling between $\vec{L}$ and $\vec{S}$ is weak (no spin-orbit coupling), the spin $\vec{S}$ is not coupled to the internuclear axis. In Hund's case (b), the orbital angular momentum is coupled to the internuclear axis (as it is in case (a)), but $\vec{S}$ is not. Thus, Ω is not defined anymore. The projection of $\vec{L}$ is Λ which then couples to a rotational momentum $\vec{R}$. This forms $\vec{N}$. The total angular momentum is then formed by coupling $\vec{N}$ to $\vec{S}$. If $\vec{S} \neq 0$, a spin-rotation splitting is possible for states with $N > 0$. Good quantum numbers for this case are Λ, N, S, J.

The two cases (a) and (b) are the most common for deeply-bound diatomic molecules.

Hund's coupling case (c)

In Hund's case (c), the coupling between $\vec{L}$ and $\vec{S}$ is stronger than the coupling to the internuclear axis. In this situation, the projections Λ and Σ are not defined. The two momenta couple to form a component $\vec{J}_a$ which then is coupled to the internuclear axis. The projection of this is then Ω which couples to the rotational momentum $\vec{R}$ to form the total momentum $\vec{J}$. The resulting states can be degenerate for $\Omega \neq 0$. This degeneracy is removed by rotation and is called Ω-doubling. Good quantum numbers are J_a, Ω, J.

Hund's coupling case (d)

If the coupling between $\vec{L}$ and $\vec{R}$ is much stronger than to the internuclear axis, it will be identified as Hund's case (d). The result of the coupling between $\vec{L}$ and $\vec{R}$ is $\vec{N}$ which then couples to the spin $\vec{S}$ to form the total angular momentum $\vec{J}$. Because of the coupling, each rotational state splits up into $2L+1$ components except where $R < L$, where there are $2R+1$ components. This case is a good description of many Rydberg molecules [81], where the outer electron couples very weakly to the molecular core. Good quantum numbers are L, R, N, S, J.

Hund's coupling case (e)

Hund's case (e) was not identified by Hund, but a fifth coupling case is possible: Here, $\vec{L}$ and $\vec{S}$ are coupled strongly to each other. They form a resultant J_a. This vector couples only very weakly to the internuclear axis and therefore it couples to the rotation $\vec{R}$ and form the total angular momentum $\vec{J}$. For the different rotational levels, a splitting is possible giving $2J_a + 1$ respective $2R + 1$ states. Good quantum numbers are J_a, R, J.

2.2.3. Vibrational states

In contrast to atoms, molecules have two more degrees of freedom. They can initiate vibrations and rotations. The vibrational level of a molecule can in principle be calculated by the potential form and the solution of the energy eigenvalues of the Schrödinger equation. The potential is similar to an anharmonic oscillator and therefore, the solution is similar

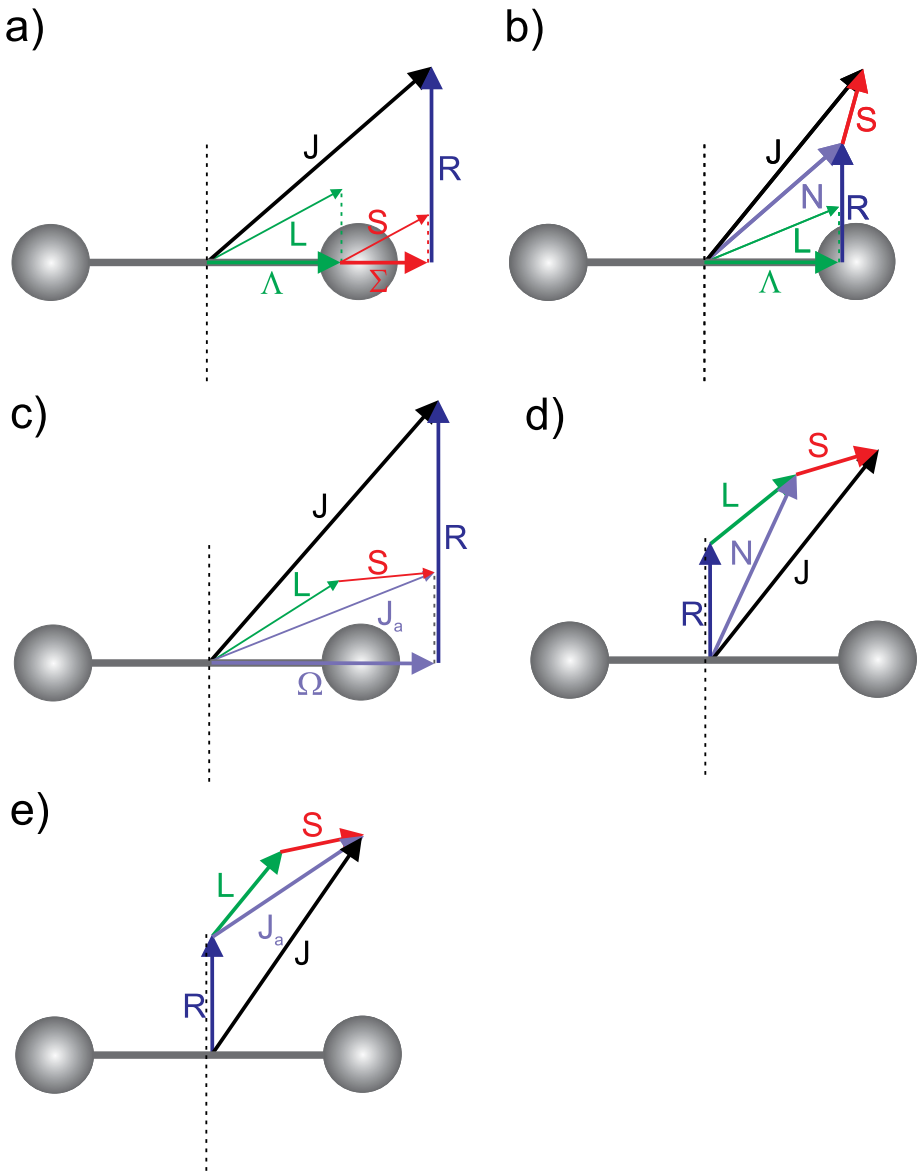

Figure 2.4.: *Illustration of the 5 different Hund's cases. Different types are possible depending on the strength of the coupling of the different angular momenta. Adapted from [82].*

to it. A molecular potential curve can be approximated by the Morse potential [79]. Remember equation (2.18)

$$V(r) = E_D \left(1 - e^{-a(r-R_e)}\right)^2$$

where E_D is the dissociation energy, R_e is the equilibrium distance of the two atoms and

$$a = \sqrt{\frac{\mu}{2E_D}}\omega_e \tag{2.19}$$

is a molecule specific constant with the reduced mass μ and the vibrational frequency ω_e. The solution for the energy eigenvalues for a vibrational level v can be analytically solved to [79]

$$E_v = \hbar\omega_e \left(v + \frac{1}{2}\right) - \frac{\hbar\omega_e}{4E_D}\hbar\omega_e \left(v + \frac{1}{2}\right)^2. \tag{2.20}$$

This potential gives a good approximation for deeply bound levels. For the long-range states, which are investigated by photoassociation, this approximation is no longer the best. It is more advantageous to use a potential like

$$V(r) = C_6/r^6 \tag{2.21}$$

with a negative value for the C_6 coefficient to get an attractive potential. LeRoy and Bernstein [6] presented a semi-analytical approximation for this potential. In the photoassociation spectroscopy, this helped us to identify the different vibrational level we observed:

$$E_v = E_D - \left((v_D - v) \cdot \sqrt{\frac{\pi}{2\mu}} \cdot \frac{\Gamma(1 + 1/n)}{\Gamma(1/2 + 1/n)} \cdot \frac{\hbar(n-2)}{(-C_n)^{1/n}}\right)^{\frac{2n}{n-2}} \tag{2.22}$$

Here, Γ is the gamma function, μ is the reduced mass of the system and n denotes the order of the leading long range coefficient (for a heteronuclear system, it is $n = 6$). The non-integer dissociation quantum number v_D gives as its integer the maximum vibrational quantum number and the fractional part is an indication for the binding energy of the last vibrational level. This equation works quite well in the long-range part of the molecular level, but not near the dissociation limit where $E_D - E_v < 10$ GHz. In this regime, relativistic retardation effects appear and modify the potential [83]. But for the observed resonances, this approach works well for identification purposes (see chapter 4 and 5).

2.2.4. Rotational states

The rotational structure of a diatomic molecule can be described by the rigid rotor approximation [76, chap. 6.8]. Here, the two nuclei are assumed to have a fixed distance R and rotate around the center of mass. The relevant rotation axis is perpendicular to the internuclear axis. In classical mechanics, this can be calculated as

$$E_{\text{rot}} = \frac{1}{2}\Theta\,\omega^2 \tag{2.23}$$

with ω being the angular velocity and Θ is the moment of inertia which is defined as

$$\Theta = m_1 r_1^2 + m_2 r_2^2 = \mu r^2 \tag{2.24}$$

with μ the reduced mass, r_1 and r_2 the distances of the two masses m_1 and m_2 from the center of mass and r defined as $r = r_1 + r_2$. The angular momentum L is defined as

$$|L| = \Theta\omega. \tag{2.25}$$

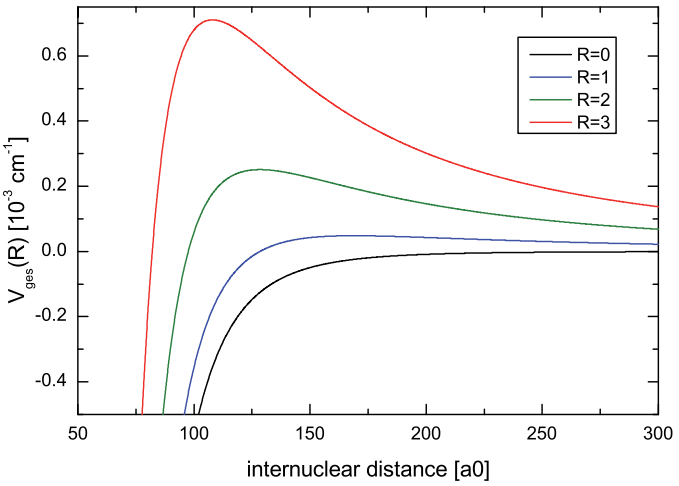

Figure 2.5.: *Change of the potential due to rotation of the molecule. Here, a potential for* $^{176}Yb^{87}Rb$ *was plotted with a* $C_6 = -2563\mathrm{E_h a_0^6}$*, which was derived from our experimental observations for the ground state potential.*

Together with (2.23), this gives us

$$E_{\mathrm{rot}} = \frac{L^2}{2\Theta}. \tag{2.26}$$

If we now quantize the angular momentum, we get for the rotational energy

$$E_{\mathrm{rot}} = \frac{\hbar^2}{2\Theta}\, R\cdot(R+1) = \frac{\hbar^2}{2\mu r^2}\, R\cdot(R+1) = B_{\mathrm{rot}}\, R\cdot(R+1). \tag{2.27}$$

Here, the rotational constant B_{rot} was introduced:

$$B_{\mathrm{rot}} = \frac{\hbar^2}{2\mu r^2} \tag{2.28}$$

In photoassociation spectroscopy, this rotational constant can be measured and therefore an averaged size of the molecule can be determined.

2.2.5. Centrifugal barrier

The rotational energy is part of the effective potential of the molecule. Depending on the rotation of the molecule, this potential becomes

$$V_{\mathrm{ges}}(r) = V(r) + \frac{\hbar^2\, R\cdot(R+1)}{2\mu r^2}. \tag{2.29}$$

Fig. 2.5 shows this dependence. This additional repulsive potential is called the centrifugal barrier. The height of this barrier can be calculated following the treatment in [25] to:

$$E_c(R) = \frac{1}{2}\left(\frac{R\cdot(R+1)}{3}\right)^{3/2} E_{\mathrm{vdW}} \tag{2.30}$$

R	E_c $\left[10^{-3}\,\mathrm{cm}^{-1}\right]$	T_c $[\,\mu\mathrm{K}]$
0	-	-
1	0.0483	69.5
2	0.2511	361.3
3	0.7102	1021.8

Table 2.3.: *Energy of the centrifugal barriers for collision of ^{176}Yb and ^{87}Rb with varying angular momenta. The energies are calculated with a $C_6 = -2563\,\mathrm{E_h a_0^6}$ (see chapter 5). The temperature is given by $T_e = E_e/k_B T$.*

The specific energy for an atom pair is given by

$$E_{\mathrm{vdW}} = \frac{\hbar^2}{2\mu}\frac{1}{R_{\mathrm{vdW}}^2} \text{ with}$$
$$R_{\mathrm{vdW}} = \frac{1}{2}\left(\frac{-2\mu C_6}{\hbar^2}\right)^{1/4}. \tag{2.31}$$

For the isotopologue $^{176}\mathrm{Yb}^{87}\mathrm{Rb}$ the calculated values for different rotational states are shown in tab. 2.3. For photoassociation experiments, this means that the atoms are repelled from each other if they do not have enough energy to cross the barrier. This is the reason why the rotational angular momentum in our experiment is limited to $R = 2$ since the temperature of the atoms is about $400\,\mu\mathrm{K}$.

2.3. Wavenumbers

In the field of spectroscopy, the most common used unit is the wavenumber ν and normally given in the unit cm^{-1}. The definition of the wavenumber is $\nu = 1/\lambda$ with λ being the wavelength of the photon in vacuum. Thus, the wavenumber is proportional to the energy of a photon $E = hc\nu$ and energy differences can be easily calculated. Some conversion formulas are added for reference:

- The energy is $E = hc\nu$, where h is the Planck constant, c is the speed of light and ν is the wavenumber. Thus:

  $$1\,\mathrm{cm}^{-1} \mathrel{\hat{=}} 1.986446 \cdot 10^{-23}\,\mathrm{J},$$

  $$1\,\mathrm{J} \mathrel{\hat{=}} 5.034 \cdot 10^{22}\,\mathrm{cm}^{-1}.$$

- The frequency, given in Hz, is $\bar{\nu} = \frac{\omega}{2\pi} = c\nu$. Thus:

  $$1\,\mathrm{GHz} \mathrel{\hat{=}} 0.033\,\mathrm{cm}^{-1},$$

  $$1\,\mathrm{cm}^{-1} \mathrel{\hat{=}} 29.98\,\mathrm{GHz}.$$

- The wavelength is the reciprocal of the wavenumber in vacuum: $\lambda = 1/\nu$.

3.

Experimental apparatus

In this chapter, the experimental apparatus used in this work is described. This includes the setup for preparing ultracold samples of Rubidium and Ytterbium and the setup for the photoassociation. The two species will be continuously loaded in a combined magneto-optical trap where they will be photoassociated to excited molecules. An additional laser interacting with an excited molecular state and a molecular ground state is introduced which interferes with the photoassociation transition and thus provides information about the molecular ground state.

The setup for trapping the two species was used in previous experiments and is explained in detail in [1, 2, 3]. The photoassociation laser setup was redesigned compared to [3] and will be described in chapter 3.5.

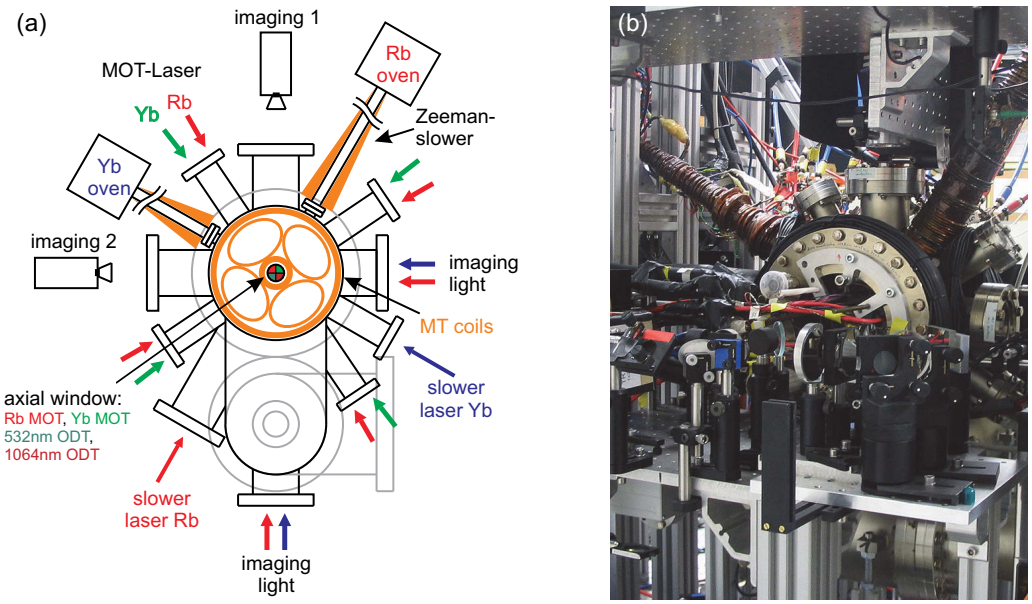

Figure 3.1.: *(a)Sketch and (b)photograph of our main vacuum chamber. From [4]*

3.1. Overview

All experiments presented in this thesis are performed in an ultra high vacuum with a pressure of $\approx 10^{-11}$ mbar to avoid collisions with hot background atoms. Fig. 3.1 shows a picture of our chamber. It is a wheel-style steel vacuum chamber connected with two Zeeman slowers, one for each atom species. In this chamber, rubidium and ytterbium atoms are held in a combined magneto-optical trap. The needed magnetic field is created by a single-side configuration of two coils. These coils are calculated to generate a magnetic field gradient of $(\partial B/\partial z)/I = 0.44\,\mathrm{G/cm}$ in axial respective $(\partial B/\partial r)/I = 0.22\,\mathrm{G/cm}$ [2] in radial direction. For the experiments described in this thesis, we are normally working with a current of $I = 40\,\mathrm{A}$ providing an axial field gradient of $17\,\mathrm{G/cm}$ and a radial gradient of $9\,\mathrm{G/cm}$. This gradient was found to be the best compromise for trapping the two species simultaneously.

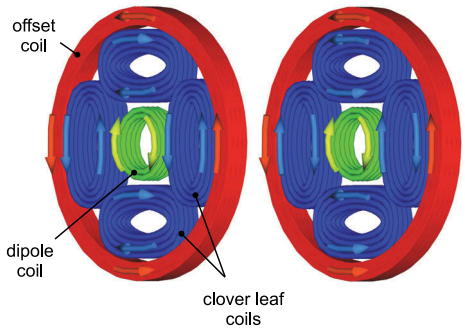

Figure 3.2.: *Schematic of the setup of our magnetic coils. The arrows indicate the current flow in MOT or magnetic trap operation. For Feshbach resonance experiments, a homogeneous magnetic field is needed and thus, the current flow of the dipole coils is switched. From [1].*

For conservative trapping, additional coils in a clover-leaf geometry are attached to our chamber (see fig. 3.2) leading to a magnetic trap geometry. Three pairs of compensation coils provide (nearly) homogeneous magnetic fields in all three dimensions which are used to compensate any unwanted stray fields and to shift the position of the magnetic zero in the MOT respective the minimum for the magnetic trap.

By switching the polarization of the dipole coils, it is possible to produce a (nearly) homogeneous magnetic field in the trapping region which will be used in Feshbach experiments in the near future (see chapter 7 for details).

A detailed description of our vacuum chamber can be found in [1] and [2].

3.2. Atom detection and imaging system

The most important information in the experiments described here is the (relative) atom number in Rb and Yb. For this, we are using a photodiode for the Rb system which

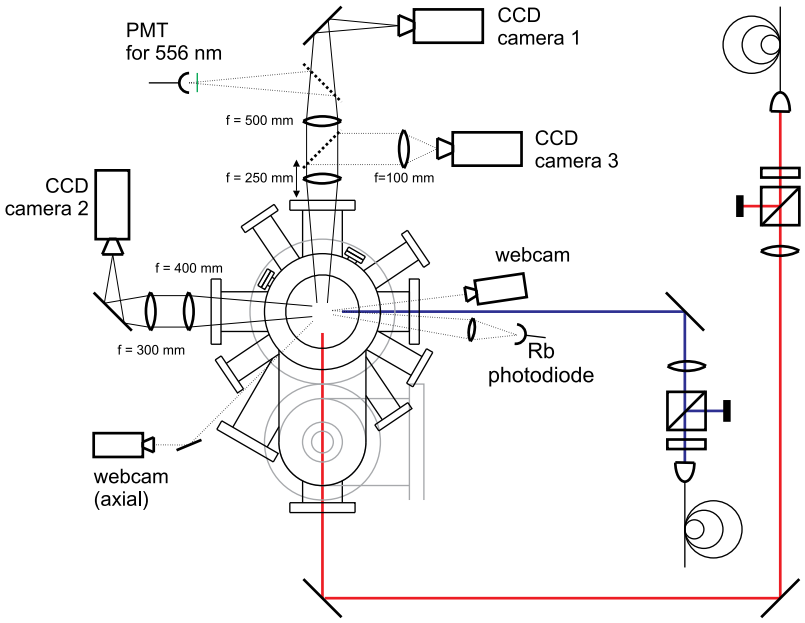

Figure 3.3.: *Imaging system in the current setup. Adapted from [4].*

monitors continuously the fluorescence of the Rb MOT and a photomultiplying tube for the Yb MOT because of the lower fluorescence of the atoms. A green filter blocks every unwanted light to improve the signal to noise ratio.

The imaging system used in the current setup is shown in fig. 3.3. It includes 3 charge-coupled-device (CCD) cameras providing density distributions of the MOTs. This information is used for the determination of the absolute atom number, the size of the MOTs and the temperature. It is also used in the alignment process. Camera 1 and camera 3 are providing images in the yz plane of the MOT. Camera 1 (Finger Lakes Instrumentation MaxCam 7-E) has a resolution of 764×512 pixel and can image MOT clouds with a maximal size of $3.3 \times 2.2\,\mathrm{mm}^2$. In the same direction, camera 3 (ABS Jena UK1117) can be used instead of camera 1 when an additional mirror is placed in the imaging path. It has a different imaging scale than camera 1 and is able to image large atom clouds with a size of up to $15.6 \times 11.8\,\mathrm{mm}^2$ (768×576 pixel). Camera 2 (ABS Jena UK1117) takes pictures in the xz plane of MOTs with a size of up to $4.5 \times 3.4\,\mathrm{mm}^2$ (768×576 pixel).

For measuring the density distribution, it is possible to use either fluorescence imaging or absorption imaging. In fluorescence imaging, the atoms are illuminated by resonant light. The fluorescence of the MOT is recorded with the cameras. In absorption imaging, an additional resonant imaging beam is shining through the MOT on the camera recording the shadow of the MOT. The imaging light is provided through single mode fibers. Depending on which camera should be used for which atom species, the fibers are connected to the experiment. In normal operation, we image Yb atoms in the xz plane while Rb is imaged in the yz plane. This can be done simultaneous.

For alignment purposes, we installed two standard webcams at different directions to

the atom clouds to monitor the position of the MOTs and for diagnostic purposes.

3.3. Rubidium MOT

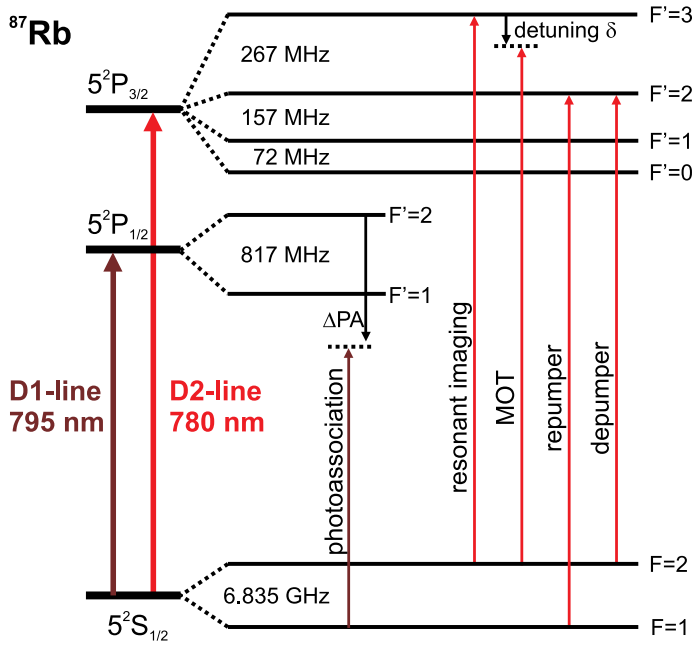

Figure 3.4.: *Relevant Rb levels (not to scale). The slower is working on the same transition as the MOT, but with a larger detuning. The photoassociation beam is working on the red side of the D_1 line.*

In our current setup, we trap ^{87}Rb in a MOT. For the Zeeman slower and the MOT we use the D_2 line at 780 nm. The main transition for cooling and trapping use the $|^2S_{1/2}\rangle$ ground state in the hyperfine level $F = 2$ and the excited $|^2P_{3/2}\rangle$ state in the hyperfine level $F' = 3$. This is in principle a closed transition, because the selection rule $\Delta F = 0, \pm 1$ prevents atoms to enter the $F = 1$ ground state, but due to non-resonant excitations, the atoms are sometimes excited to the $F' = 2$ state. From this state, a spontaneous decay to the $F = 1$ ground state is possible where the atoms are lost from the cycling transition. Thus, an additional laser is needed to pump these atoms back in the cooling transition. This repumper excites the atoms from the $|^2S_{1/2}, F = 1\rangle$ ground state level to the $|^2P_{3/2}, F' = 2\rangle$ state and returns them into the cycling transition. A sketch of the relevant Rb levels is shown in fig. 3.4.

The light required for the MOT is created by 4 diode lasers (Sharp GH0781JA2C, rated 120 mW at 784 nm) from which two are stabilized using a Rb vapor cell. The first laser, used as the repumping beam at the transition $|F = 1\rangle \rightarrow |F' = 2\rangle$, is designed with a narrow bandwidth interference filter [84]. The second laser, stabilized to the transition $|F = 2\rangle \rightarrow |F' = 3\rangle$, is designed as an external cavity diode laser (ECDL) in Littrow-

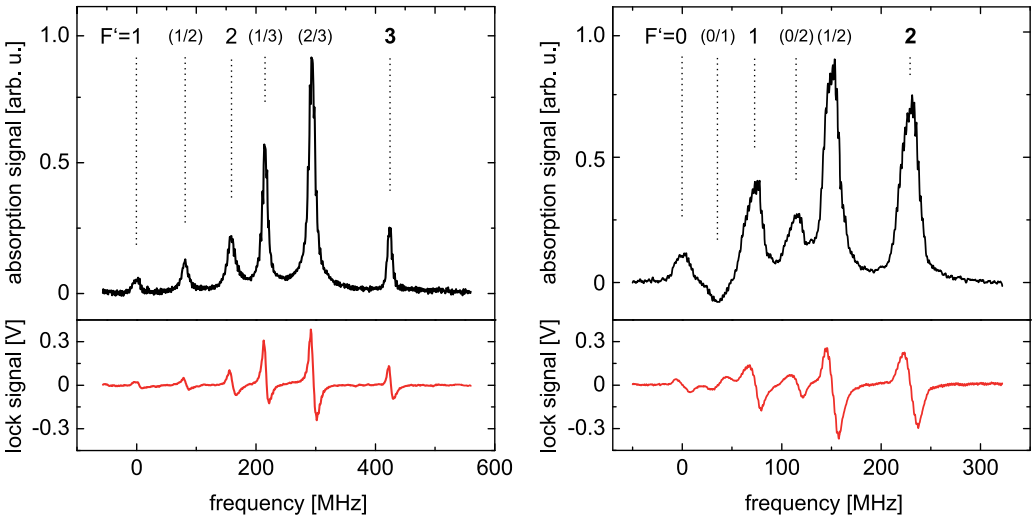

Figure 3.5.: *Doppler free lock signals for the Rb MOT master (left side) and the repumping beam (right side). The MOT master is locked to the $F' = 3$ resonance while the repumper is locked to the $F' = 2$ state. The lock signal is created by a frequency modulation of the laser and the dispersive signal is created through demodulation with lock-in techniques. Adapted from [4].*

configuration [85]. This laser injects the two other laser diodes which then acts as slave lasers providing enough power for slowing and trapping.

The frequency stabilization of the two master lasers is done via Doppler-free saturation spectroscopy [86] in Rb vapor cells independently for each laser. The Doppler free absorption signal is shown in fig. 3.5. The light for the spectroscopy is frequency modulated through an acousto-optical modulator (AOM) (in fig. 3.6 AOM4 and AOM5 for the two master lasers) in double-pass configuration to avoid a spatial shift. A demodulation through lock-in techniques creates the dispersive signal. Needed frequency shifting is achieved with AOMs which also provide a fast switching, power adjustment and frequency control of the light. Additionally, all beams can be switched on or off with mechanical beam shutters. The current scheme of this laser system is shown in fig. 3.6.

In a MOT consisting of a large atom number, the interaction between the atoms plays a role and the density is limited. The atoms experience a repulsive force because of reabsorption of scattered atoms (radiation trapping) [87]. To overcome this effect, it is essential to lower the reabsorption processes. In a MOT working with a repumper this can be achieved easily: If the repumping beam has a hole in the center of the beam then the atoms which are in this region can fall into a dark state (in our case it is the $F = 1$ ground state) and they do not scatter any photons anymore. This is reached by inserting an obstacle into the repumping beam at the beam center. The atoms are not trapped anymore but since they are in the center of their trap they return in the cooling (and trapping) process once they fall out of the dark regime of the repumping beam. This type of trap is called Dark Spot MOT [88, 89]. To enhance this effect, a third laser ("depumper"), resonant to the

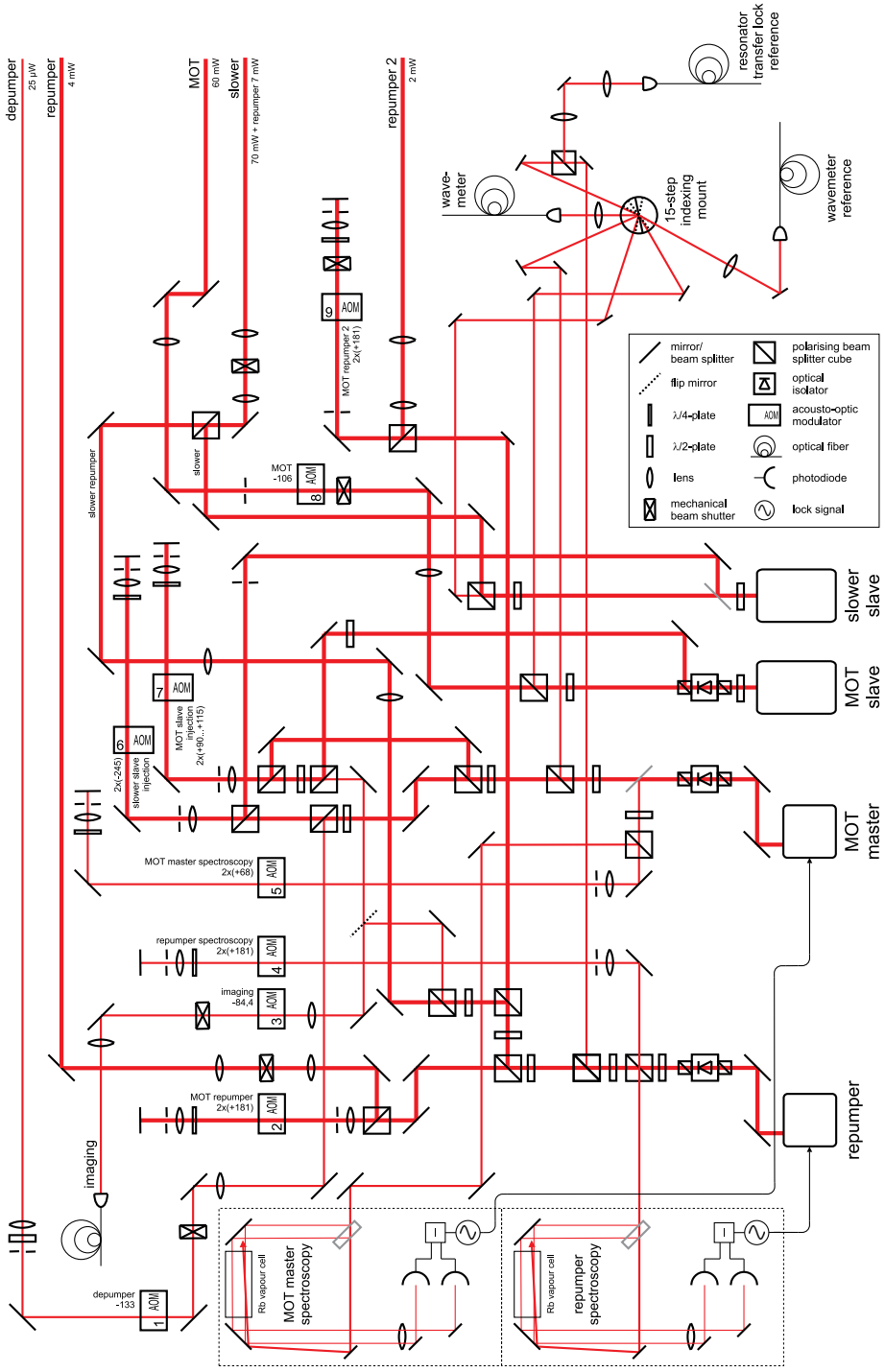

Figure 3.6.: *Rb laser system. The MOT master laser is locked to the $F = 2 \rightarrow F' = 3$ transition on the D_2 line of Rb. The repumping laser is locked to the $F = 1 \rightarrow F' = 2$ transition. Adapted from [4]*

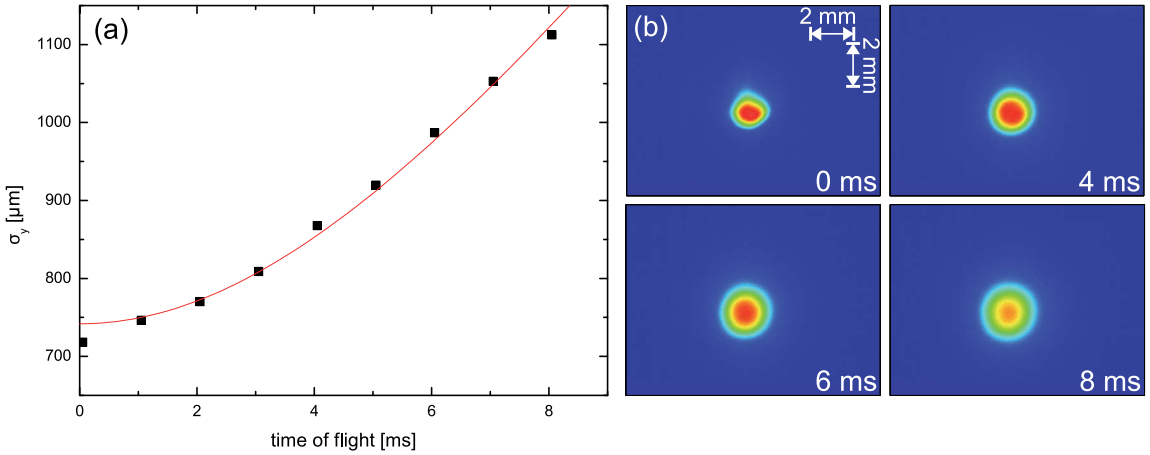

Figure 3.7.: *Time of flight measurement of the Rb MOT. The MOT was released from the trap and after some time a picture of the MOT was taken (b). The $1/e^2$ radius of the MOT at different flight times is shown in (a). A fit to this data yields a temperature of* $T_{\mathrm{Rb,y}} = 114 \pm 4\,\mu\mathrm{K}$.

transition $|^2S_{1/2}, F = 2\rangle \rightarrow |^2P_{3/2}, F' = 2\rangle$, is superimposed to the center of the MOT which forces the atoms into the dark state.

To measure the temperature of the MOT, we apply a time-of-flight method in which pictures of the MOT are taken. For this, a resonant imaging beam is needed and all atoms have to be repumped into the cycling process, therefore a second repumping beam without obstacle illuminating the whole MOT region is needed as well. Fig. 3.7 shows a typical temperature measurement. The atoms in the MOT are released from the trap and after a varying time of flight, a picture is taken. From the size of the cloud, the temperature, atom number and atom distribution can be determined.

A harmonic trapping potential, as assumed here, has a Gaussian density distribution:

$$\tilde{n}(y,z) = \int n(x,y,z)dx = N\sqrt{2\pi}\sigma_x \exp\left(-\frac{y^2}{2\sigma_y^2} - \frac{z^2}{2\sigma_z^2}\right) \tag{3.1}$$

The density $\tilde{n}$ is the column density as imaged by our CCD camera for an atom cloud with the density n. After released from the trap, the atoms expand ballistic as a function of the time of flight (TOF) [90]:

$$\sigma_i\left(t_{\mathrm{TOF}}\right) = \sqrt{\sigma_i\left(0\right)^2 + \frac{k_B T}{m} t_{\mathrm{TOF}}^2} \quad \text{with} \quad i = [x,y,z] \tag{3.2}$$

where σ_i is the size of the atom cloud, m is the mass of one atom and $\sigma_i(0)$ is the initial size of the cloud which depends on the trapping potential. The peak density ρ_{max} in the trapping center can be calculated from eqn. (3.1) to

$$\rho_{\mathrm{max}} = \frac{N}{\sigma_r(0)^2\sigma_a(0)(2\pi)^{3/2}}. \tag{3.3}$$

Here, the trapping geometry is already included, giving the radial component $\sigma_r = \sigma_x = \sigma_y$ and the axial component $\sigma_a = \sigma_z$.

We get about $4.2 \pm 1.2 \ \cdot 10^8$ Rb atoms with a $1/e^2$ radius of $\sigma_y = 740\ \mu$m respective $\sigma_z = 715\ \mu$m. This denotes a density of $6.8 \cdot 10^{10}\ \mathrm{cm}^{-3}$. The temperature of the MOT is measured to be

$$\begin{aligned} T_{\mathrm{Rb,y}} &= 114 \pm 4\ \mu\mathrm{K}, \\ T_{\mathrm{Rb,z}} &= 142 \pm 8\ \mu\mathrm{K}. \end{aligned} \tag{3.4}$$

The temperatures differ in each dimension, because the atoms are not in a true thermal equilibrium since the interactions with the trap still play a role [3]. But this interaction is assumed to have nearly no influence for the experiments performed during this thesis, therefore an averaged temperature is used:

$$T_{\mathrm{avg}} = \frac{1}{3}\left(T_x + T_y + T_z\right) \tag{3.5}$$

where $T_x = T_y = T_r$ is the radial temperature and $T_z = T_a$ is the axial temperature due to our trapping geometry. This gives a temperature of

$$T_{\mathrm{Rb,avg}} = 123 \pm 6\ \mu\mathrm{K}. \tag{3.6}$$

All of these measurements were performed without Yb atoms present, but the presence of Ytterbium atoms does not have any measurable effect on the Rb.

3.4. Ytterbium MOT

Ytterbium has 7 stable isotopes from which 5 are bosons and 2 are fermions. It is a rare earth metal with an alkaline-earth like structure. The bosonic isotopes do not have a hyperfine structure and therefore the relevant level structure is quite simple, see fig. 3.8.

Ytterbium has two cycling transitions that are used in our setup. The transition at 399 nm from $|^1S_0\rangle \rightarrow |^1P_1\rangle$ is used for the first cooling stage in the Zeeman slower. In fig. 3.9 (a), a fluorescence signal from an Yb atomic beam is shown. The laser is locked to the desired Yb isotope. The transition exhibits a large linewidth which means that the cooling and slowing process is fast because of the short lifetime, but it also means that the Doppler temperature is comparatively high. The laser system for the blue transition consists of a Master-Slave setup with laser diodes (master diode: Nichia NDHV310ACAEI, rated 30 mW at 399 nm; slave diode: Nichia NDHV310APC, rated 60 mW at 401 nm). The master diode is an ECDL with the same setup as the Rb MOT diode and is frequency stabilized to an Yb spectroscopy signal with the same frequency modulated lock-in technique. This beam is used for imaging purposes and for injecting the slave diode which provides an usable output power of 20 mW for the slowing beam. Fig. 3.10 shows the setup for the blue system.

For trapping, we use the intercombination transition $|^1S_0\rangle \rightarrow |^3P_1\rangle$ at 556 nm. This transition has a linewidth of only $2\pi 182$ kHz leading to a Doppler temperature of only

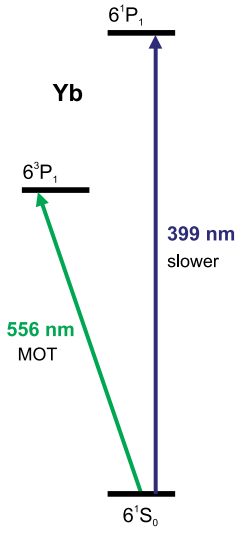

Figure 3.8.: *Relevant Yb levels for cooling and trapping.*

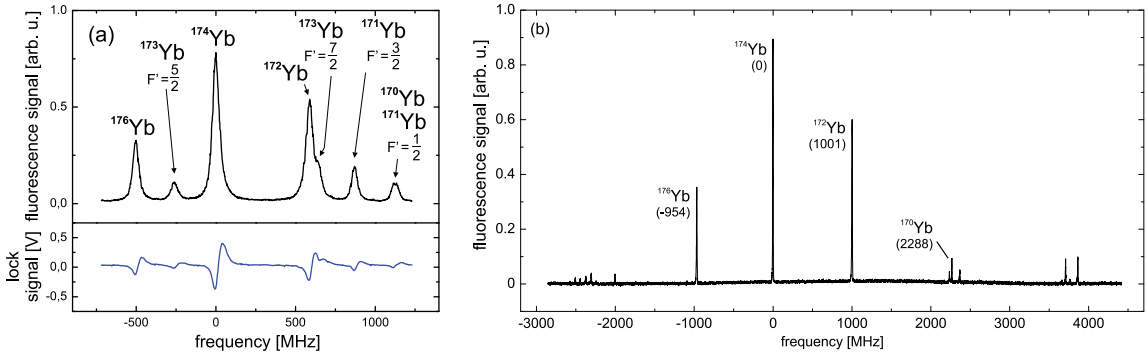

Figure 3.9.: *Yb spectroscopy signal for (a) 399 nm and (b) 556 nm. From [4].*

4.4μK. The green laser light is derived from a fiber laser at 1112 nm with an output power of 1 W (Koheras Boostik BoY10PztS). This laser is frequency-doubled in a periodically poled lithium niobate (PPLN) crystal in single pass configuration. The crystal is temperature stabilized to $\approx 180\,^{\circ}$C and leads to a usable output power of 30 mW of green light. The residual infrared light is separated from the green light at a dichroic mirror and sent to a beam block. Fig. 3.11 shows the setup of our green laser system. A small part of the frequency-double laser light is used to frequency stabilize the laser to an Yb spectroscopy signal. Here, the same lock-in technique as for the other stabilizations is used. The typical spectroscopy signal for green light is shown in fig. 3.9 (b).

All Yb isotopes are in principle visible in the spectrum for the blue and the green laser, therefore it is in principle possible to lock our lasers to any of these isotopes and it is possible to cool and trap all of the 7 stable isotopes of ytterbium. But ^{168}Yb has a very low natural abundance of only 0.13 % [60], therefore the signal is in normal operation of

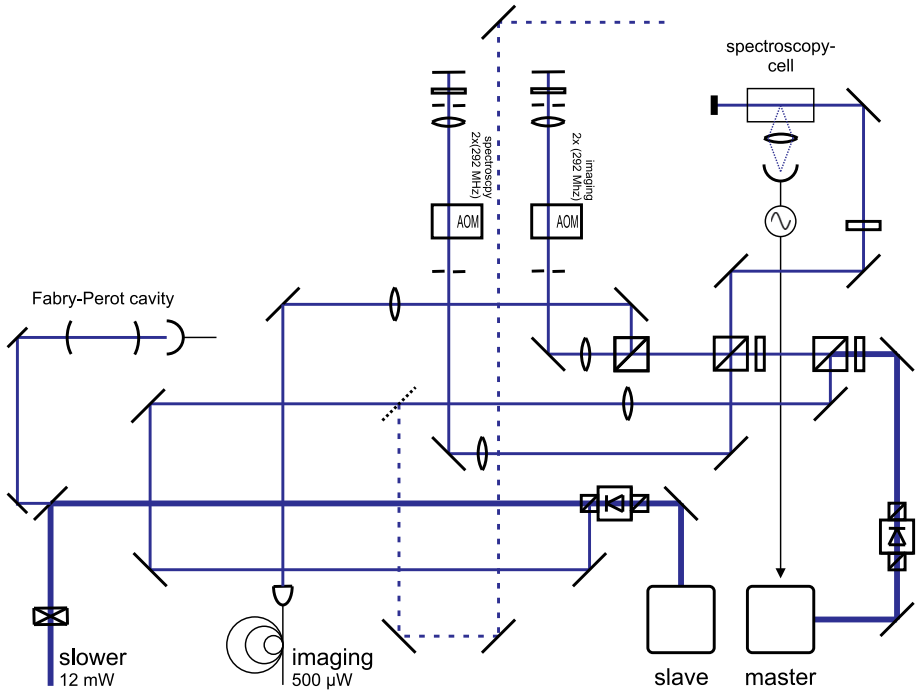

Figure 3.10.: *Yb laser system for imaging and Zeeman cooling. The master diode creates light at 399 nm for the transition* $|^1S_0\rangle \rightarrow |^1P_1\rangle$. *From [4].*

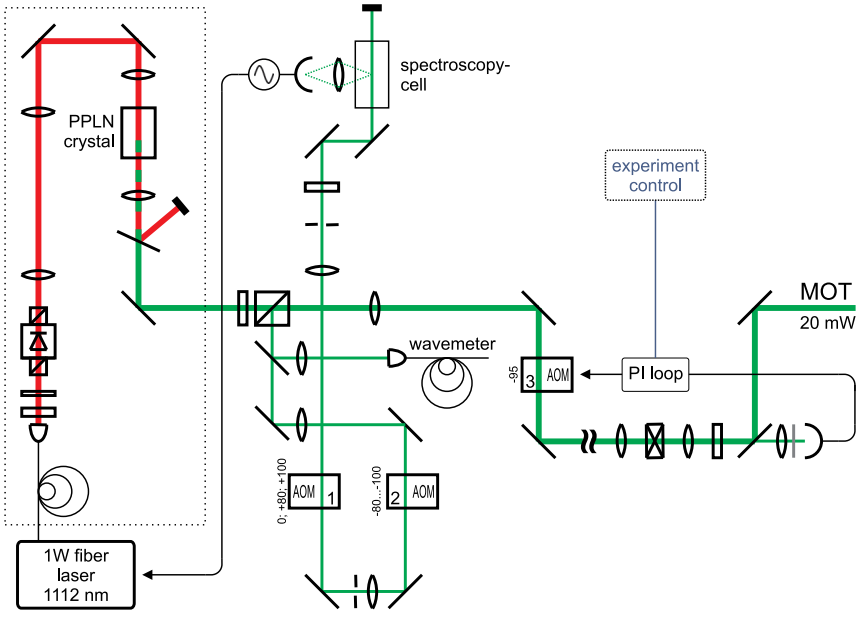

Figure 3.11.: *Yb laser system for the magneto-optical trap. The fiber laser is frequency doubled to a wavelength of 556 nm at the transition* $|^1S_0\rangle \rightarrow |^3P_1\rangle$. *From [4].*

our spectroscopy cell not visible, but a higher flux of Yb atoms and more spectroscopy light should make a locking possible.

We use the same time-of-flight method for determining temperature, atom number and density as for Rb. Without Rb, we get about $2.4 \cdot 10^6$ atoms with a temperature of

$$\begin{aligned} T_{\mathrm{Yb,x}} &= 387 \pm 107\,\mu\mathrm{K}, \\ T_{\mathrm{Yb,z}} &= 411 \pm 115\,\mu\mathrm{K} \end{aligned} \tag{3.7}$$

leading to an averaged temperature of $T_{\mathrm{Yb,avg}} = 395 \pm 110\,\mu$K. The MOT has a $1/e^2$ radius of $\sigma_x = 270\,\mu$m respective $\sigma_z = 465\,\mu$m yielding a density of $4.5 \cdot 10^9\,\mathrm{cm}^{-3}$. Note that the magnetic field gradient is optimized for the combined trapping of Yb and Rb. Therefore, the temperatures and densities are not the optimum that can be reached in single species experiments. When rubidium is present, the ytterbium atom number drops to about $0.6 \cdot 10^5$ atoms. This is mainly due to light-assisted collisions [82]. In Rb, there is no effect detectable because of the much higher atom number in Rb in comparison to Yb, so that the effect is negligibly small in Rb.

3.5. Photoassociation laser system

For the 2-Photon-Photoassociation, two lasers are needed from which one needs to be locked to a fixed wavelength and (until now) the second one is scanned over a large range.

Laser 1, from now on called PA laser, used at a fixed wavelength near the Rb D_1 transition at 795 nm, is derived from a diode laser (Sharp GH0781JA2C, rated 120 mW at 784 nm) heated to about 60 °C. Fig. 3.12 shows the actual setup for the photoassociation laser system. The PA laser is divided into three parts, from which one is going to our wavemeter, one to the locking system and the rest is injected into a tapered amplifier (m2k TA-0800-0500, rated 500 mW at 790-810 nm). This laser gives a usable output power after the optical isolator of about 200 mW which is sent to the experimental apparatus.

A locking system for this laser is needed since it is not stable enough in free-running mode and the experiment requires that it is possible to lock the laser to any desired frequency. It is therefore not possible to use a locking system similar to the MOT laser system, where an atomic transition is used. Instead, we are transferring the stability of the Rb MOT laser to this laser by using a resonator transfer lock [82]. This is implemented through a scanning Fabry-Perot interferometer in which the PA laser and a frequency stabilized laser with perpendicular polarization are injected. The transmitted light from the interferometer is split up into the two polarizations and fed into photodiodes. Fig. 3.13 shows the typical signal of the two photodiodes. A piezo changes the length of the Fabry-Perot interferometer and is controlled by a delta voltage with a frequency of 30 Hz so that the distance between the (fixed) resonance of the stabilized Rb MOT laser and the resonance of the PA laser is measured as a time difference which is repeated every cycle. To avoid errors due the hysteresis of the piezo, only distances from one flank of the delta voltage is used as an error signal for the locking control unit. With this error signal, it is possible to keep the difference of the two lasers constant and therefore to transfer the

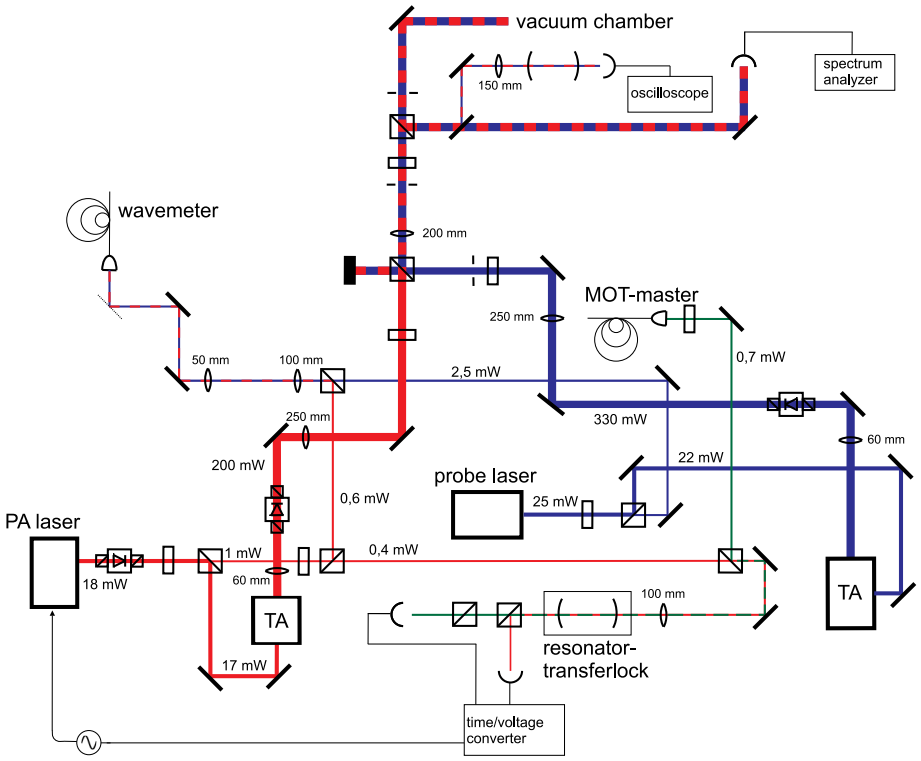

Figure 3.12.: *The laser system for the photoassociation. For 2-Photon-Photoassociation experiments, the PA laser can be locked with a resonator transfer lock whose reference laser is stabilized to a Rb reference. Adapted from [82]*

stability of the stabilized Rb laser to the PA laser. The short time fluctuations of the laser cannot be controlled with this locking scheme, because it is only providing error signals with a rate of 30 Hz. But these fluctuations are less than 5 MHz, which is enough for the measurements presented here. For long time stability, the resonator is temperature stabilized and built into a pressure sealed box to minimize the influence of temperature and pressure fluctuations. We measured a stability better then 5 MHz within an hour. A detailed description of the locking system can be found in [91].

The second laser, from now on called probe laser, is derived from a laser diode (Toptica DL pro) at 795 nm which can be scanned up to 20 GHz without a modehop. This laser is split into two parts. One part is used for wavelength determination and the other one is injected into a tapered amplifier (m2k TA-0800-0500, rated 500 mW at 790-810 nm) which gives up to 330 mW after the optical isolator. Up to now, this laser cannot be locked, but a similar resonator-transfer-locking scheme is planned for future experiments.

Fig. 3.12 shows the optical setup of our PA laser system. For our experiments, it is required that the two lasers have the same (linear) polarization. This ensures the best results in our experiments. Any effects caused by different polarizations were not examined. A discussion of these effects can be found in [92]. The two lasers are overlapped at a polarizing beamsplitter followed by a $\lambda/2$ waveplate and a second polarizing beamsplitter.

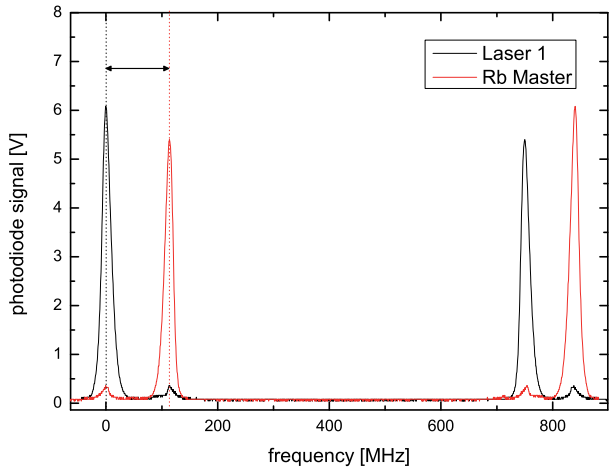

Figure 3.13.: *The principle of our locking system: Two lasers with different wavelengths are coupled into a scanning Fabry-Perot interferometer and the distance between the two peaks (shown as the black arrow in the picture) is kept constant leading to a transfer of the stability of one laser to the other.*

One output beam from this beamsplitter is used for the photoassociation process and the other output is injected into another scanning Fabry Perot interferometer for diagnosing purposes. This beam is also fed into a photodiode to measure the beat signal of the two lasers. The signal output of this photodiode is connected to a spectrum analyzer giving the beat frequency for frequency differences of the two lasers of up to 2 GHz.

The size of the two laser beams at the MOT position is chosen such that they have nearly the same size as the Yb MOT. The Yb MOT has a $1/e^2$ radius of $\sigma_x = 270\,\mu$m respective $\sigma_z = 460\,\mu$m. The PA laser has a $1/e^2$ radius of $r_x = 425\,\mu$m respective $r_y = 299\,\mu$m while the probe laser is more elliptic and has a $1/e^2$ radius of $r_x = 952\,\mu$m respective $r_y = 245\,\mu$m (see fig. 3.14). This gives an intensity for the PA laser, used for the free-bound transition of up to $I_{\mathrm{PA}} = 50\,\mathrm{W/cm^2}$ and for the probe laser of up to $I_{\mathrm{probe}} = 45\,\mathrm{W/cm^2}$. Note that these values are maximum ratings that are only available when only one laser is shining onto the atoms. If both lasers are used, the maximum intensity is decreased since the lasers are superimposed on a polarizing beam splitter with the same polarization.

3.6. Alignment process

In principle, a MOT is centered around the zero of the magnetic field. Due to misalignment or imbalance of the MOT beams, it can happen that the trap is pushed to another position. Therefore, it is needed to take care of the position to ensure a good overlap of the MOTs. For this, the CCD cameras are used to determine the positions of the MOTs and to adjust the MOT beams. The Rb MOT in continuous loading setup has too many atoms for the

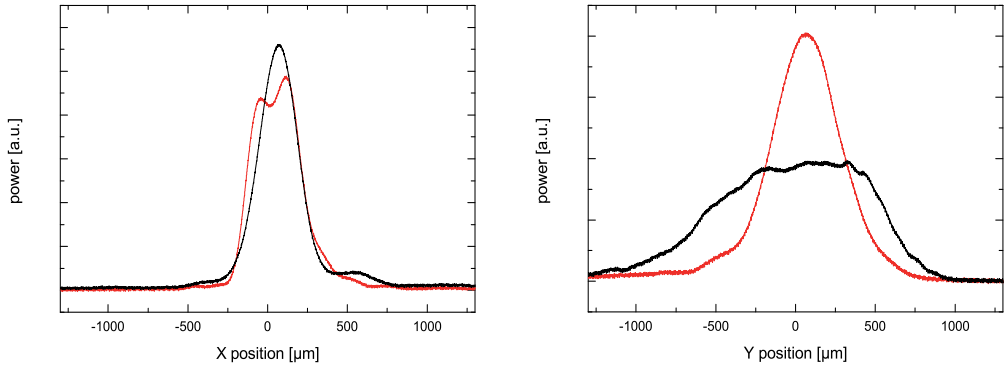

Figure 3.14.: *The size of the PA laser (red curve) used for the photoassociation of the free-bound transition and the probe laser (black) at the position of the MOT. The* $1/e^2$ *radius of the two beams are:* $r_{x,PA} = 425\,\mu$m, $r_{y,PA} = 299\,\mu$m *and* $r_{x,probe} = 952\,\mu$m, $r_{y,probe} = 245\,\mu$m.

camera which leads to saturation in the trapping center. Thus, it can be useful to look at the "background" Rb MOT by blocking the slowing beam.

When the two MOTs are overlapped, one must ensure that the photoassociation beam is superimposed to the MOT. For that, the PA beam is locked to a known PA resonance and adjusted carefully so that the Yb fluorescence is lowest. This is the best position of the PA beam. For the 2-Photon PA experiments, an overlap of the two beams must be ensured over a long range beginning at the position of the polarizing beam splitter. This can be proofed when the PA laser is locked to an 1-Photon-PA resonance and the second laser is located on a 2-Photon-PA resonance. This laser is staying stable on the desired frequency for a few minutes without locking. This needs to be checked from time to time. Then, the overlap of the two beams can be adjusted by monitoring the Yb fluorescence which must reach a maximum for best performance of the probe laser.

3.7. Wavelength measurement and data acquisition

In a typical 2-Photon-Photoassociation experiment, the PA laser is fixed to a free-bound photoassociation transition and the probe laser is scanned over the desired range. The frequency of the PA laser is found by applying only this laser to the double species MOT. It is then carefully adjusted in frequency until the Yb fluorescence signal is at its minimum which means that it is on a 1-Photon-Photoassociation resonance. In a next step, the probe laser is applied to the MOT and to the wavemeter. The self-built wavemeter is based on a Michelson interferometer with one moving mirror. In standard operation, a Helium-Neon-Laser is used as a reference providing an accuracy of about $\pm 1 \cdot 10^{-3}$ nm for the measured absolute wavelength [3]. The accuracy can be improved by using a frequency stabilized laser light, which is in our case one part of the light that is also used

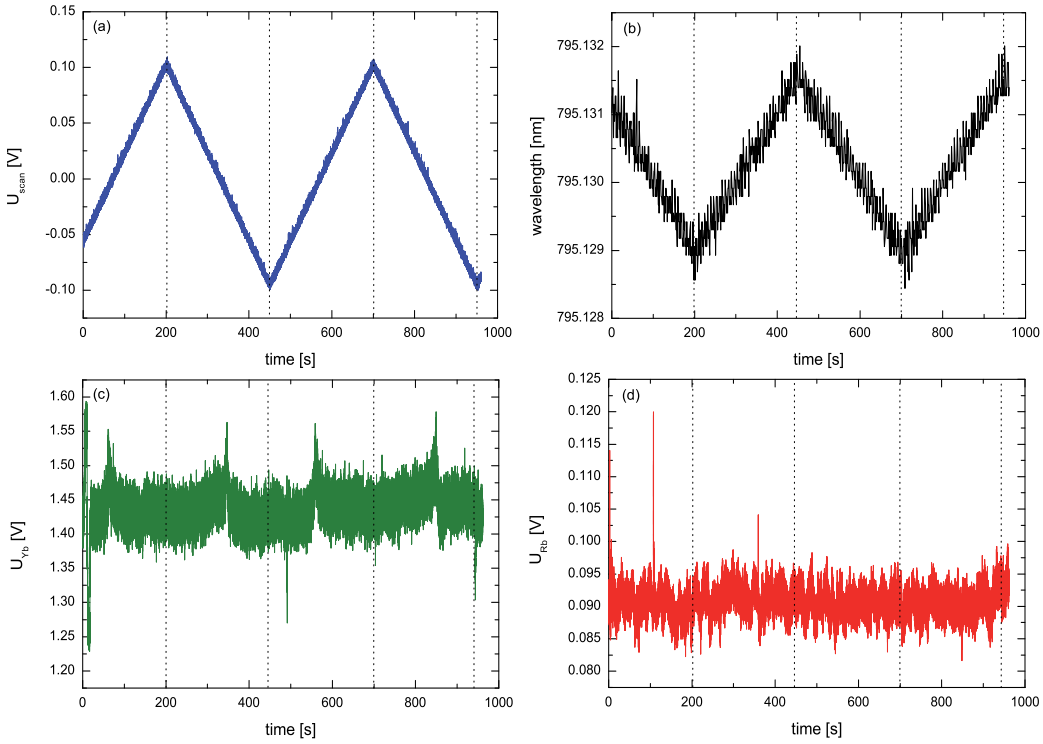

Figure 3.15.: *Example scan from a typical experiment. (a) Scan control voltage, (b) wavelength from the wavemeter, (c) Yb fluorescence signal and (d) Rb fluorescence signal. The vertical black dotted lines denote the positions on which the data is split up into individual blocks.*

for the Rb MOT, providing an accuracy for the wavelength determination of $\pm 0.5 \cdot 10^{-3}$ nm ($\approx 4 \cdot 10^{-3}\,\mathrm{cm}^{-1}$ near 795 nm). The wavelength determination is done by a microcontroller which provides the wavelength in ASCII encoding over standard serial bus. This is besides several displays around the lab connected to our datalogging system. The datalogger records the wavelength and up to 5 more analog input channels with 16 bit precision. Fig. 3.15 (b) shows the wavelength during a typical scan.

If the two lasers are less than 2 GHz detuned from each other, it is possible to use the beat frequency instead of the wavemeter. For that purpose, we use a LabView based program to read out a spectrum analyzer and record the beat note and a timestamp. This information is then inserted in the datasets at the place of the wavemeter data. Fig. 3.16 shows a typical scan with (a) the wavemeter and (b) with the beat frequency method which is much more accurate, providing an accuracy of $\pm 2 \cdot 10^{-4}\,\mathrm{cm}^{-1} \approx 6$ MHz.

In the current setup, we record, amongst the wavelength, the Rb MOT fluorescence which is monitored by a photodiode, the Yb MOT fluorescence monitored by a photomultiplying tube and the scan control voltage. Fig. 3.15 shows the data from a typical experimental measurement: (a) shows the scan control voltage. It is clearly visible that a scan with a

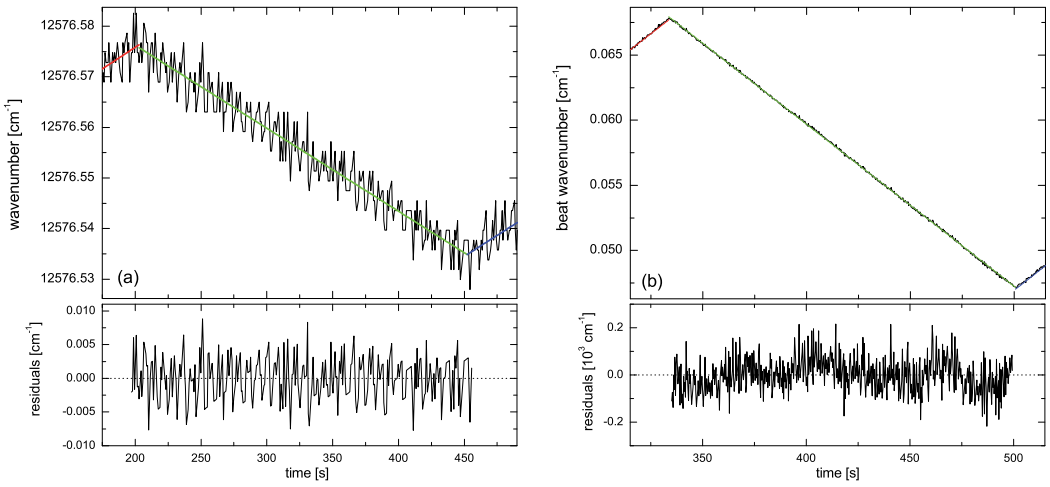

Figure 3.16.: *A typical fit to determine the wavelength of the scan. In (a), the wavemeter is used. The cycling of the measured wavelength is clearly visible. The wavemeter sometimes fails to compute the wavelength which results in a completely off-value which is identified and deleted. This method gives the absolute value of the wavelength of the laser and is already converted to wavenumbers here. In (b), the beat signal of the two laser beams is recorded by a spectrum analyzer and is used as the basis for the fitting routine. This method gives directly the difference of the two lasers. Note the different scale of the two graphs. The estimated error of the wavemeter is about* $4 \cdot 10^{-3}$ cm^{-1} *in this wavelength regime, while the error of the second method is less than* $2 \cdot 10^{-4}$ cm^{-1}.

frequency of 2 mHz was performed. In (b), the wavelength determined by the wavemeter is shown. The accuracy of about $\pm 0.5 \cdot 10^{-3}$ nm is reflected by the noise on the signal. The Yb fluorescence signal (c) shows a broad peak. The Rb fluorescence signal (d) is not showing any effects of the two lasers.

At the beginning of a scan, the two lasers for photoassociation are blocked for a short time. Thus, the two MOTs are not disturbed by these lasers anymore and the atom number increases to the maximal loading number. This gives information about the signal when 100 % of the atoms are present. Afterwards, the slowing beam for Yb is blocked for a short time. Thus, the atom number drops to zero in the combined MOT and the photomultiplier only measures the background signal. This will be set equal to 0 % of atoms, see fig. 3.17 (a) for an example. These two information are needed to calculate relative atom numbers.

After the measurement, the resulting data file is analyzed in an OriginPro script. In the first step, the wavemeter data is analyzed. The evaluation of the interferometer data of the wavemeter and the transport via the serial bus delays the information by nearly a second which is corrected by the analysis script. In the next step, outliers of the wavelength caused by a miscount of the electronics are removed. The scan control voltage (see fig. 3.15 a) is analyzed and the positions of the maxima and minima is determined. The data for the atom numbers in Rb and Yb and the wavemeter data is then split up into individual

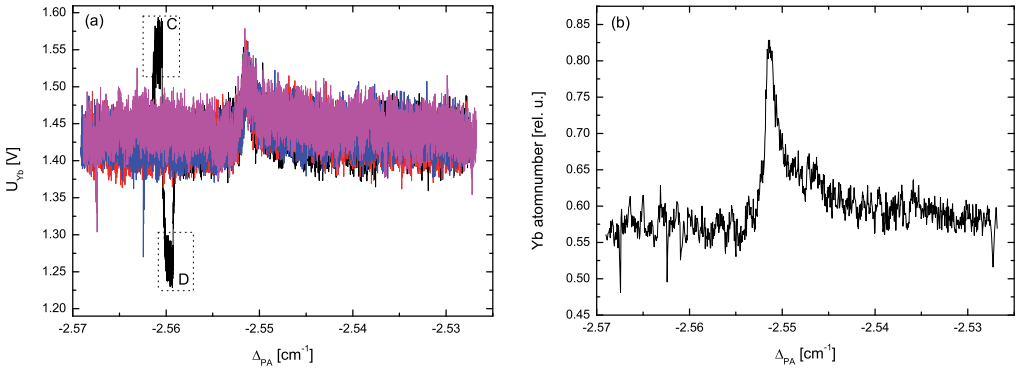

Figure 3.17.: *A typical photoassociation Yb signal, already cut at the turning points of our scan. The x-axis is already converted to the relative wavenumber determined by the wavemeter. (a) The individual scans. In the first scan (the black curve) the two lasers got blocked for a short time, indicated by the rectangular C. This results in a higher atom number in the Yb MOT since there are no losses from photoassociation processes. Afterwards, the slowing beam got blocked for a short time giving us the background signal of the photodiode, indicated in the rectangular D. This method is used to get the relative atom numbers. For the smoothing routine, this data will be deleted. (b) the averaged data of the single scans.*

blocks. A linear fit is performed to the wavemeter data of each individual block. The fitting parameters are then used to convert the timestamps of the Yb and Rb signal to wavelengths giving an accuracy of about $4 \cdot 10^{-3}\,\mathrm{cm}^{-1} \approx 120\,\mathrm{MHz}$ when the wavemeter is used respective an accuracy of $\pm 6\,\mathrm{MHz} \approx \pm 2 \cdot 10^{-4}\,\mathrm{cm}^{-1}$, as shown in fig. 3.16. This accuracy is most likely the laser stability, as our locking system does provide a stability of 5 MHz.

After this, each single sweep is available in the worksheet of an Origin project. It is therefore easy to delete data that has obvious errors in it (e.g. one laser is not resonant anymore) or the data that is due to the measurement of the relative atom numbers in Yb as explained before. In fig. 3.17 (a), all available sweeps of one dataset are shown. In the black curve, the measurements for the relative atom numbers were performed. This data is deleted before the sweeps get combined. Sometimes it is necessary to shift the sweeps to each other since the accuracy of the wavelength determination is about $4 \cdot 10^{-3}\,\mathrm{cm}^{-1}$. This can be done manually by overlapping the sweeps. In most of the cases, this is not needed or only much less than the accuracy of the wavelength determination. After that procedure, the data gets combined and averaged which minimizes the signal noise. Fig. 3.17 (b) shows an example of the finally used signal of an Yb peak.

4.

1-Photon-Photoassociation

In this chapter, the previously published results of the 1-Photon-Photoassociation [93] of ^{174}Yb and ^{176}Yb with ^{87}Rb will be reviewed. The Photoassociation was performed near the Rb $|^2S_{1/2}\rangle \rightarrow |^2P_{1/2}\rangle$ transition at 795 nm. In addition to the previous results, we performed 1-Photon-Photoassociation spectroscopy for two more bosonic Ytterbium isotopes. These results give more information about the potential of the excited state of the isotopologue $^xYb^{87}Rb$ which is a needed information for the 2-Photon-Photoassociation that is the main part of this thesis and will be discussed in the next chapter.

Furthermore, photoassociation of ^{176}Yb and ^{87}Rb near the D_2-transition at 780 nm was performed and the results will be presented.

4.1. Introduction

In the process called photoassociation, two colliding atoms A and B form an excited molecule with the help of a photon [25]:

$$A + B + \hbar\omega_L \rightarrow AB^* \tag{4.1}$$

With this technique, it is possible to excite two atoms to a specific vibrational and rotational molecular level. This process is schematically shown in fig. 4.1. The frequency difference of the photoassociation (PA) laser to the dissociation limit of the atomic transition corresponds to the binding energy of the molecular state.

The two atoms that form the molecule do not change their distance to each other during the photoassociation process. Therefore, the internuclear distance required for the process is determined by the vibrational level of the molecule. That is the reason that the photoassociation process is more probable for a high-lying molecular vibrational level that has a large average internuclear distance. This also means that it is (nearly) impossible to create deeply bound molecules with a 1-Photon-Photoassociation process.

In the current experimental setup, the two MOTs are continuously loaded by a Zeeman slower (see chapter 2 for details). A photodiode monitors the fluorescence of the Rb MOT which is directly connected to the atom number. A photomultiplying tube is monitoring the Yb fluorescence which determines the atom number. The PA laser is superimposed on the two MOTs and creates excited molecules if it is on a molecular resonance. An excited photoassociated molecule decays after a short time either into a ground state molecule

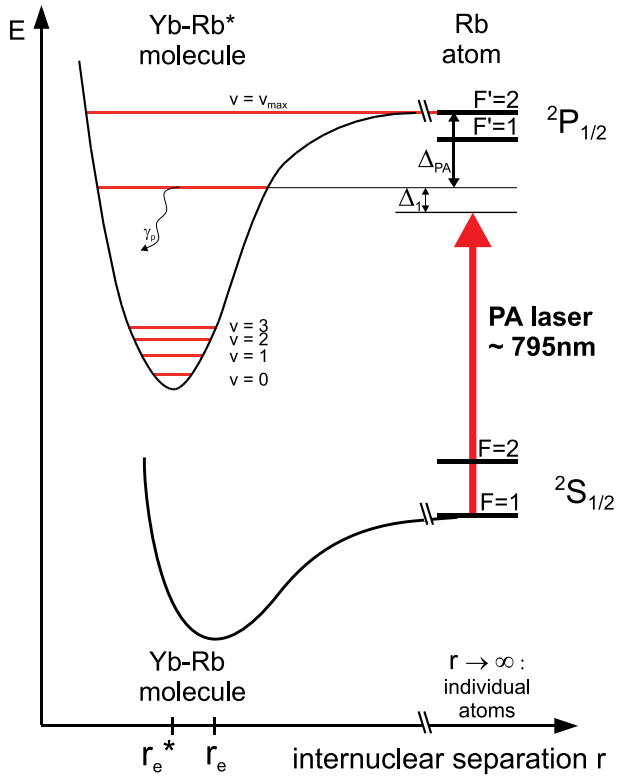

Figure 4.1.: *Illustration of 1-Photon-Photoassociation. The PA laser is red detuned to the Rb D_1 transition at about 795 nm. The frequency difference between the transition from $F = 1$ to $F' = 2$ and the PA laser is called Δ_{PA}. The excited bound state can decay by spontaneous emission with the rate γ_p. Δ_1 is the detuning of the photoassociation laser to the bound state.*

which then leaves the cycling cooling transition and is not trapped anymore in the MOT or into two atoms with kinetic energies high enough to leave the MOT. In both cases, the two atoms are lost from the MOT. Thus, the PA laser induces an additional loss channel to the MOT leading to a steady state with a lower atom number. This can be monitored by the fluorescence signal. Due to the large imbalance in atom number in the two species (10^8 Rb atoms, but only 10^5 Yb atoms), the losses in the Rb signal are small and it is not possible to see a YbRb photoassociation resonance on the Rb fluorescence signal, but we see it in the Yb signal. Since we are working near a Rb transition, it can be spaced out that the resonances we found belong to Yb_2 photoassociation. A typical spectrum is shown in fig. 4.2. The upper graph shows a scan over a lot of vibrational levels. The lower graphs zoom in on two specific vibrational levels that are used in the 2-Photon-Photoassociation experiments (see chapter 5). It is clearly visible that the hyperfine structure of the excited atomic Rb state is conserved (although it starts getting narrower [3]). A rotational structure with levels of up to $R' = 1$ is visible as well as a splitting of the rotational levels.

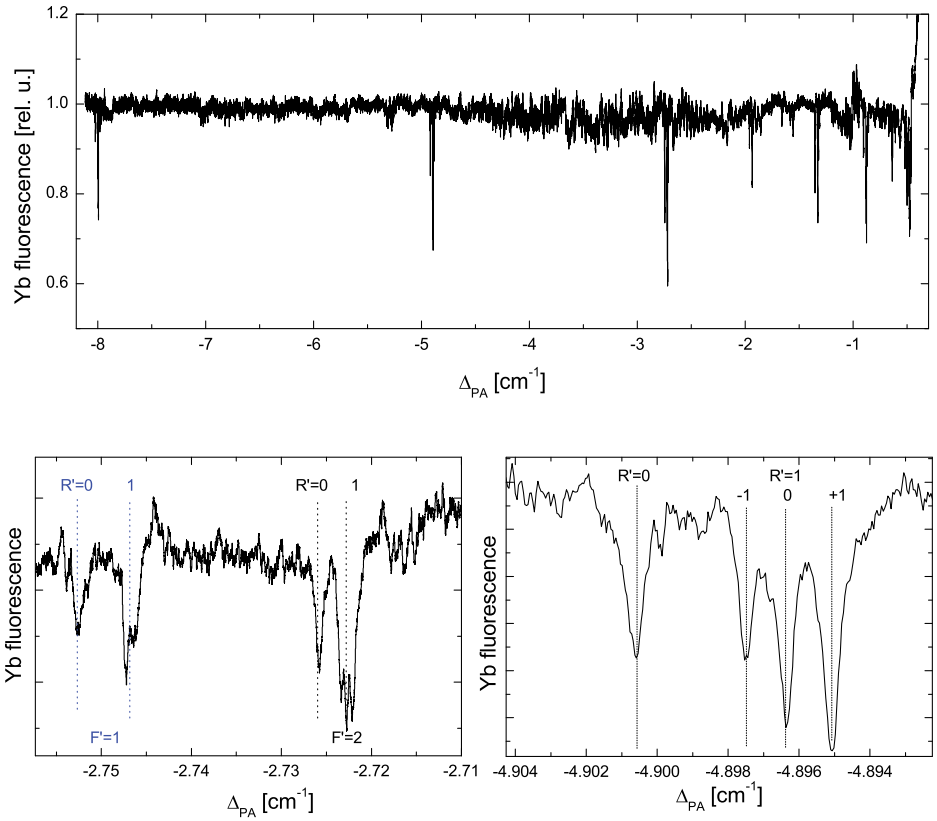

Figure 4.2.: *Upper graph: Spectrum of the 1-Photon-Photoassociation of* $^{176}Yb^{87}Rb$ *(from [3]). Lower graphs: two vibrational level. The hyperfine structure from the Rb atom and the rotational structure with levels up to* $R' = 1$ *is clearly visible. Additionally, the rotational levels are splitting up into subcomponents.*

4.2. Line Shape

A full quantum close coupling calculation [94] yields the following equation for the scattering probability of one PA resonance:

$$|S_p(\epsilon, l, \Delta_1, I_1)|^2 = \frac{\gamma_p \gamma_s(\epsilon, l, I_1)/(2\pi)^2}{(\epsilon/\hbar - \Delta_1)^2 + (\gamma/4\pi)^2} \tag{4.2}$$

Here, Δ_1 is the relative detuning of the PA laser from the position E_b of the bound state, Δ_1 is positive for a red detuned PA laser ($\hbar\omega < E_b$), see fig. 4.1. For low intensities, Fermi's golden rule gives

$$\gamma_s(\epsilon, l, I_1) = \frac{2\pi V_1^2 |\langle \epsilon, l|b\rangle|^2}{\hbar}. \tag{4.3}$$

The kinetic energy of the colliding atoms is $\epsilon = \hbar^2 k^2/2\mu$ and $\gamma = \gamma_s(\epsilon, l, I_1) + \gamma_p + \gamma_0$ is the total width of the excited state. γ_p is the natural linewidth of the transition and $\gamma_s(\epsilon, l, I_1)$ is the stimulated emission induced by the PA laser back to the ground state. γ_0 is due to

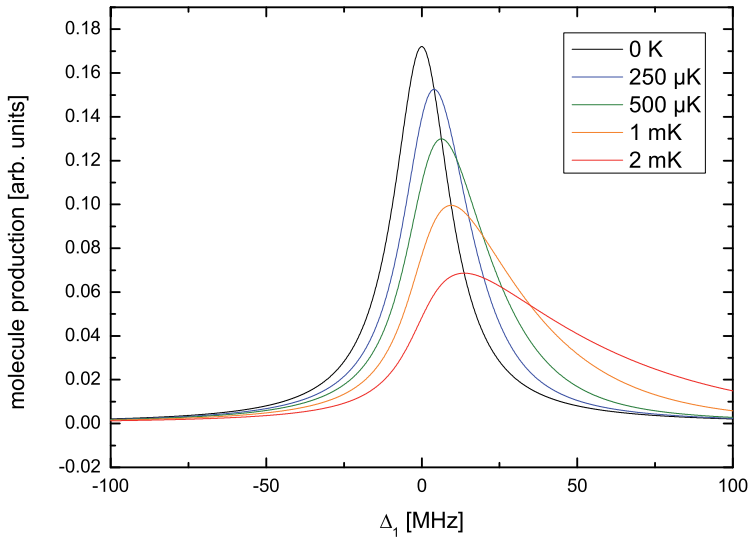

Figure 4.3.: *Temperature dependence of the line shape of a Photoassociation resonance according to eqn. (4.4). The temperature has a clear effect on the red side of the line and on the position of the maximum. The difference between the (black) zero temperature curve and the (blue) curve at the temperature of* 250 μK *is only* 3.9 MHz *which is much less than the resolution of our wavemeter and therefore can be neglected.*

all other possible processes e.g. molecular predissociation. This is typically a small value and will be neglected in this work. $V_1(R) = (\frac{I_1}{2\epsilon_0 c})^{1/2} d_1(R)$ is the radiative coupling matrix element, depending on the laser intensity I_1 and the molecular transition dipole $d_1(R)$. $|\langle \epsilon.l|b\rangle|^2$ is the Franck-Condon factor for the free-bound transition.

Thermal averaging of the ensemble leads to the following term giving the molecular production rate [94]:

$$K = h \int |S_p(\epsilon, l, \Delta_1, I_1)|^2 \, e^{-\epsilon/k_B T} \frac{d\epsilon}{k_B T} \tag{4.4}$$

The solution of this numerically solved integral is shown in fig. 4.3. The temperature has a clear effect on the lineshape and also on the position of the resonance. The resonance is shifted by 3.9 MHz for a temperature of 250 μK, 6.3 MHz for 500 μK, 9.5 MHz for 1 mK and 13.6 MHz for 2 mK. The shift of resonance is small compared to the accuracy of our wavemeter and can therefore be neglected.

4.3. Line Assignment

The lower graphs of fig. 4.2 show typical resonances found in 1-Photon-PA experiments. All found resonances for all examined Yb isotopes have a similar structure for 1-Photon-PA

experiments at the D_1 line of Rb near 795 nm. Experiments done at the D_2 line show a different behavior and will be discussed later.

4.3.1. Hyperfine Structure

The 1-Photon-PA resonances always appear in pairs that are split by approximately $0.027\,\mathrm{cm}^{-1}$. This value is close to the hyperfine splitting of the atomic Rb, where the literature value is $2.717 \pm 0.015 \cdot 10^{-2}\,\mathrm{cm}^{-1}$ [59]. The atomic properties are often still visible in weakly bound molecules, since the long-range character of the molecule changes atomic properties only slightly. This coupling, where the atomic angular momenta do not couple to the internuclear axis, is best described by Hund's case (e). Deeper bound molecules will show a different coupling, mostly Hund's case (a) or (b), but we were not able to explore these deeply bound levels. A hint for the changing of coupling can be seen by the more bound vibrational level: The hyperfine splitting slightly decreases to about $0.023\,\mathrm{cm}^{-1}$ [3].

4.3.2. Rotational Structure

The rotational energy of a molecule is defined as

$$E_{rot} = B_{rot}\, R \cdot (R+1) \tag{4.5}$$

where R is the rotational quantum number of the nuclear motion and B_{rot} is the rotational constant, as defined in equation (2.28):

$$B_{\mathrm{rot}} = \frac{\hbar^2}{2\mu r^2}$$

The rotational structure is clearly visible for the components $R = 0$ and $R = 1$. The $R = 2$ component is nearly not visible in the spectrum, higher rotational levels do not appear. This is due to the temperature of our atom clouds with $T_{\mathrm{Rb}} \approx 120\,\mu\mathrm{K}$ and $T_{\mathrm{Yb}} \approx 400\,\mu\mathrm{K}$ (see chap. 3). The relevant effective temperature is then [2]

$$\bar{T} = \frac{m_{\mathrm{Rb}} T_{\mathrm{Yb}} + m_{\mathrm{Yb}} T_{\mathrm{Rb}}}{m_{\mathrm{Yb}} + m_{\mathrm{Rb}}} \approx 210\,\mu\mathrm{K} \tag{4.6}$$

which is the well below the centrifugal barrier of $360\,\mu\mathrm{K}$ for the $R' = 2$ component (see chap. 2.2.5). In previous experiments [3], we worked at higher temperatures of the atom clouds which made the $R' = 2$ component more pronounced, see the comparison of different temperatures for the photoassociation in fig. 4.4.

4.3.3. Splitting of the rotational components

Our data shows a splitting of rotational components into subcomponents. A detailed view shows that for each rotational component we get for the $F' = 1$ state $1, 3, 3$ substates while for the $F' = 2$ state, there are $1, 3, 5$ substates. This let us come to the assumption, that a coupling between F' and R' causes this splitting. This confirms the Hund's case (e) coupling, where at first all atomic angular momenta couple to F' and then this couples to R'. A detailed discussion of this splitting can be found in [3].

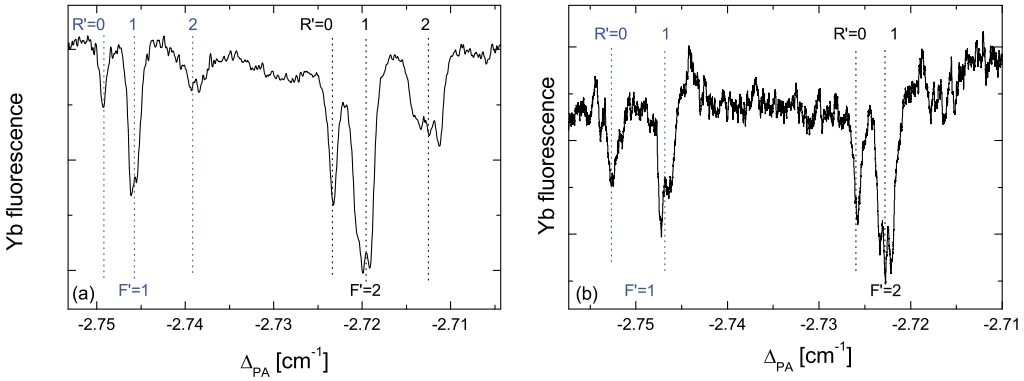

Figure 4.4.: *1-Photon-Photoassociation resonance in* $^{176}Yb^{87}Rb$ *at* $\Delta_{\mathrm{PA}} = -2.72\,\mathrm{cm}^{-1}$. *(a) Previous data from [3] with an effectivetemperature of* $\bar{T} \approx 400\,\mu$K *[3] and (b) data with* $\bar{T} \approx 210\,\mu$K *from this work. The rotational structure shows only components up to* $R' = 1$ *due to the centrifugal barrier of* $361\,\mu$K.

4.3.4. Vibrational Structure

The positions of the vibrational levels can be computed by an approximation introduced by LeRoy and Bernstein [6]. As already described in chapter 2.2.3, a C_6 value describes the potential in the long-range regime and defines the vibrational level by the following equation:

$$E(V) \approx E_D - \left((v_D - v) \cdot \sqrt{\frac{\pi}{2\mu}} \cdot \frac{\Gamma(1+1/n)}{\Gamma(1/2+1/n)} \cdot \frac{\hbar(n-2)}{(-C_n)^{1/n}} \right)^{\frac{2n}{n-2}} \tag{4.7}$$

A fit to our data gives a value of [3]

$$\begin{aligned} C_6 &= -(5684 \pm 98)\,\mathrm{E_h a_0^6} \\ v_D &= 0.278 \pm 0.031. \end{aligned} \tag{4.8}$$

The plot of the function is shown in fig. 4.5.

4.4. Isotopic effects on Photoassociation

In [3], we performed the 1-Photon-PA experiments in YbRb with the two isotopes ^{176}Yb and ^{174}Yb. In preparation for the 2-Photon-PA experiments, we performed 1-Photon-PA spectroscopy for ^{170}Yb and ^{172}Yb as well. In general, the structure of the found resonances is the same as for ^{176}Yb for all examined isotopes. We performed the 1-Photon-PA experiments on the same vibrational state for each isotope[1].

[1] Due to the mass of ^{176}Yb^{87}Rb, it is $\Delta v' = -7$ for this isotopologue while it is $\Delta v' = -6$ for the other combinations, because it exhibits one more vibrational state.

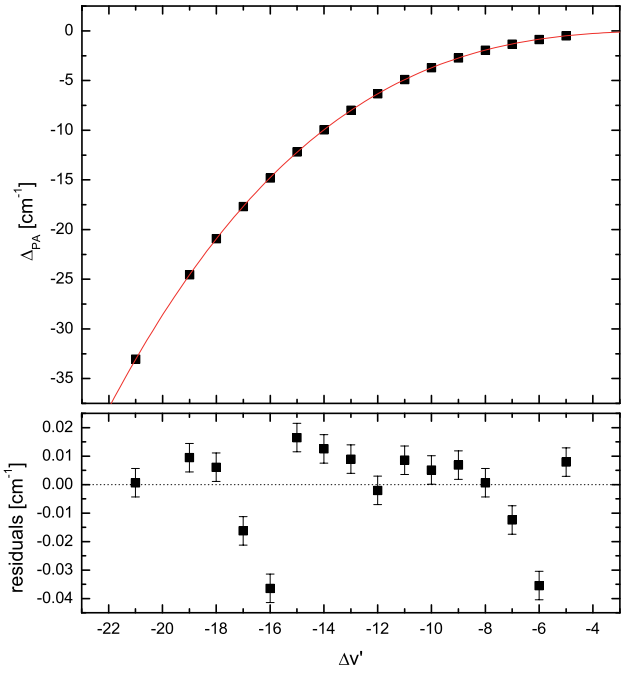

Figure 4.5.: *Vibrational level of the excited $^{176}Yb^{87}Rb$ molecule. Adapted from [3, 93].*

In experiments with ^{174}Yb and ^{87}Rb, the found resonances appear to be smaller compared to ^{176}Yb. A sample resonance scan is shown in fig. 4.7. This resonance was used for the 2-Photon-PA spectroscopy.

In ^{172}Yb, a deep, very loosely bound resonance was found. Fig. 4.6 (b) shows this resonance. The hyperfine structure of Rb is clearly visible as well as a rotational structure up to $R' = 3$, which is more than expected. One reason could be, that the strength of this free-bound transition is very high and therefore the tunneling process through the centrifugal barrier is sufficient to create molecules with larger angular momentum.

Since the natural abundance of ^{170}Yb is only 3 %, the signal is lower but still sufficient for this kind of experiments. A typical 1-Photon-PA scan is shown in fig. 4.6 (a).

The depicted resonances are exhibiting well the expected mass dependence of a vibrational state. Fig. 4.8 shows the potential of ^{x}Yb^{87}Rb with the additional states belonging to the different isotopes included. The potential of the molecular state which is determined by electronic interactions does not change with the isotopes, therefore the C_6 coefficient calculated for ^{176}Yb is still valid for the other isotopes. In the LeRoy-Bernstein formula, the only two things that change are the fractional part v_D of the vibrational state and the reduced mass. Tab. 4.1 lists this number for all examined Yb isotopes.

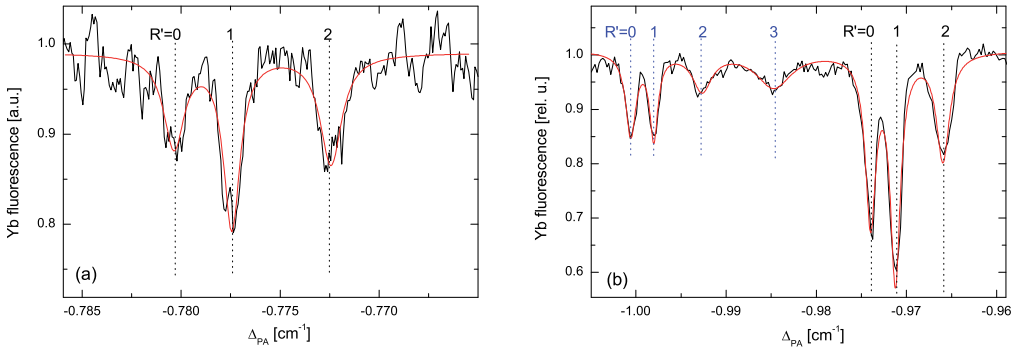

Figure 4.6.: *1-Photon resonance for (a) $^{170}Yb^{87}Rb$ with a rotational structure up to $R' = 2$ and (b)$^{172}Yb^{87}Rb$. The hyperfine structure of the excited Rb state is clearly visible as well as the rotational levels, in blue: $F' = 1$, in black: $F' = 2$.*

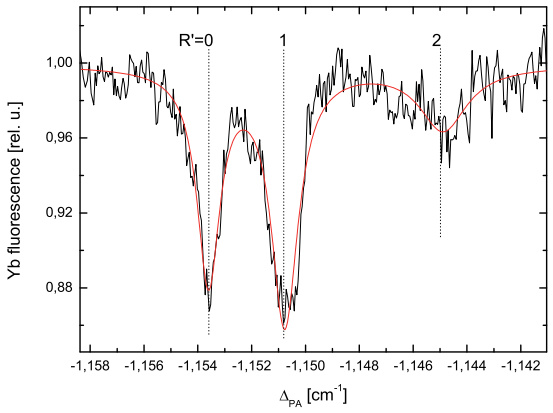

Figure 4.7.: *1-Photon Resonance for ^{174}Yb and^{87}Rb. A rotational structure until $R' = 2$ is visible.*

Yb isotope	v_D
170	0.13
172	0.58
174	0.928
176	0.274

Table 4.1.: *The fractional part v_D of the LeRoy-Bernstein formular for different Yb isotopes.*

Yb isotope	vibrational state $\Delta v'$	Δ_{PA} in cm^{-1}	B_{rot} in $10^{-3}\,\mathrm{cm}^{-1}$
170	-6	-0.783	1.25
172	-6	-0.974	1.34
174	-4	-0.42490	1.02
	-5	-0.72800	1.09
	-6	-1.1486	1.40
	-7	-1.70310	1.47
	-8	-2.43700	1.67
	-10	-4.45900	1.95
	-12	-7.38365	2.33
176	-5	-0.49440	0.85
	-6	-0.88090	1.45
	-7	-1.32980	1.34
	-8	-1.93810	1.48
	-9	-2.72330	1.65
	-10	-3.70710	1.66
	-11	-4.89710	2.00
	-12	-6.33330	2.00
	-13	-8.00080	2.45
	-14	-9.94940	2.47
	-15	-12.19230	2.90
	-16	-14.80770	2.98
	-17	-17.68660	3.14
	-18	-20.92110	3.30
	-19	-24.5534	3.35
	-21	-33.0554	3.60

Table 4.2.: *Properties of all excited states found in* $^{x}Yb^{87}Rb$. *The position is given for the* $F' = 2, R' = 0$ *state with an accuracy of* $\pm 5 \cdot 10^{-3}\,\mathrm{cm}^{-1}$. *The values for* ^{174}Yb *and* ^{176}Yb *are taken from [3].*

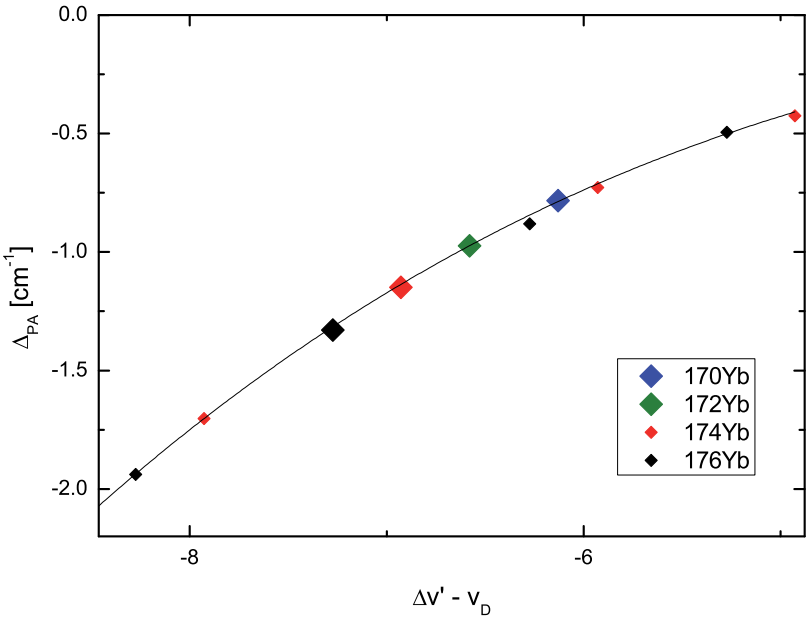

Figure 4.8.: *Positions of vibrational levels of different Yb isotopes. The potential does not change with different isotopes except for the v_D constant and the reduced mass. The fit is the potential for ^{176}Yb as described before. The resonances of the different Yb isotopes belonging to the same vibrational level are emphasized.*

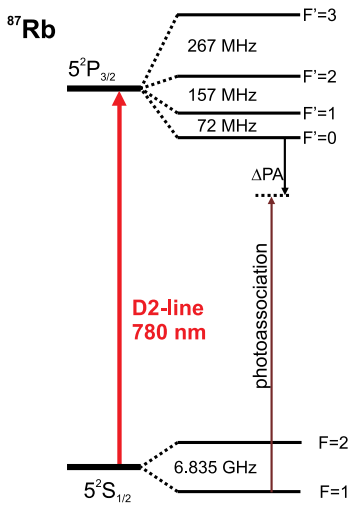

Figure 4.9.: *Photoassociation experiments at the D_2 transition of Rb. $\Delta^*_{\mathrm{PA}} = 0$ is defined as the transition from $F = 1$ to $F' = 0$.*

4.5. 1-Photon-Photoassociation at the D_2-transition

In principle, photoassociation experiments could be done close to any atomic transition of the involved atoms. Besides experiments at 795 nm at the D_1 transition of Rb, we also investigated the possibility for photoassociation close to the D_2 transition near 780 nm. The excited state of this transition exhibits four hyperfine levels of Rb, with distances in the range of the rotational spacing, see fig. 4.9. From now on, $\Delta^*_{PA} = 0$ is defined as the transition from $|S_{1/2}, F = 1\rangle \rightarrow |P_{3/2}, F' = 0\rangle$ at 12816.6818 cm^{-1}. We found three resonances with a completely different structure than the ones at the D_1 transition. Fig. 4.10 shows these resonances.

Exact and trusted properties of the potential can not be made with these three resonances. But ab-initio calculations (see fig. 2.3) show that the potential of this state is similar to the $^2\Pi_{1/2}$ state we examined at the D_1 transition. We can give an estimation of the C_6^* coefficient with the LeRoy Bernstein formalism, which also gives information about

$\Delta v'^*$	Δ^*_{PA}
-5	-0.4297
-8	-1.742
-9	-2.496

Table 4.3.: *Properties of the found resonances at the D_2 transition. The accuracy of the given resonances is $\pm 5 \cdot 10^{-3}$ cm^{-1}.*

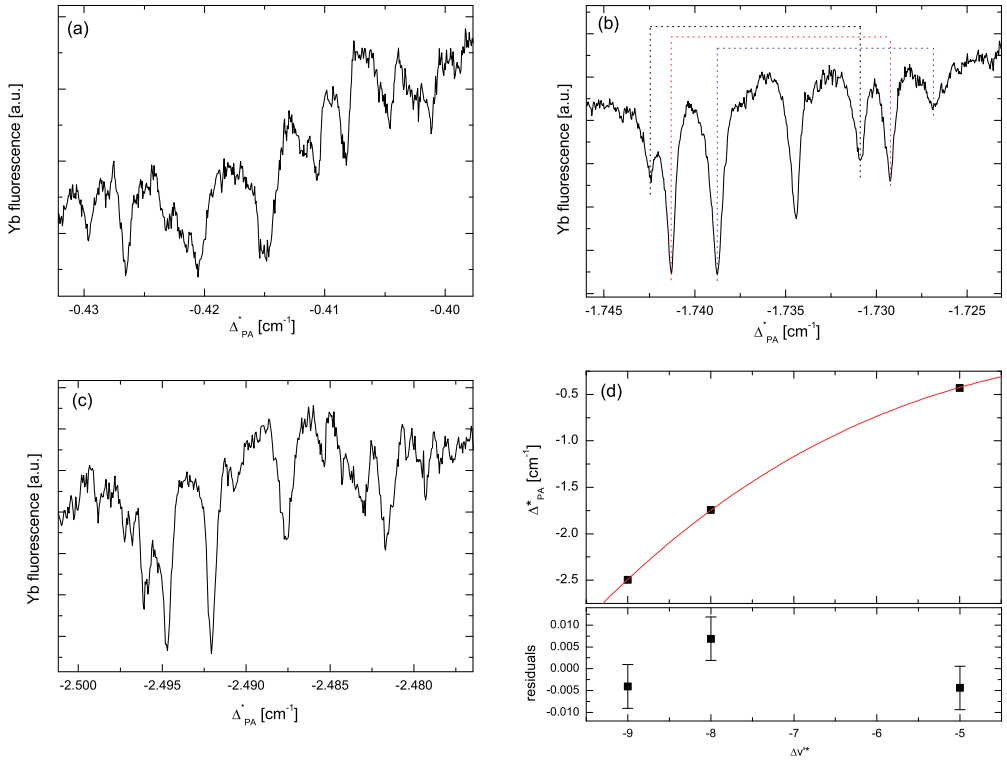

Figure 4.10.: *(a) - (c): All found photoassociation resonances in the regime up to* $\Delta_{\mathrm{PA}} = -3\ \mathrm{cm}^{-1}$*. In (b), the possible "echoes" are shown. (d): Fit to the LeRoy-Bernstein equation using the most deeply bound peak from each resonance. This leads to* $C_6 = -(5610 \pm 250)\ \mathrm{E_h a_0^6}$ *and* $v_D = 0.02$*.*

the relative vibrational level $\Delta v'^*$ by using the three resonances we found. We got

$$\begin{aligned} C_6^* &= -(5610 \pm 250)\ \mathrm{E_h a_0^6}, \\ v_{\mathrm{D}}^* &= 0.02 \pm 0.07. \end{aligned} \tag{4.9}$$

This was fitted using the most deeply bound peak in each resonance which is probably the $R'^* = 0$ component. The positions and the belonging vibrational levels are given in tab. 4.3.

The structure of the resonances is not fully understood yet. It is remarkable that the first three peaks seem to have each an "echo", that are the last three peaks. This is shown in fig. 4.10 (b) as an example.

Since the structure of these resonances is much more complicated in comparison to the D_1 transition, we did not see any advantages to use this transition. Therefore, we did not pursue this possibility anymore and did not try to use this transition in 2-Photon-Photoassociation experiments.

5.

2-Photon-Photoassociation

In this chapter, the experimental results of our 2-Photon-Photoassociation studies are presented. The 2-Photon-Photoassociation studies were performed in a double species MOT using a trap-loss technique which is based on the one used for 1-Photon-Photoassociation. From the 2-Photon-Photoassociation spectra information about the potential of the ground state molecule YbRb is obtained.

5.1. Principle of 2-Photon-PA spectroscopy

2-Photon-Photoassociation spectroscopy probes a state in an atom or molecule through an auxiliary state. In the heteronuclear case, the simplest way is to prepare two atomic species in a continuously loaded two-species MOT. After a loading time of a few seconds, the two clouds reach their steady state values in temperature and atom number. The atom number can be monitored easily by the fluorescence of the MOT.

The first step to observe 2-Photon-Photoassociation is to apply the PA laser to the double-species MOT on resonance with a specific free-bound transition which causes a permanent creation of electronically excited molecules (see chapter 4). This leads to a steady state of the MOT with a lower atom number as a permanent additional loss is introduced. In the next step, a probe laser is superimposed with a lower wavelength than the PA laser. This laser couples the excited bound state to a vibrational level of the molecular ground state. Whenever the laser is resonant with such a bound-bound transition, the excited level is perturbed by lightshift effects. A shift of the resonance occurs and thus, the PA laser which is fixed to the unperturbed system is not resonant anymore. This causes a lower production rate for the molecules in the excited state and therefore, the atom number in the MOT increases. The energy difference of the PA and the probe laser gives the binding energy of the vibrational level of the electronic ground state. Fig. 5.1 shows this technique. The PA laser is fixed slightly below the D_1 transition of Rb near 795 nm to a transition from free atoms to a vibrational level of the electronically excited molecular state $^2\Pi_{1/2}$. The probe laser is scanned and whenever it is on resonance, it shifts the molecular level and therefore shifts the PA laser out of resonance which will be noticed as an increase of atom numbers. The 2-Photon-Photoassociation spectroscopy was first demonstrated in 1995 [95] in a mixture of homonuclear ^{7}Li.

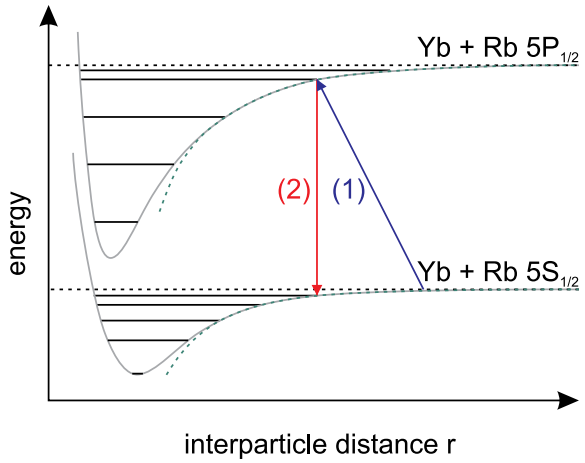

Figure 5.1.: *Principle of 2-Photon-Photoassociation spectroscopy: The PA laser (1) is fixed to a 1-Photon-PA resonance producing molecules in the electronically excited state and the probe laser (2) couples this bound state to a bound state in the electronic ground state. When on resonance, this laser shifts the energy levels of the molecule and the PA laser (1) is out of resonance causing less molecule production. Adapted from [3].*

5.2. Strong light field interaction with a molecular transition

Autler and Townes [96] showed that a transition can split up into two components when one of the used levels is coupled to a third one by a light field[1]. This splitting leads to a shift of the resonance. This effect is utilized in 2-Photon-Photoassociation experiments. This so called Autler-Townes splitting is explained in many textbooks, such as [56, 97] and is subject of many lectures to quantum optics. I will follow these lectures [98, 99] to explain this effect. We start with a system that is reduced to an atom with three levels $|a\rangle$, $|b\rangle$, $|c\rangle$ with the energies $\hbar\omega_a$, $\hbar\omega_b$ and $\hbar\omega_c$ and no spontaneous emission. This system has two allowed transitions (see fig. 5.2). The transition $|b\rangle \leftrightarrow |c\rangle$ with transition frequency ω_{cb} is probed by a weak laser field $\omega_{L,cb}$. The transition $|a\rangle \leftrightarrow |b\rangle$ has the frequency ω_{ab} and is driven by a strong laser field with frequency ω_L with a relative detuning

$$2\pi\delta = \omega_L - \omega_{ab} \tag{5.1}$$

which is small compared to ω_{ab}, ω_{cb} and the difference $\omega_{ab} - \omega_{cb}$ to ensure that this laser field is nonresonant with the transition $|c\rangle \leftrightarrow |b\rangle$. Due to the interaction between the states $|a\rangle$ and $|b\rangle$, the transition $|c\rangle \leftrightarrow |b\rangle$ is also modified. To quantify this modification, we neglect for now the probe transition (and level $|c\rangle$) and only consider a two-level atom with the wavefunction:

$$\Psi(\vec{r}, t) = c_a(t)e^{-i\omega_a t}u_a(\vec{r}) + c_b(t)e^{-i\omega_b t}u_b(\vec{r}) \tag{5.2}$$

[1] Autler and Townes described a microwave transition, but the effect is the same for a light field which is used in this experiment.

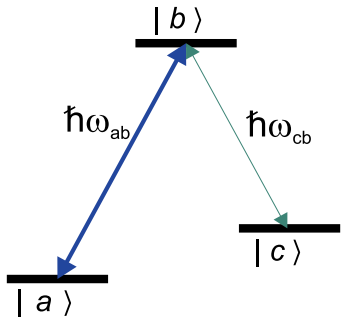

Figure 5.2.: *Three level atom. The transition $|a\rangle \leftrightarrow |b\rangle$ is driven by strong laser field ω_{L} and the transition $|c\rangle \leftrightarrow |b\rangle$ is probed by a weak laser field $\omega_{L,cb}$.*

$u_a(\vec{r})$ and $u_b(\vec{r})$ are the two eigenfunctions of the two states with the energy E_a and E_b with $E_b > E_a$. The time-dependent wave equation can then be calculated by the Schrödinger equation

$$i\hbar\dot{\Psi} = \hat{H}\Psi = \left(\hat{H}_{\mathrm{at}} + \hat{H}_{\mathrm{int}}\right)\Psi \tag{5.3}$$

where $\hat{H}_{\mathrm{at}}$ is the atomic Hamiltonian containing all internal interactions and $\hat{H}_{\mathrm{int}}$ is the interaction Hamiltonian. We neglect all kinetic terms of the atomic Hamiltonian:

$$\hat{H}_{\mathrm{at}} u_i(\vec{r}) = \hbar\omega_i u_i(\vec{r}) \tag{5.4}$$

The light field

$$\vec{E}_L = \vec{\epsilon} E_0 \cos\left(\omega_L t - \vec{k}_L \cdot \vec{r}\right) \tag{5.5}$$

which is driving the transition $|a\rangle \leftrightarrow |b\rangle$ with the amplitude E_0, the polarization vector $\vec{\epsilon}$ and the laser frequency ω_L interacts with the wavefunction through the dipole interaction. The light field changes only slightly over the range of the atom, so that we can use the dipole approximation where $\vec{E}_{\mathrm{L}}$ is taken as constant in space and depends only on time:

$$\hat{H}_{\mathrm{int}} = -\vec{d} \cdot \vec{E}(t) \tag{5.6}$$

Here, we introduced the dipole operator $\vec{d} = -e\vec{r}$. If we now substitute eqn. (5.2) into (5.3), we get

$$\begin{aligned} \dot{c}_a(t) &= i\Omega_0^* e^{-i\omega_{ab}t} \cos(\omega_L t)\, c_b(t) \\ \dot{c}_b(t) &= i\Omega_0 e^{i\omega_{ab}t} \cos(\omega_L t)\, c_a(t) \end{aligned} \tag{5.7}$$

where

$$\Omega_0 = \frac{\vec{\epsilon} E_0}{\hbar} \cdot \langle a|\vec{d}|b\rangle = \frac{\vec{\epsilon} E_0}{\hbar} \cdot d_{\mathrm{ab}} \tag{5.8}$$

is the resonant Rabi frequency of the system and ω_{ab} is the transition frequency between $|a\rangle$ and $|b\rangle$. The Rabi frequency can be assumed to be real, that means $\Omega_0^* = \Omega_0$. If we

apply the rotating-wave-approximation which is valid if $\omega_L \approx \omega_{ab}$, we can neglect terms with the frequency $\omega_L + \omega_{ab}$ and only keep the terms with the detuning $2\pi\delta = \omega_L - \omega_{ab}$ which then gives us:

$$\begin{aligned} \ddot{c}_a(t) &= i\frac{\Omega_0}{2}e^{i2\pi\delta t}c_a(t) \\ \ddot{c}_b(t) &= i\frac{\Omega_0}{2}e^{i2\pi\delta t}c_b(t) \end{aligned} \tag{5.9}$$

If at $t = 0$ all the population is in state $|a\rangle$, one gets for the population of state $|b\rangle$:

$$|c_b(t)|^2 = \frac{\Omega_0^2}{\Omega^2}\sin^2(\Omega t/2) = \frac{\Omega_0^2}{2\Omega^2}\left(1 - \cos(\Omega t)\right) \tag{5.10}$$

Here, the generalized Rabi frequency Ω was introduced:

$$\Omega = \sqrt{(2\pi\delta)^2 + \Omega_0^2} \tag{5.11}$$

We see, that a laser field in a two-level system induces oscillations with a frequency Ω.

If we introduce spontaneous emission with the rate γ and the saturation intensity

$$I_{\mathrm{sat}} = \frac{\hbar\omega_{\mathrm{ab}}^3\gamma}{12\pi c^2} \tag{5.12}$$

to the model system, it can be shown that the Rabi frequency can be written as

$$\Omega_0 = \gamma\sqrt{\frac{I}{4I_{\mathrm{sat}}}} \tag{5.13}$$

with the intensity $I = \frac{1}{2}c\epsilon_0 E_0^2$ of the laser field.

Now, we introduce the third level and the probe laser field. The atom are now viewed in the "dressed atom" [97] picture: The atom is described by two quantum numbers: one for the eigenstates a, b or c and one for the photon number N with the energy of $\hbar\omega_L$. For example, the state $|a, N+1\rangle$ is an atom in the eigenstate a in the presence of $N+1$ photons. This state is separated from a state $|b, N\rangle$ by an energy difference

$$E_a + (N+1)\hbar\omega_L - E_b - N\hbar\omega_L = \hbar(\omega_L - \omega_{ab}) = \hbar 2\pi\delta. \tag{5.14}$$

At resonance and vanishing laser intensity, these two states are degenerate. The interaction Hamiltonian $\hat{H}_{\mathrm{int}}$ couples these two states. An atom in the state $|a\rangle$ can make a transition to the state $|b\rangle$ by absorbing one photon:

$$\langle b, N|\hat{H}_{\mathrm{int}}|a, N+1\rangle = \hbar\Omega_0 \tag{5.15}$$

with the Rabi frequency Ω_0 as before, see equation (5.8). This frequency is proportional to the laser intensity and the transition dipole moment between the states $|a\rangle$ and $|b\rangle$. The coupling due to the laser field is the reason for a splitting of the two states and leads to an avoided crossing mixing these states. Thus, the new eigenstates in the presence of the light field are the perturbed states $|1(N)\rangle$ and $|2(N)\rangle$. The energies of these two states

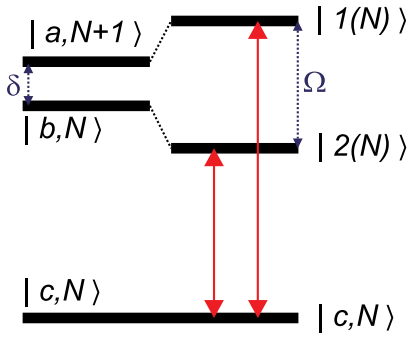

Figure 5.3.: *Dressed state picture of the system.*

are separated by the generalized Rabi frequency Ω (see eqn. (5.11)). The laser light field ω_L is nonresonant for the transition $|c\rangle \leftrightarrow |b\rangle$ and therefore, any effects of the interaction Hamiltonian on $|c, N\rangle$ can be neglected.

The weak laser field with the frequency $\omega_{L,cb}$ probes the transition $|c, N\rangle \leftrightarrow |b, N\rangle$. Because the perturbed states $|1(N)\rangle$ and $|2(N)\rangle$ are given by linear combinations of $|a, N+1\rangle$ and $|b, N\rangle$, two transitions are possible. These two transitions are separated by

$$\Delta = \frac{\Omega}{2\pi} = \sqrt{\left(\frac{\Omega_0}{2\pi}\right)^2 + \delta^2}. \tag{5.16}$$

This is the so-called Autler-Townes-Splitting, which will be investigated in detail in chapter 6. For the present chapter, it is sufficient to know, that the state $|b\rangle$ is shifted due to the laser field ω_L when on resonance with $|a\rangle \leftrightarrow |b\rangle$.

5.3. 2-Photon Photoassociation spectroscopy in YbRb

The model presented above can now be applied to the YbRb system:

- $|a\rangle$ is a vibrational level of the molecular ground state,
- $|b\rangle$ is the electronically excited molecular state addressed by the PA laser,
- $|c\rangle$ is the state of two free atoms,
- $|c\rangle \leftrightarrow |b\rangle$ is the 1-Photon-Photoassociation transition used by the PA laser and
- $|a\rangle \leftrightarrow |b\rangle$ is the 2-Photon-Photoassociation transition used by the probe laser.

A scheme of the experiment is shown in fig. 5.4. The PA laser is fixed on a 1-Photon-PA resonance with the energy $E_\mathrm{b} = E_\mathrm{res} + \Delta_\mathrm{PA}$, where E_res is the energy of the atomic resonance corresponding to the excited state hyperfine level $F' = 2$, as defined in the previous chapter. The PA laser is detuned from this resonance by Δ_1. This excited state can decay by spontaneous emission with a rate of γ_p. The probe laser is resonant with the transition of the excited state $|b\rangle$ to a ground state $|a\rangle$ with the energy $E_\mathrm{a} = E_0 + \Delta_\mathrm{bind}$

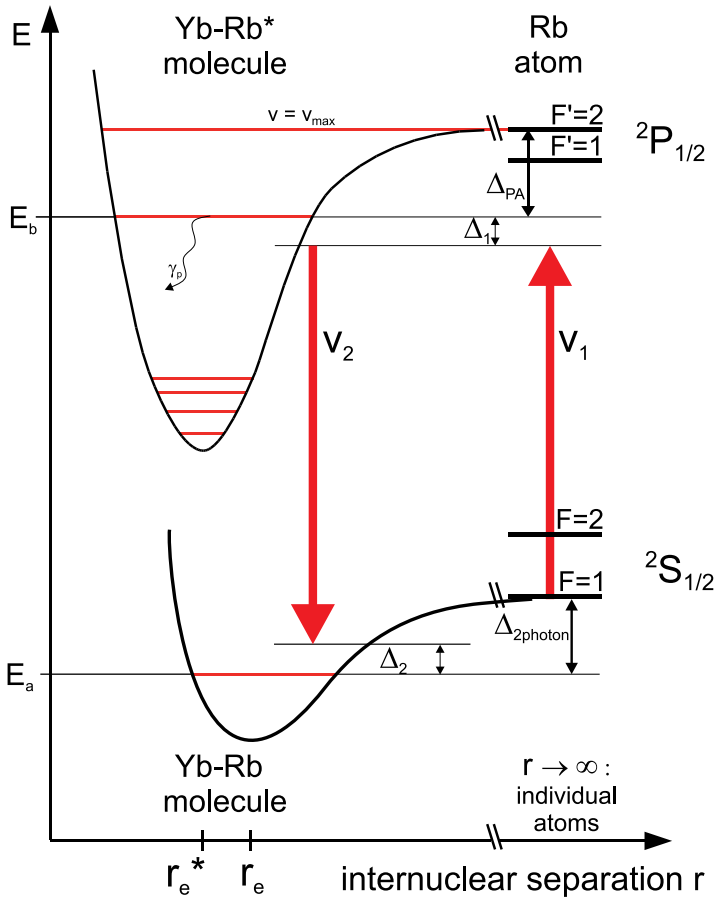

Figure 5.4.: *Schematic potential curve for the RbYb molecule (not to scale). The bound vibrational state $|b\rangle$ of the electronically excited molecule has the energy E_b and the vibrational number $\Delta v'$ which is shifted by Δ_{PA} from the Rb atomic $|^2P_{1/2}, F' = 2\rangle$ excited state. The PA laser is detuned by Δ_1 from this state. The probe laser is detuned by Δ_2 from E_a . E_a is the energy of the vibrational level with the vibrational number Δv of the electronically ground state of the molecule. The probed vibrational level of the ground state is detuned by $\Delta_{2\mathrm{photon}}$ from the $F = 1$ ground state of Rb, which is the binding energy Δ_{bind} of the 2-Photon resonance plus the hyperfine splitting, which is dependent on the state. Adapted from [3]*

with E_0 being the energy of the atomic ground state with the hyperfine level $F = 1$. From this definition, Δ_{PA} and Δ_{bind} are negative if the state is bound. The probe laser is detuned by Δ_2 from the bound state.

For a 2-Photon-Photoassociation scan, the PA laser is fixed to a specific 1-PA resonance. This leads to molecule production in the excited state and the atom number in the MOT drops. The probe laser is then superimposed to the PA laser, causing a disturbance of the excited state $|b\rangle$ as discussed above. The wavelength of the probe laser is measured with a wavemeter, giving the wavelength in absolute wavenumbers. For simplicity, the wavenumber of this laser will from now on be given as the difference of the wavenumbers

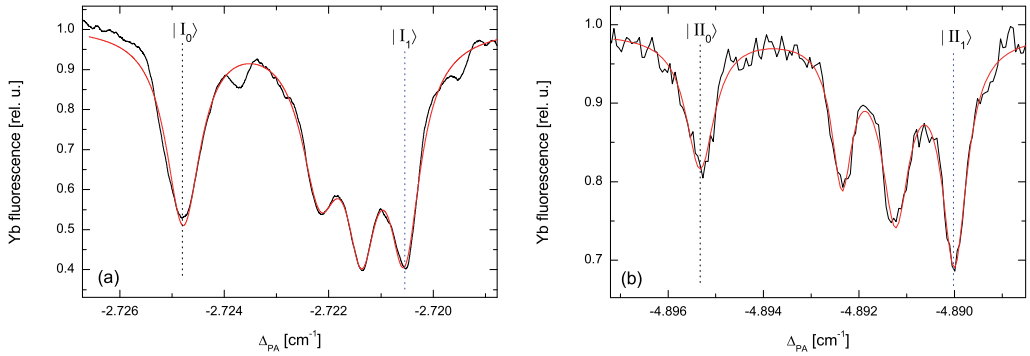

Figure 5.5.: *Used 1-Photon-Photoassociation resonances in* $^{176}Yb^{87}Rb$*, (a)* $\Delta v' = -9$*, (b)* $\Delta v' = -11$*. The used transitions for the rotational level* $R' = 0$ *(black) and* $R' = 1$ *(blue) are marked with the dotted lines.*

of the two lasers:

$$\Delta_{2\text{photon}} = \nu_1 - \nu_2 \tag{5.17}$$

with ν_1 and ν_2 are the absolute wavenumbers of the two lasers. With this definition, $\Delta_{2\text{photon}}$ corresponds to the binding energy of the vibrational states, if they belong to the $F = 1$ hyperfine ground state.

If $\Delta_{2\text{photon}}$ is smaller than $0.07\,\text{cm}^{-1}(= 2\,\text{GHz})$, we are able to use the beatnote of the two lasers to determine the difference of the two frequencies, recorded with a photodiode connected to a spectrum analyzer which gives us directly the frequency difference of the two lasers equivalent to $\Delta_{2\text{photon}}$.

For the 2-Photon-PA spectroscopy in ^{176}Yb, we focus on two resonances, namely the $\Delta v' = -9$ at $\Delta_{\text{PA}} = -2.723\,\text{cm}^{-1}$ and the $\Delta v' = -11$ at $\Delta_{\text{PA}} = -4.897\,\text{cm}^{-1}$, each with the two rotational states $R' = 0$ and $R' = 1$ and a subrotational splitting $\Delta_{R'}$ of the $R' = 1$ state. The corresponding 1-Photon-PA resonances are shown in fig. 5.5. From now on, the used excited states will be named as follows:

- The $|\Delta v' = -9, F' = 2\rangle$ state will be named as $|I_0\rangle$ for the $R' = 0$ component and $|I_1\rangle$ for the $R' = 1, \Delta_R = +1$ component.
- The $|\Delta v' = -11, F' = 2\rangle$ state will be named as $|II_0\rangle$ respective $|II_1\rangle$.

A typical scan is shown in fig. 5.6. This spectrum was recorded with the first laser fixed to the $|I_1\rangle$ resonance of the excited molecule.

For the determination of the ground state potential, we performed 2-Photon-PA measurements with the excited states $|I_0\rangle$ and $|II_0\rangle$. All resonances found are shown in fig. 5.7 for $|I_0\rangle$ (black curve) and $|II_0\rangle$ (red curve). For the identified ground state vibrational levels, the value for $\Delta_{2\text{photon}}$ is the same within the accuracy of our wavelength determination. Thus, the states can be considered to belong to the ground state. It should

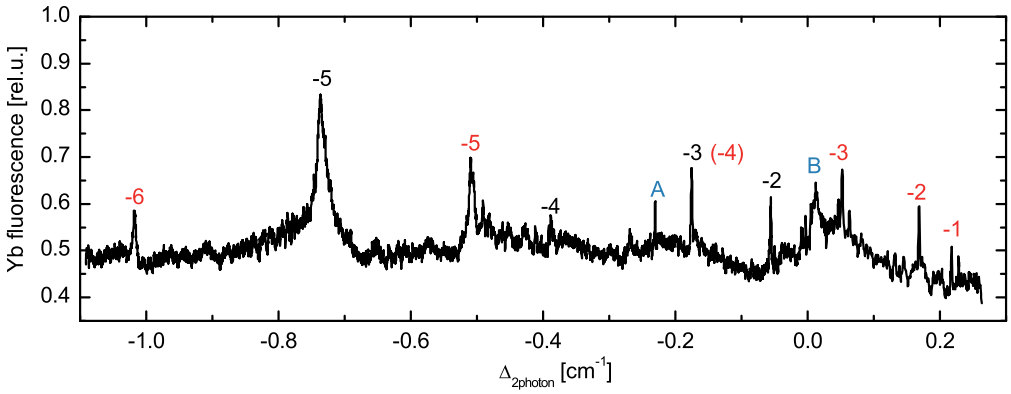

Figure 5.6.: *Spectra of 2-Photon-Photoassociation with the PA laser fixed to the $|I_1\rangle$ 1-Photon-PA resonance (see fig. 5.5 and chap. 4). The identified resonances are labeled by their relative quantum number Δv of the molecular ground state with $F = 1$ (black) or $F = 2$ (red) hyperfine ground state. The lines labeled with blue letters correspond to an 1-Photon-Photoassocation resonance in Rb (A), leading to less loss in Yb and to an artifact due to four-wave mixing of the tapered amplifier (B). For a determination of the vibrational quantum numbers see chapter 5.5. From [100]*

be emphasized, that resonances exist on the red side of the $F = 1$ hyperfine state with $\Delta_{2\text{photon}} > 0$. These states clearly belong to the $F = 2$ hyperfine level of the electronic ground state. The intensity of the peaks differs between the two excited states, but since this depends on the overlap of the ground and excited state wavefunction, this is expected.

5.4. Line Shapes

The model for the 1-Photon-Photoassociation, as described in chapter 4.2, was expanded to 2-Photon-Photoassociation in [101]. As explained in eqn. (4.2), the scattering probability for 1-Photon-PA is

$$|S_{\text{p}}(\epsilon, l, \Delta_1, I_1)|^2 = \frac{\gamma_p \gamma_s(\epsilon, l, I_1)/(2\pi)^2}{(\epsilon/\hbar - \Delta_1)^2 + (\gamma/4\pi)^2}$$

with $\gamma = \gamma_s + \gamma_p$. The stimulated width γ_s depends on the laser intensity I_1 and the Franck-Condon factor for the free-bound transition (see chapter 4.2). In the following, this is considered independent of the intensity I_2 of the second laser. It is also assumed that γ_s is constant for a given excited vibrational level and thus independent of the probed ground state. The natural linewidth γ_p of the excited state is independent of any laser intensities. The values for γ_s and γ_p are determined from 1-Photon-Photoassociation spectra. For consistent results, these values were calibrated once a day.

The single photon molecular production rate $|S_{1\text{g}}|^2$ in the 2-Photon case depends on the PA laser as the laser who creates the molecules and on the probe laser which disturbs this

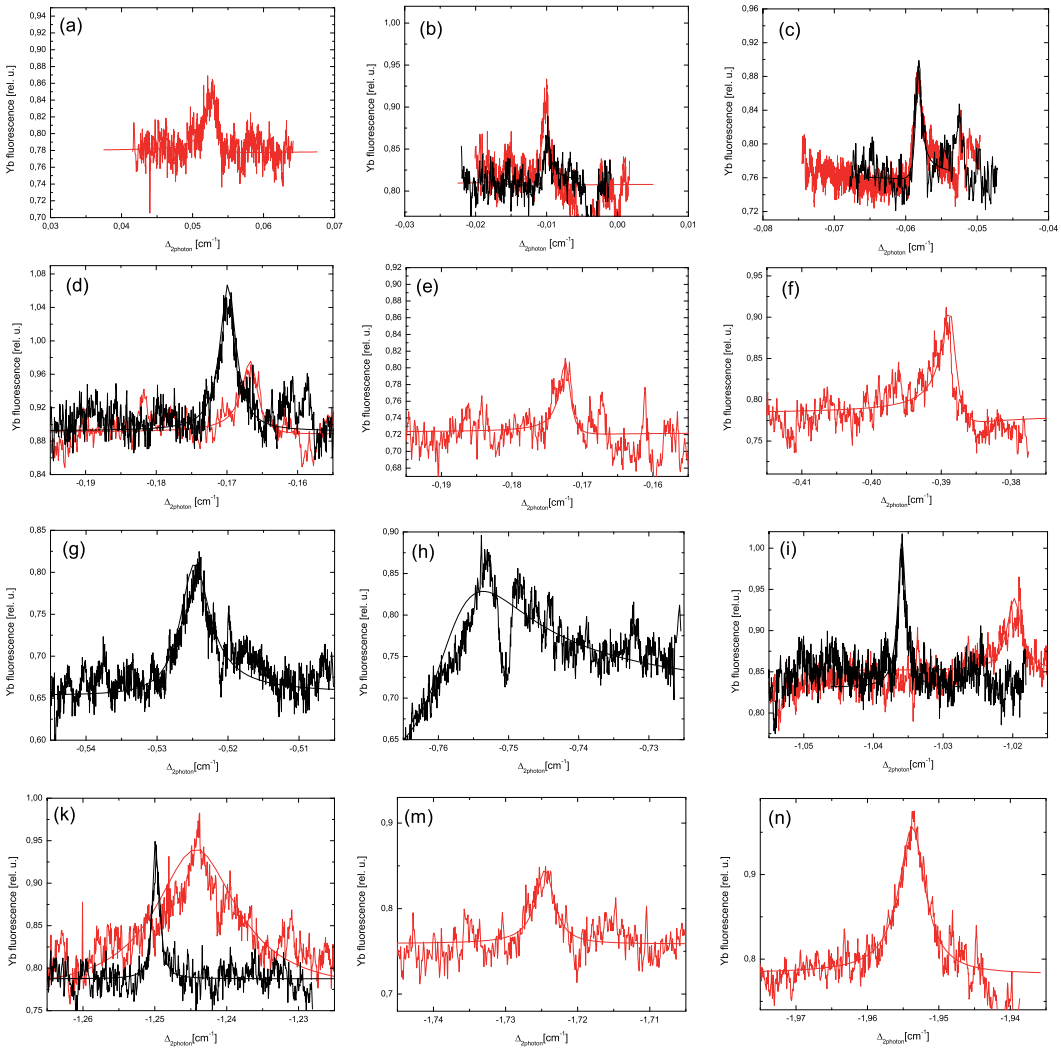

Figure 5.7.: *All observed resonances of the 2-Photon-PA spectroscopy using the two 1-Photon-PA resonances $|I_0\rangle$ (black) and $|II_0\rangle$ (red). Differences of the resonance positions can be attributed to the uncertainty of about $\pm 5 \cdot 10^3\,\mathrm{cm}^{-1}$ of the wavelength determination. Notes: (h) A "dip" can be seen in the resonance that only occurs at high intensities of the probe laser, it is also visible in (g) and the red curve in (k), we did not examine this effect in detail. In (i), the difference of the position of the two peaks is most likely due to the inaccuracy of the wavemeter.*

production and is calculated to be [101]

$$|S_{1g}|^2 = \frac{(\epsilon/\hbar - \Delta_2)^2 \gamma_p \gamma_s/(2\pi)^2}{((\epsilon/\hbar - \Delta_+)(\epsilon/\hbar - \Delta_-))^2 + (\gamma/4\pi)^2 (\epsilon/\hbar - \Delta_2)^2}. \tag{5.18}$$

Here, γ, γ_s and γ_p are defined the same way as for the 1-Photon-PA. Δ_2 is the detuning of the second laser from the bound state (see fig. 5.4). This laser splits a single vibrational

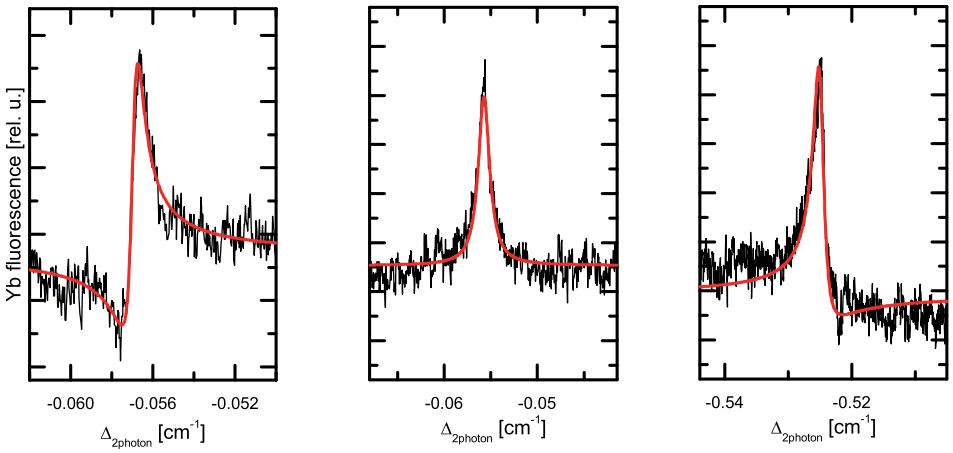

Figure 5.8.: *Examples of observed lineshapes for the 2-Photon Photoassociation resonance. Left:* $\Delta_1 > 0$ MHz, *middle:* $\Delta_1 \approx 0$ MHz, *right:* $\Delta_1 < 0$ MHz.

level of the excited state into a pair with the energies of

$$\Delta_\pm = \frac{1}{2}\left(\Delta_1 + \Delta_2\right) \pm \frac{1}{2}\sqrt{\left(\Delta_1 - \Delta_2\right)^2 + \left(\frac{\Omega}{2\pi}\right)^2}. \tag{5.19}$$

The splitting of the two resonances is then:

$$\Delta = \Delta_+ - \Delta_- = \sqrt{\left(\Delta_1 - \Delta_2\right)^2 + \left(\frac{\Omega}{2\pi}\right)^2} \tag{5.20}$$

This definition corresponds to eqn. (5.16), if a detuning from the resonance is defined as $\delta = \Delta_1 - \Delta_2$. Note that in this definition, Ω is the splitting of the pair and therefore differs from the definition of Bohn and Julienne [101]. This splitting is called Autler-Townes-Splitting [96] and the Rabi frequency Ω is defined as

$$\Omega = \left|\langle a|b\rangle\right| \gamma_p \sqrt{\frac{I_2}{4I_{\mathrm{sat}}}} \tag{5.21}$$

where I_{sat} is the saturation intensity and γ_p is the atomic linewidth as before. The overlap integral is related to the Franck-Condon factor f_{FC} through $f_{\mathrm{FC}} = |\langle a|b\rangle|^2$. The Autler-Townes splitting will be discussed in detail in the next chapter.

Fig. 5.8 is showing some examples with different values for Δ_1, showing that the model is well reproducing our data.

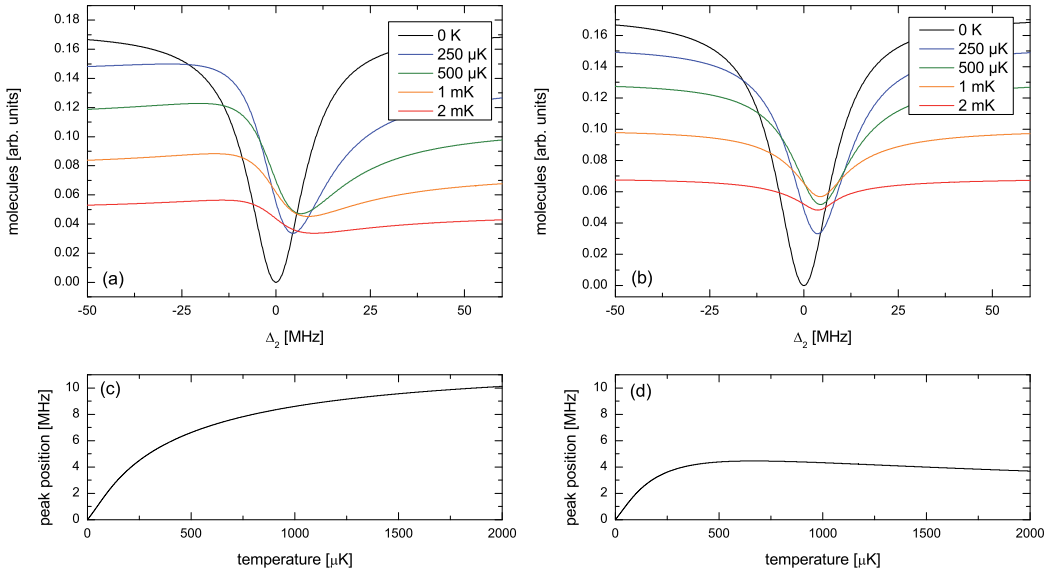

Figure 5.9.: *Temperature dependence of 2-Photon-PA. (a) Resonance at different temperatures with* $\Delta_1 = 0$*. (b) Resonance at different temperatures with* Δ_1 *equals the maximal depth of the 1-Photon-PA (see chapter 4.2). Down: Relative position of the peak position (compared to the case at* $T = 0\,\mathrm{K}$*) with (c)* $\Delta_1 = 0$ *respective (d)* Δ_1 *equals the maximal depth of the 1-Photon-PA resonance.*

The atoms are trapped in a MOT at a temperature of about $250\,\mu$K. Thermal averaging over the collision energy ϵ is necessary for this temperature. This is given by [102]

$$K = \frac{1}{hQ_T} \int |S_{1\mathrm{g}}|^2 \, e^{-\epsilon/k_\mathrm{B}T} d\epsilon \tag{5.22}$$

where $Q_T = (\frac{2\pi k_\mathrm{B} T \mu}{h^2})^{3/2}$ is the partition function with μ being the reduced mass. Some examples for different temperatures are shown in fig. 5.9 (a) with Δ_1 set to zero detuning and (b) with Δ_1 set to the maximal depth of the 1-Photon-PA resonance at a given temperature (see chapter 4.2). In (c) and (d), the shift of the resonance against the temperature is shown. For a temperature of $250\,\mu$K, the thermal shift is about 4 MHz and is thus small compared to the uncertainty of the wavemeter, which is about 120 MHz and can be neglected. For the resonances found in the region below 2 GHz, we used the beat-signal of the two lasers and the accuracy of this method is about $\pm 6\,$MHz, therefore the temperature shift should be considered.

Since the shift of the temperature is small, the simpler equation (5.18) without considering the temperature is used as a fitting function for the resonances. This function has the detuning Δ_1 and Δ_2 of the two lasers from the transition and the Rabi frequency Ω as fitting parameters, some examples are shown in fig. 5.8.

5.5. Line assignment

Let us first concentrate on the resonances found with the PA laser being on the $R' = 0$ component in the excited state. Each resonance we found can be assigned to one vibrational state in the ground state. No substructure was found. Hence, there must be a selection rule giving only one possible transition to the ground state. Since both states are following Hund's case (e) coupling, both vibrational states are loosely bound and therefore the coupling between the nuclear motion and the electronic momentum of the electron is weak. Therefore, the nuclear motion cannot be changed by the absorption of a photon. The comparison between the structure of the resonances found when the PA laser is on a $R' = 0$ component and resonances found when the PA laser is on a $R' = 1$ component confirm this assumption (see next section).

It is also interesting to notice, that the hyperfine splitting of the Rb ground state is also seen in the resonances found in the 2-Photon-PA. To most of the vibrational levels, there is a corresponding resonance about $0.227\,\mathrm{cm}^{-1}$ apart. This is exactly the hyperfine splitting of the ground state of the ^{87}Rb atom. These states will be labeled with $F = 1$ and $F = 2$ from now on. There were also resonances found on the red side ($\Delta_{2\mathrm{photon}} > 0$) of the $F' = 2 \rightarrow F = 1$ transition, which clearly indicates, that these bound molecular levels must correspond to the $F = 2$ hyperfine ground state of Rb. A typical spectrum is shown in fig. 5.6. We performed a whole scan with the PA laser fixed to the $|I_1\rangle$ excited level from $+0.3\,\mathrm{cm}^{-1}$ to $-1.1\,\mathrm{cm}^{-1}$ and found 10 resonances, from which we assigned 5 to the upper hyperfine state of Rb ($F = 2$) and 5 to the lower $F = 1$ state[2]. All observed resonances that are used for the determination of the ground state potential in ^{176}Yb^{87}Rb are shown in fig. 5.7 with the intermediate excited states $|I_0\rangle$ and $|II_0\rangle$.

5.5.1. Vibrational levels

To assign a vibrational quantum number to a series, we used the same method as for the 1-Photon-PA: LeRoy and Bernstein found in 1970 [6] an equation for calculating the position of the vibrational states of one series (see chapter 2.2.3, especially eqn. (2.22)):

$$\Delta_{\mathrm{bind}} = -\frac{1}{hc}\left(\hbar\left(\frac{2\pi}{\mu}\right)^{\frac{1}{2}}\frac{\Gamma\left(1+\frac{1}{n}\right)}{\Gamma\left(\frac{1}{2}+\frac{1}{n}\right)}\frac{n}{C_n^{1/n}}\left(v_{\mathrm{D}}-\Delta v\right)\frac{n-2}{n}\right)^{\frac{2n}{n-2}}$$

Here, μ is the reduced mass, Γ the Gamma function, v_{D} is the non-integer value of the vibrational quantum number at the dissociation limit und C_n is the long-range coefficient of the potential and $n = 6$ for a heteronuclear diatomic molecule. This equation can also be used to assign vibrational quantum numbers to the observed ground state levels. The position of the vibrational series Δ_{bind} is corrected by the hyperfine splitting of the Rb atom for each resonance by

$$\Delta_{\mathrm{bind}}(\Delta v, F) = \Delta_{2\mathrm{photon}} + \Delta_{\mathrm{HFS}}(F). \tag{5.23}$$

[2] With the help of the assumed hyperfine splitting of the ground state, we were able to find another resonance at $\Delta_{2\mathrm{photon}} = -1.24\,\mathrm{cm}^{-1}$ which is not shown on the spectrum

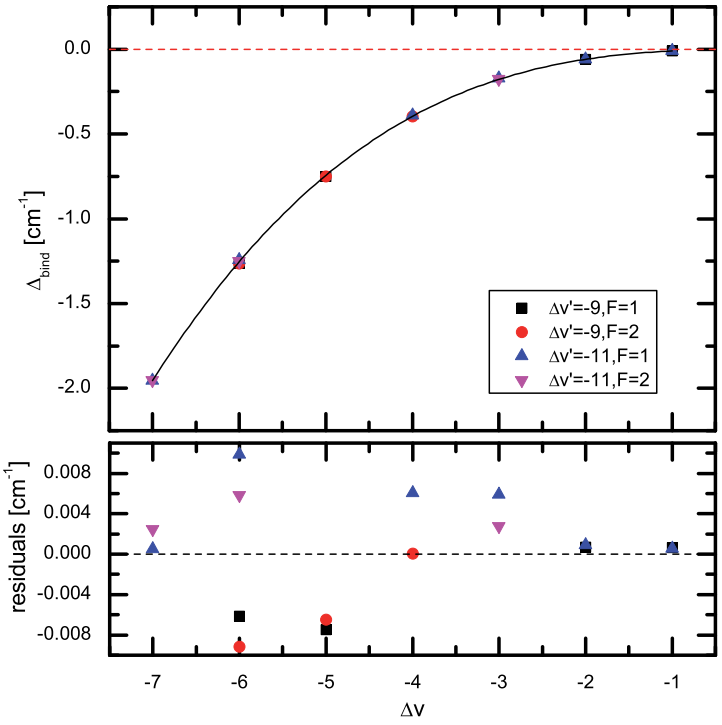

Figure 5.10.: *Fit to the vibrational level of the ground state molecule. In the upper graph, the broken red line indicates the dissociation energy. A fit to the data yields a value for* $C_6 = -(2563 \pm 50)\,\mathrm{E_h a_0^6}$.

Here, $\Delta_{2\mathrm{photon}}$ is the difference of the two lasers, giving the difference of the probed state to the $F = 1$ hyperfine ground state of Rb. $\Delta_{\mathrm{HFS}}(F = 1) = 0\,\mathrm{cm}^{-1}$ and $\Delta_{\mathrm{HFS}}(F = 2) = -0.227\,\mathrm{cm}^{-1}$ respects the hyperfine structure of Rb. A change of this value is not found in our data.

In a next step, we repeated the same measurements on the excited vibrational level $|II_0\rangle$ 1-Photon-resonance. Since the second laser still couples to the same ground state as before, this should give the same binding energies for the probed vibrational levels of the ground state. So, this state can also be used as a test for the assignment. In fig. 5.7, the resonances found in this scan are shown in the red curves. We confirmed most of the known resonances within the uncertainty in wavelength measurement except for two which we did not find in this level, but still fit into the potential. The magnitude of the resonances differs for the two excited states (see chapter 5.6 for details), but that is expected due to the different vibrational level with a different wavefunction leading to a different overlap integral. That is also the reason that we did not find two of the levels, it seems to be a very low overlap

R=0

Δv	F	rel. position ($\Delta v' = -9$) / cm^{-1}	rel. position ($\Delta v' = -11$) / cm^{-1}
-1	2	-[b]	-[b]
-1	1	-0.0098[c]	-0.0099[c]
-2	2	-[b]	-[b]
-2	1	-0.0588[c]	-0.0586[c]
-3	2	-[a]	-0.1751[c]
-3	1	-[a]	-0.172
-4	2	-0.396	-0.395
-4	1	-[a]	-0.390
-5	2	-0.751	-[a]
-5	1	-0.752	-[a]
-6	2	-1.263	-1.248
-6	1	-1.260	-1.244
-7	2	-[a]	-1.952
-7	1	-[a]	-1.954

R=1

Δv	F	rel. position ($\Delta v' = -9$) / cm^{-1}	rel. position ($\Delta v' = -11$) / cm^{-1}
-1	2	-0.012	-[a]
-1	1	-0.0094[c]	-0.0096[c]
-2	2	-0.057	-0.057
-2	1	-0.0565[c]	-0.0572[c]
-3	2	-0.172	-0.175
-3	1	-0.174	-0.177
-4	2	-0.399	-0.393
-4	1	-0.390	-0.393
-5	2	-0.736	-[a]
-5	1	-0.744	-[a]
-6	2	-1.249	-1.253
-6	1	-1.245	-1.255
-7	2	-[a]	-1.952
-7	1	-[a]	-1.957

[a] not observed [b] not measured

Table 5.1.: *Resonances found in 2-Photon-PA spectroscopy in $^{176}Yb^{87}Rb$. The measurement accuracy is $4 \cdot 10^{-3}\,\mathrm{cm}^{-1}$ if not labeled with [c] where the accuracy is $2 \cdot 10^{-4}\,\mathrm{cm}^{-1}$ (direct measurement using the beat frequency). Due to the lower 1-Photon-PA signal in the $R' = 0$ component, it is possible, that the resonances that we did not observe in this component are too small to distinguish them from the background signal.*

of the two wavefunctions.

To get more information about the rotational structure of the ground state, we repeated the measurement with the PA Laser fixed to the $R' = 1$ component where also one resonance per vibrational level was found, but slightly shifted with respect to the $R' = 0$ resonances. A discussion of the rotational splitting will follow in the next section.

Table 5.1 shows the found values for the two vibrational levels $\Delta v' = -9$ and $\Delta v' = -11$. They differ only within error bars so that it can be concluded that these resonances all connect to vibrational levels of the $^2\Sigma_{1/2}$ ground state of the ^{176}Yb^{87}Rb molecule.

With the help of the LeRoy-Bernstein formula (2.22), it is possible to determine a C_6 value for this potential. A fit to our data with the PA laser fixed to the $R' = 0$ component is shown in fig. 5.10 and gives us the following values:

$$\begin{aligned} C_6 &= -(2563 \pm 50)\,\mathrm{E_h a_0^6} \\ v_\mathrm{D} &= 0.26 \pm 0.02 \end{aligned} \tag{5.24}$$

With the help of these values, it would be theoretically possible to calculate the last bound state of the potential which determines the s-wave scattering length. But it has been shown [103] that the approximations that have been made for the derivation of the LeRoy-Bernstein equation (2.22) should be modified near the dissociation limit. This is important for states which are less bound than $0.33\,\mathrm{cm}^{-1}$(=10 GHz) [83]. In other words, v_D should be regarded as a fit parameter with limited physical significance rather than a real non-integer value of the vibrational quantum number. Therefore, this equation fails for determining the last bound state and thus, for determining the s-wave scattering length. A fully numerical solution is favorable (see chapter 5.8).

5.5.2. Rotational levels

The rotational energy of a state is defined as (see also chapter 4.3.2)

$$E_\mathrm{rot} = B_\mathrm{rot} R \cdot (R+1) \tag{5.25}$$

with the rotational constant $B_\mathrm{rot} = \hbar^2/(2\mu r^2)$. Therefore, the difference of the $R = 0$ and the $R = 1$ component is giving us twice the rotational constant. An estimated size of the ground state molecules of about $r \approx 25 a_0$ implies rotational constants in the region of $B_\mathrm{rot} \approx 1.6 \cdot 10^{-3}\,\mathrm{cm}^{-1}$.

We already discussed that the 2-Photon-Photoassociation process does only couple to states with the same rotational quantum number:

$$\Delta R = R' - R = 0 \tag{5.26}$$

Here, R' belongs to the excited state and R to the ground state. To get information about the rotational structure of the ground state, it is essential to repeat the measurements with the PA Laser locked to different components of an excited vibrational level. The experimental data lead to the following findings: The three substates of the excited $R' = 1$ component couple to the same level in the ground state. The $R' = 0$ component couples to

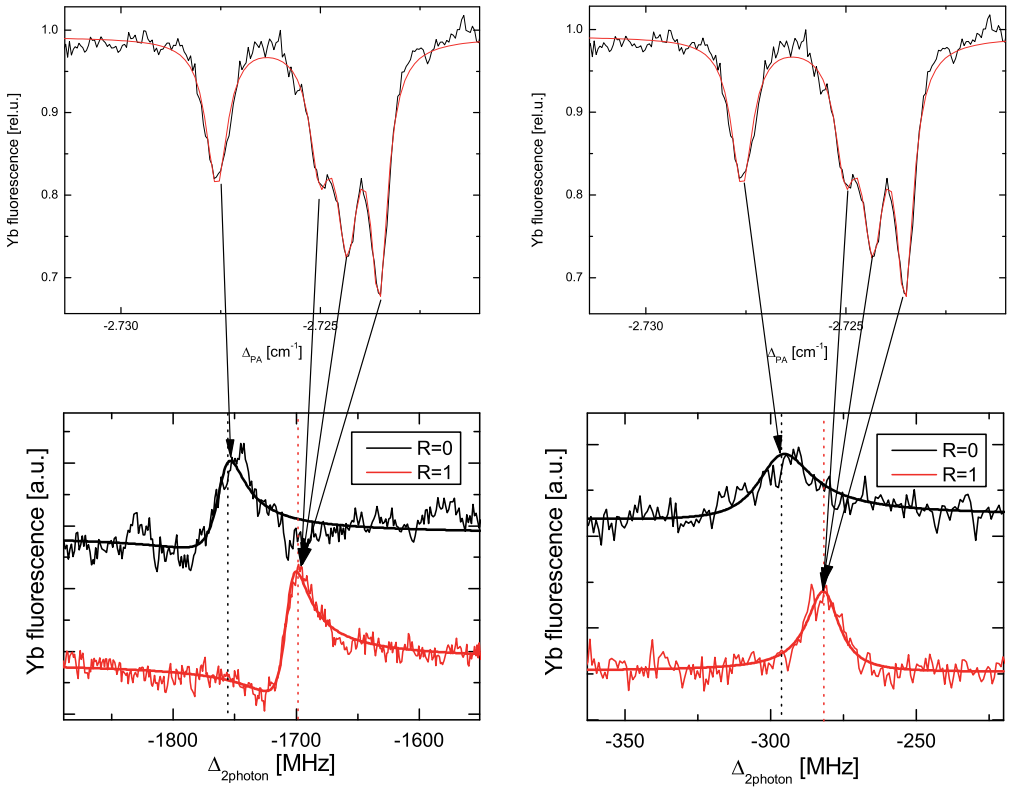

Figure 5.11.: *The position of the resonance is dependent of the rotation of the first transition. Upper Graph: the used 1-Photon-PA resonance for the 2-Photon resonances. The arrows indicate which resonance belongs to which excited state. It shows that the $R' = 0$ component is shifted against the components that come from one of the subrotational states of the $R' = 1$ component. Lower Graphs: The black curve shows the PA laser fixed to the $|I_0\rangle$ 1-Photon-PA resonance. Red: The PA Laser fixed to one of the $R' = 1$ components of the $|I\rangle$ 1-Photon-PA resonance. All three substates lead to the same 2-Photon-PA resonance. The difference between these two resonances is $2 \cdot B_{\mathrm{rot}}$, since the rotational energy is defined es $E_{\mathrm{rot}} = B_{\mathrm{rot}} \cdot R \cdot (R+1)$. The data is vertically shifted.*

a different state that is more bound. This shows, that states coupled to the $R' = 0$ have less rotational energy than the states coupled to $R' = 1$ states. This confirms the assumption we made in eqn. (5.26). In addition, there is no splitting into subrotational levels in the $R = 1$ component of the ground state. In fig. 5.11, this is shown. We locked the PA laser to different components of one vibrational level in the excited state and scanned the probe laser over the resonances $\Delta v = -1$ and $\Delta v = -2$ where the beat frequency of the two lasers can be used to determine $\Delta_{2\mathrm{photon}}$. The accuracy of $\pm 2 \cdot 10^{-4}\,\mathrm{cm}^{-1}$ of this method makes it possible to determine the rotational constant. The black arrows indicate which resonance in the ground state was found.

We compared the measurements of the $R' = 0$ and the $R' = 1$ rotational component of

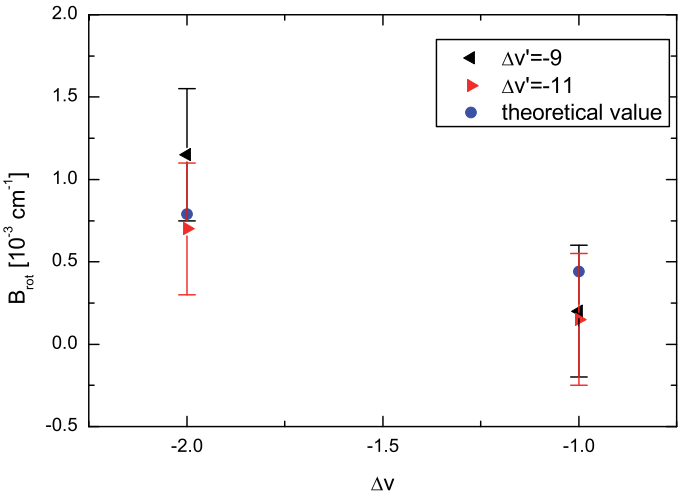

Figure 5.12.: *The rotational constant B_{rot} for the $\Delta v = -1$ and $\Delta v = -2$ vibrational levels of the ground state in $^{176}Yb^{87}Rb$. The theoretical value is given by equation (5.27) with the values from (5.24).*

the excited state for the two vibrational levels $\Delta v' = -9$ and $\Delta v' = -11$. In fig. 5.12, these resonances were shown together with a theoretical value obtained from the equation by LeRoy [104] for the rotational constant:

$$B_{rot} = \frac{\hbar}{4\pi c\mu} \cdot \frac{\Gamma(1+1/n)\Gamma(1/2-1/n)}{\Gamma(1/2+1/n)\Gamma(1-1/n)} \cdot \left(\frac{E_D - E(v)}{C_n}\right)^{2/n} \tag{5.27}$$

This method has the same limitations than the LeRoy-Bernstein formula for calculating the vibrational levels, but is still well within the error bars of our experimental data.

For more bound vibrational levels the beat signal cannot be used anymore and we had to use our wavemeter for wavelength measurement. Since the accuracy of this method is only $\pm 5 \cdot 10^{-3}\,\mathrm{cm}^{-1}$, it was not possible to determine the rotational constant as it is expected to be smaller than our accuracy.

5.6. Linewidth

5.6.1. Intensity dependence

In the 2-Photon-PA spectroscopy, the width of a resonance gives information about the strength of the transition. The key factor is the Rabi frequency

$$\Omega_0 = \frac{\langle a|\vec{d}\cdot\vec{\epsilon}E_0|b\rangle}{\hbar} = |\langle a|b\rangle|\,\gamma_1\sqrt{\frac{I}{4I_{\mathrm{sat}}}} \tag{5.28}$$

which shows the squareroot-dependence on the intensity of the laser field driving the transition. In order to determine the intensity dependence experimentally, we fixed the PA laser to the resonance at the excited vibrational level $|I_0\rangle$ and varied the intensity of the probe

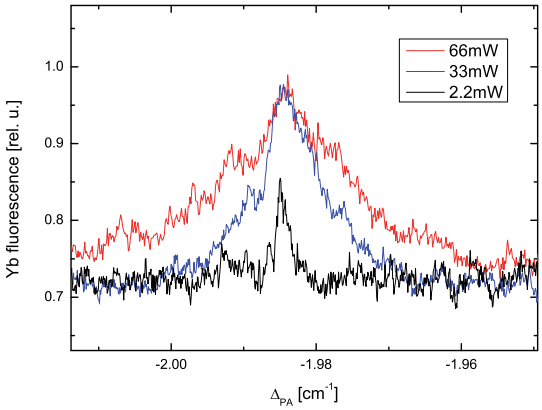

Figure 5.13.: *The 2-Photon-PA resonance* $|I_0\rangle \leftrightarrow |\Delta v = -5, F = 1\rangle$ *observed with different power levels in the probe laser. It is clearly visible that the resonance gets broader with higher intensities. Eventual shifts of the peak positions are corrected to be at the same position.*

laser which couples the ground state level $\Delta v = -5, F = 1$ to this excited state. We chose this level because it is the broadest resonance found. Fig. 5.13 shows this resonance with different intensities. It is obvious that this transition gets broader with higher intensities.

The 2-Photon-PA line shape equation is given by eqn. (5.18). If we now fit our data to this equation, we get the Rabi frequency Ω directly as a parameter. The values for γ_s and γ_p are determined by the data taken in 1-Photon-PA experiments. It is essential for the fitting routine, that these values are kept constant, otherwise the determination of Ω fails. For very little intensities of the laser, this method gives too big values since the temperature of the atom cloud is not included which broadens the resonance. But still, the dependence of the intensity can be reproduced. Fig. 5.14 plots the squareroot of the laser power against the Rabi frequency, giving a linear dependence of these two.

With a fit to this data, it is possible to calculate the overlap integral of the ground and excited state:

$$|\langle a|b\rangle| = \frac{\Omega}{\gamma_1}\sqrt{\frac{4I_{\mathrm{sat}}}{I}} \tag{5.29}$$

With the saturation intensity $I_{\mathrm{sat}} = 1.496\,\mathrm{mW/cm^2}$ and the atomic linewidth $\gamma_1 = 2\pi 5.75\,\mathrm{MHz}$, one gets for the Franck-Condon factor:

$$f_{\mathrm{FC}} = |\langle a|b\rangle|^2 = 0.25 \pm 0.04 \tag{5.30}$$

The given error bars are resulting from the statistical error from the fitting function. The real error is higher because the determination of the beam size and the overlap of the PA and probe beam is not perfect and thus, the determined intensity has an error, too. Furthermore, the determination of the Rabi frequency depends on the width of the

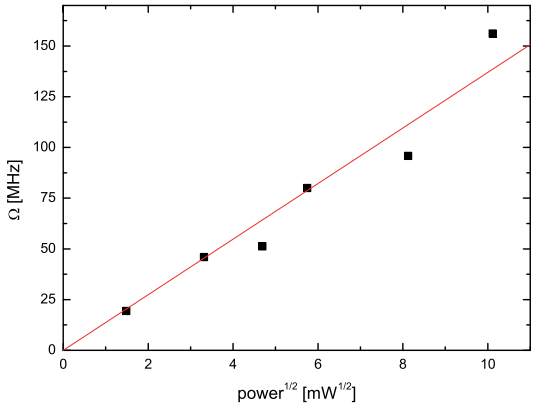

Figure 5.14.: *Intensity dependence of the Rabi frequency at the transition $|I_0\rangle$ to $|\Delta v = -5, F = 1\rangle$. The Rabi frequency should be proportional to the squareroot of the intensity. The red line is a fit.*

measured resonance which is also temperature dependent and may be broadened by the PA and probe laser linewidth. This is not included in this calculation. On the plus side, it should be noted that the determination of transition strengths is independent of the atomic density.

5.6.2. Transition strengths

This method is transferrable to all other found resonances as well. In principle, only one intensity is needed to get all Rabi frequencies of the transitions and get all the transition strengths. The above section showed that this method actually is working and giving reasonable results. Fig. 5.15 shows the calculated Franck-Condon factors for each found resonance. The above described method can in principle be used for any resonance, but the width of a resonance is not only dependent on the Rabi frequency but also on the temperature and the stimulated width. This leads to more inaccuracies. In the Autler-Townes spectroscopy, the Rabi frequency can be measured directly, therefore this method is the better choice. This will be discussed in chap. 6.

5.7. Binding energies of RbYb isotopologues

The binding energy of the least bound states can be used to determine the s-wave scattering length and thus intercollisional properties. For a precise determination of these energies, we performed 2-Photon-PA spectroscopy measurements on 4 different isotope combinations. The PA laser was fixed to a known 1-Photon-PA resonance (see chapter 4.4) and the probe laser was scanned in the range up to 2 GHz. In this way, it was possible to use the beat frequency of the two lasers to determine binding energies in a more accurate

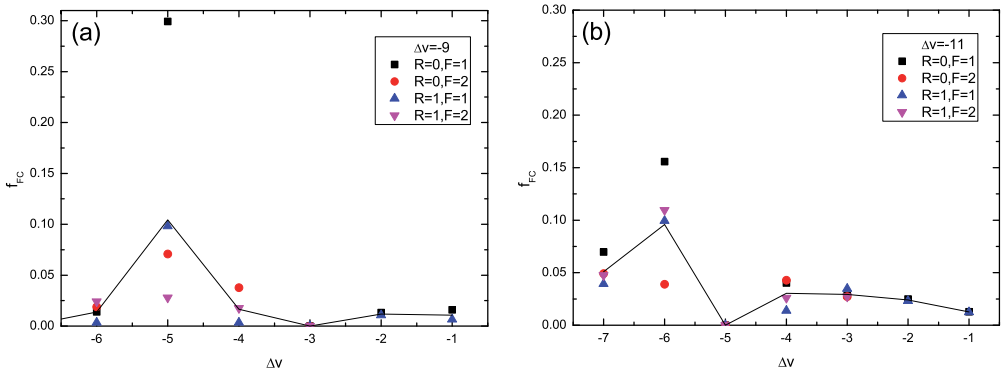

Figure 5.15.: *Calculated Franck-Condon factors from experimentally determined Rabi frequencies for the different resonances. Note that no resonances for (b) $\Delta v = -5$ were found indicating a very low Franck-Condon overlap. The line is a guideline for the eyes, containing the average of all 4 possibilities for each resonance. (a) $\Delta v' = -9$, (b) $\Delta v' = -11$.*

Δv	Yb isotope	Δ_{bind} $(R = 0)$	Δ_{bind} $(R = 1)$
0	^{170}Yb	-115 MHz	-98 MHz
	^{172}Yb	-164 MHz	-144 MHz
-1	^{170}Yb	-1030 MHz	-982 MHz
	^{172}Yb	-1240 MHz	-1213 MHz
	^{174}Yb	-231 MHz	-204 MHz
	^{176}Yb	-294 MHz	-282 MHz
-2	^{174}Yb	-1479 MHz	-1438 MHz
	^{176}Yb	-1763 MHz	-1694 MHz

Table 5.2.: *Binding energies for the different Yb isotopes for the vibrational level $\Delta v = -1$ and $\Delta v = -2$. The accuracy of the energies is ± 10 MHz. The shift due to the temperature of the MOTs of 250 μK is not included (see chapter 5.4 for details).*

way as with the wavemeter. This is the same approach as we used for ^{176}Yb^{87}Rb. The observed resonances for the 4 different Yb isotopes are shown in fig. 5.16. The left graph shows the used 1-Photon-PA resonance while the other two graphs show the position of the $R = 0$ (green) respectively $R = 1$ (red) resonance of all levels found in the range up to 2 GHz. Table 5.2 lists all observed resonances together with the relative vibrational level, determined by numerical calculations. The LeRoy-Bernstein formula (2.22) is used to determine v_D for each isotopologue. The parameter v_D is listed in tab. 5.3, although it is only used as a fitting parameter because of the limitations of this formula. The two resonances of each combination are used which fit well in a potential with the C_6 value determined for ^{176}Yb^{87}Rb. This was done for all three isotopologues individually leading

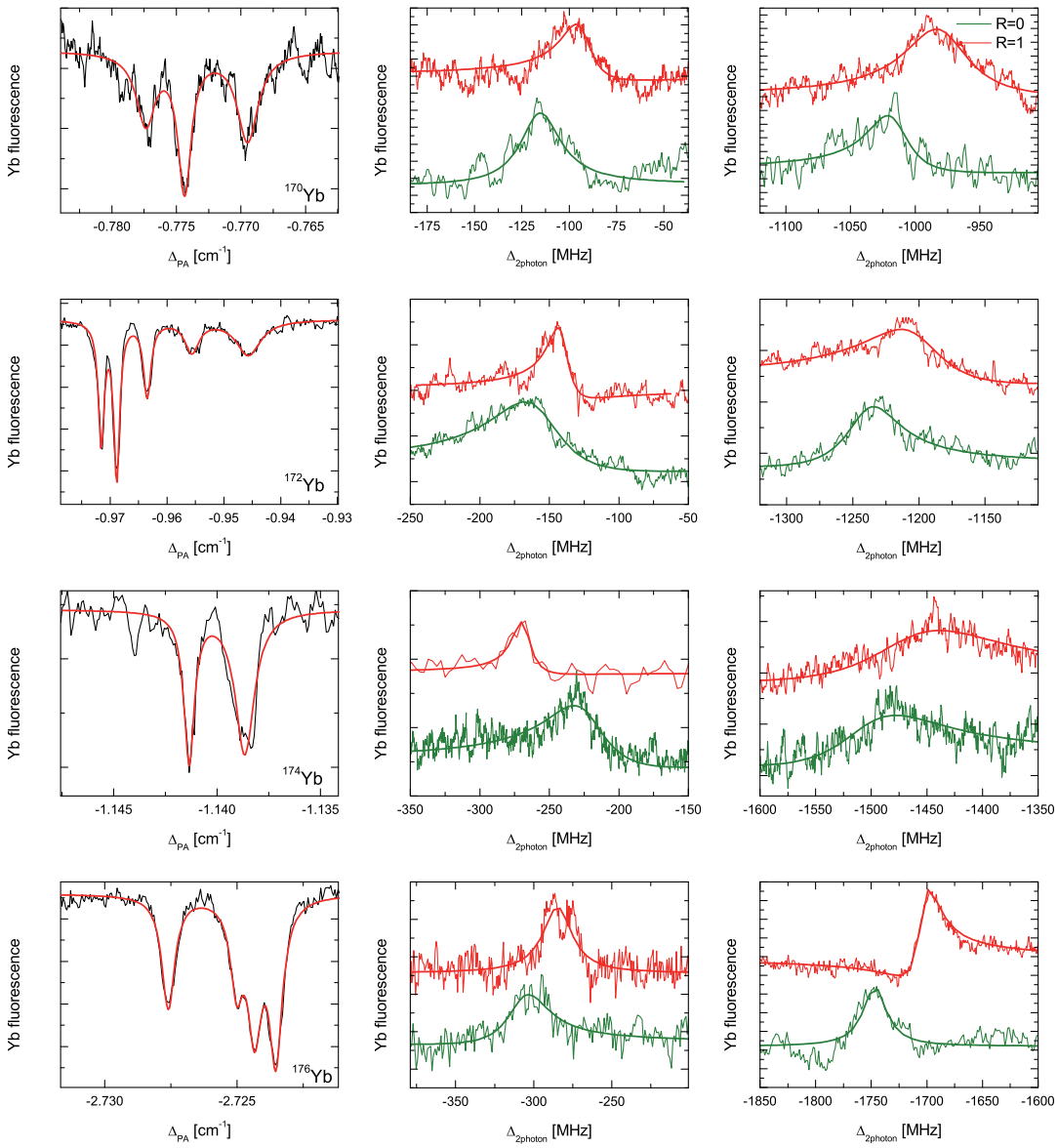

Figure 5.16.: *Left: 1-Photon-PA resonances in the different Yb isotopes used for the 2-Photon-PA.* ^{176}*Yb was added for completeness. Middle and Right: Measured vibrational levels in different Yb isotopes. The green curves represent* $R = 0$ *resonances, red curves represent* $R = 1$ *resonances.*

to the potential shown in fig. 5.17. Numerical calculations (see chap. 5.8) show that for the isotopes ^{174}Yb and ^{176}Yb, one more vibrational level near the dissociation limit exist. Unfortunately, we are not able to measure these resonances directly because they are too close to the 1-Photon-PA resonances causing additional losses in the signal.

Yb isotope	v_D
^{170}Yb	0.88
^{172}Yb	0.00
^{174}Yb	0.13
^{176}Yb	0.26

Table 5.3.: *The fitting parameter v_D for the LeRoy-Bernstein formula. This value does not offer any physical meaning because of the limitations of this formula. A numerical solution is favorable (see chap. 5.8).*

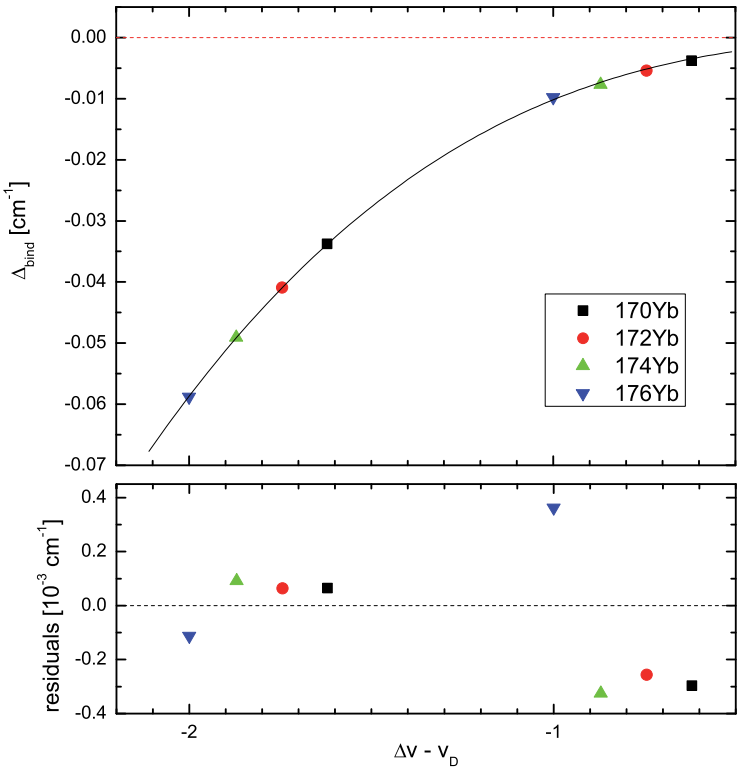

Figure 5.17.: *Fit to the binding energies of the different isotopes with $R = 0$. The binding energies were corrected by the atomic mass. The only fitting parameter is v_D.*

5.8. s-wave scattering length

The properties of a collision of particles with low energies are determined by the s-wave scattering and can be expressed by the scattering length a. For distinguishable particles a is related to the scattering cross section by

$$\sigma = 4\pi a^2. \tag{5.31}$$

This equation is valid for temperatures below the centrifugal barrier for the $R = 1$ component (see chapter 2.2.5) which is about 70 μK for RbYb. The value of the scattering length is determined by the potential energy $V(r)$ of the interatomic interaction. For large distances, this potential has been measured for the combination Rb and Yb:

$$V(r) = \frac{C_6}{r^6} \tag{5.32}$$

with a value of $C_6 = -2563 \pm 50\,\mathrm{E_h a_0^6}$. It defines a characteristic length

$$a_c = \left(\frac{-2\mu C_6}{\hbar^2}\right)^{1/4} \tag{5.33}$$

which is about $153a_0$ for the combination ^{176}Yb^{87}Rb. At this point, the kinetic energy of the relative motion equals their interaction energy [103].

Gribakin and Flambaum [103] described a semiclassical approximation for computing the s-wave scattering length a from a potential $V(r)$ where the scattering length is given by

$$a = \bar{a}\,(1 - \tan(\phi - \pi/8)) \tag{5.34}$$

with the mean scattering length

$$\bar{a} = 2^{-3/2}\frac{\Gamma\left(\frac{3}{4}\right)}{\Gamma\left(\frac{5}{4}\right)}a_c = 0.478a_c \tag{5.35}$$

and the phase

$$\phi = \frac{\sqrt{2\mu}}{\hbar}\int_{R_0}^{\infty}\sqrt{|V(r)|}dr. \tag{5.36}$$

The number of bound states can then be calculated by

$$N = [\phi/\pi + 3/8] \tag{5.37}$$

where the squared brackets mean taking the integer part. The scattering length can be calculated by using the quantum-defect formulation of Gao [105, 106]. A Lennard-Jones potential

$$V(r) = C_{12}/r^{12} + C_6/r^6 \tag{5.38}$$

is used with C_{12} serving as a "quantum defect" parameter. With this type of potential, the phase is determined as

$$\phi = \frac{\sqrt{\pi}}{12}\frac{\Gamma(1/3)}{\Gamma(11/6)}\sqrt{\frac{2\mu}{\hbar^2}}\left(\frac{(-C_6)^5}{C_{12}^2}\right)^{1/6}. \tag{5.39}$$

In the next step, the Schrödinger equation

$$\left(-\frac{\hbar^2}{2m}\Delta + V(r)\right)\Psi = E\Psi \tag{5.40}$$

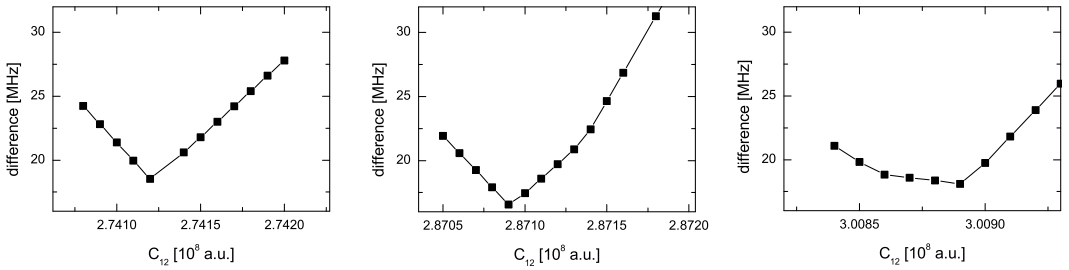

Figure 5.18.: *Determination of the C_{12} value. Shown is the sum of the absolute differences to the experimental determined states for the $\Delta v = -1$ state of ^{170}Yb, ^{174}Yb and ^{176}Yb. The C_{12} value determines the number of vibrational states in the ground state, left: 66 vibrational states, middle: 65 vibrational states, right: 64 vibrational states, in each case for $^{176}Yb^{87}Rb$. The best result for the potential is yielding 66 vibrational states for $^{176}Yb^{87}Rb$ (see text).*

is numerically solved with the potential (5.38). The solution of the Schrödinger equation was introduced by Liu [107]. A Mathematica-Script written by D. Farkas [108] was used here to solve the equation.

To simplify the numeric calculations, we have used the C_6 coefficient as determined by the LeRoy Bernstein method to $C_6 = -2563\,\mathrm{E_h a_0^6}$. The C_{12} coefficient was varied and the three eigenstates $\Delta v = -1$ for the isotopologues with ^{170}Yb, ^{174}Yb and ^{176}Yb were calculated. The absolute difference of these three calculated states to the experimentally determined values is shown in fig. 5.18. With the best value for the C_{12} coefficient obtained using this method, all known states of the isotopologue ^{176}Yb^{87}Rb have been calculated and the difference has been compared. For

$$C_{12} = 2.7412 \cdot 10^8\,\mathrm{E_h a_0^{12}} \tag{5.41}$$

all known resonances are calculated within the experimental error bars. A comparison between the experimental values and the theoretical calculations is shown in tab. 5.4. With this value, the ground state has 66 vibrational levels for ^{174}Yb^{87}Rb and ^{176}Yb^{87}Rb. The other, lighter isotopes have 65 vibrational levels. The s-wave scattering lengths for the different Yb isotopes can be determined to according to eqn. (5.34) to:

$$\begin{aligned} a_{^{87}\mathrm{Rb},^{170}\mathrm{Yb}} &= -5a_0 \\ a_{^{87}\mathrm{Rb},^{172}\mathrm{Yb}} &= -131a_0 \\ a_{^{87}\mathrm{Rb},^{174}\mathrm{Yb}} &= 1398a_0 \\ a_{^{87}\mathrm{Rb},^{176}\mathrm{Yb}} &= 225a_0 \end{aligned} \tag{5.42}$$

These results approve our previous studies [4, 7], where we performed thermalization measurements in a thermal mixture of ^{87}Rb and various Yb isotopes in the temperature regime of about 10 μK, well below the centrifugal barrier for p-wave collisions.

$\mathbf{C_6 = -2563\,E_h a_0^6,\ C_{12} = 2.7412 \cdot 10^8\,E_h a_0^{12}}$

Yb isotope	Δv	exp. value	theor. value	difference
176	-1	-298 MHz	-305 MHz	7 MHz
176	-2	-1767 MHz	-1770 MHz	3 MHz
174	-1	-235 MHz	-223 MHz	-12 MHz
174	-2	-1483 MHz	-1501 MHz	18 MHz
172	0	-168 MHz	-157 MHz	-11 MHz
172	-1	-1244 MHz	-1255 MHz	11 MHz
170	0	-119 MHz	-104 MHz	-15 MHz
170	-1	-1034 MHz	-1034 MHz	0 MHz
176	-3	$-0.1735\,\mathrm{cm}^{-1}$	$-0.17714\,\mathrm{cm}^{-1}$	109 MHz
176	-4	$-0.3937\,\mathrm{cm}^{-1}$	$-0.3949\,\mathrm{cm}^{-1}$	36 MHz
176	-5	$-0.7515\,\mathrm{cm}^{-1}$	$-0.74267\,\mathrm{cm}^{-1}$	-265 MHz
176	-6	$-1.25375\,\mathrm{cm}^{-1}$	$-1.25072\,\mathrm{cm}^{-1}$	-91 MHz
176	-7	$-1.953\,\mathrm{cm}^{-1}$	$-1.94919\,\mathrm{cm}^{-1}$	-114 MHz

$\mathbf{C_6 = -2740\,E_h a_0^6,\ C_{12} = 3.23615 \cdot 10^8\,E_h a_0^{12}}$

Yb isotope	Δv	exp. value	theor. value	difference
176	-1	-298 MHz	-310 MHz	12 MHz
176	-2	-1767 MHz	-1760 MHz	-7 MHz
174	-1	-235 MHz	-228 MHz	-7 MHz
174	-2	-1483 MHz	-1495 MHz	12 MHz
172	0	-168 MHz	-161 MHz	-7 MHz
172	-1	-1244 MHz	-1253 MHz	9 MHz
170	0	-119 MHz	-108 MHz	-11 MHz
170	-1	-1034 MHz	-1034 MHz	0 MHz
176	-3	$-0.1735\,\mathrm{cm}^{-1}$	$-0.1746\,\mathrm{cm}^{-1}$	33 MHz
176	-4	$-0.3937\,\mathrm{cm}^{-1}$	$-0.3876\,\mathrm{cm}^{-1}$	-183 MHz
176	-5	$-0.7515\,\mathrm{cm}^{-1}$	$-0.7269\,\mathrm{cm}^{-1}$	-737 MHz
176	-6	$-1.25375\,\mathrm{cm}^{-1}$	$-1.2218\,\mathrm{cm}^{-1}$	-958 MHz
176	-7	$-1.953\,\mathrm{cm}^{-1}$	$-1.9015\,\mathrm{cm}^{-1}$	-1544 MHz

Table 5.4.: *Experimental vs. theoretical values for the different Yb isotopes. All theoretical values for this potential can be found in appendix A. The experimental accuracy is* ± 10 MHz *for* $\Delta v > -3$*, otherwise* ± 150 MHz*.*

In these studies, we trapped ^{87}Rb in a magnetic trap at temperatures of $\approx 1\ \mu$K and Yb in a bichromatic optical trap, displaced from the magnetic trap at a temperature of

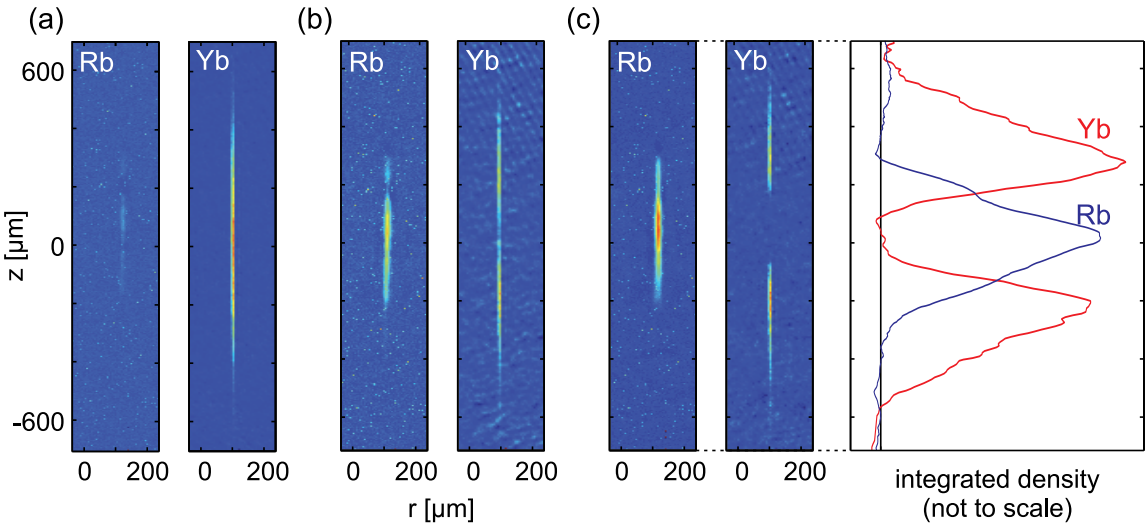

Figure 5.19.: *Intra-trap images of ^{87}Rb and ^{174}Yb after brought in contact. The ^{87}Rb atom number increases from (a) to (c) leading to a separation from the Yb cloud. (c) displays the radially integrated density of the two cluds in the relevant regions. From [4].*

$\approx 10\,\mu$K. The two traps are (nearly) independent for the other species. Details of this setup can be found in [4]. By moving the magnetic trap to the position of the optical trap, the two atomic clouds are brought in contact and thermalization measurements were performed.

We observed peculiar behavior for ^{170}Yb and ^{174}Yb in mixtures with ^{87}Rb. In the measurements with ^{170}Yb, the two atom clouds did not thermalize when the two traps are independent. By changing the power ratio of the two beams of the optical trap, it was possible to enhance the Rb density at the position of the Yb cloud. By this, we were able to measure a thermalization and extract a s-wave scattering length to [4]

$$\left|a_{^{170}\mathrm{Yb},^{87}\mathrm{Rb}}\right| = 6.6^{+3.5}_{-2.9} a_0. \tag{5.43}$$

In a mixture of ^{174}Yb and ^{87}Rb, the two species thermalized instantaneously. At higher Rb densities, we observed a separation of the two clouds, see fig. 5.19. This denotes either a very big positive s-wave scattering length where the interactions pushes the Yb cloud out of the trapping center or a very big negative scattering length with a huge 3-body loss rate. The huge uncertainty of the overlap of the two atom clouds due to the trapping geometry did not allow us to determine s-wave scattering lengths. But a determination of the scattering cross section σ (see eqn. (5.31)) is possible and can be compared to the calculated s-wave scattering lengths. Fig. 5.20 show this comparison. The previously determined cross sections include a constant scaling factor due to the unknown overlap of the two atom clouds.

The other examined Yb isotopes show a thermalization rate without any remarkable findings.

The thermalization data was used by Maxwell and Tiesinga [105] to calculate a Lennard-

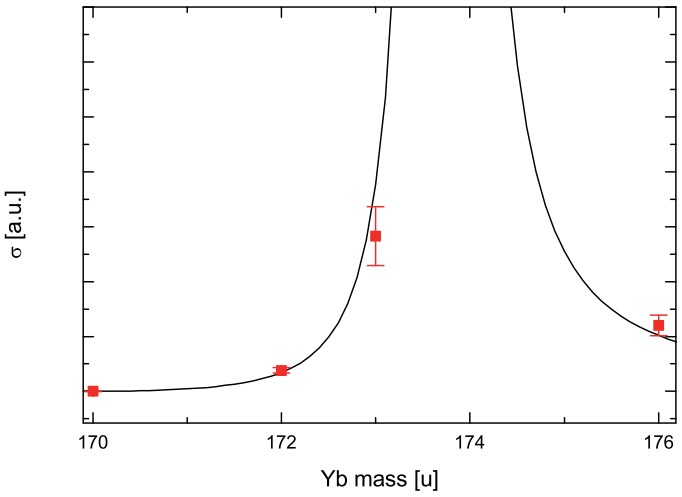

Figure 5.20.: *Black: Calculated scattering cross sections by the determined values for C_6 and C_{12} of the Lennard-Jones potential for the ground state(see text). Red: Measured scattering cross sections in thermalization measurements (data taken from [4]). A constant scaling factor is included due to the unknown overlap of the two atom clouds.*

Jones potential for the YbRb molecule. They determined a C_6 value of $C_6 = -(2740 \pm 140)\ \mathrm{E_h a_0^6}$ and estimated the number of bound states in the potential to 65 ± 6 for the two heaviest isotopologues. For the calculation of the vibrational states and the s-wave scattering lengths, a C_{12} value of $C_{12} = 3.48 \cdot 10^8\ \mathrm{E_h a_0^{12}}$ was used. With the methods described above, it is possible to determine a C_{12} value that is more consistent with the now available binding energies for the vibrational levels. We did this and came to a value of

$$C_{12} = 3.23615 \cdot 10^8\ \mathrm{E_h a_0^{12}} \tag{5.44}$$

This potential gives 66 bound states for the two heaviest isotopologues. The s-wave scattering lengths for the different Yb isotopes can now be calculated to:

$$\begin{aligned} a_{0,170} &= -17 a_0 \\ a_{0,172} &= -185 a_0 \\ a_{0,174} &= 684 a_0 \\ a_{0,176} &= 206 a_0 \end{aligned} \tag{5.45}$$

A comparison to the experimental determined values is shown in tab. 5.4, showing that the difference in some states is much higher than the precision of the experimental data. For that reason, the experimental determined C_6 and the calculated C_{12} seem to be the better values for the potential and will be used for calculations for magnetic Feshbach resonances (chapter 7) and possible routes to rovibrational ground state molecules (chapter 8).

6.

Autler-Townes spectroscopy

A laser which is resonant with a bound-bound transition induces Rabi oscillations which lead to a splitting of the involved states. This splitting can be measured with a second laser probing a transition involving one of these levels and an auxiliary level. This so called Autler-Townes splitting can then be used to determine the strength of the transition. In this chapter, our results of the Autler-Townes spectroscopy in the YbRb molecule will be presented.

6.1. Principle

The experimental setup for Autler-Townes spectroscopy is the same as for 2-Photon-Photoassociation experiments. In fig. 6.1, the principle is shown. The probe laser (2) is fixed to bound-bound transition. This induces a Rabi splitting on the two involved states. The PA laser (1) is scanned and probes the splitting of the excited state.

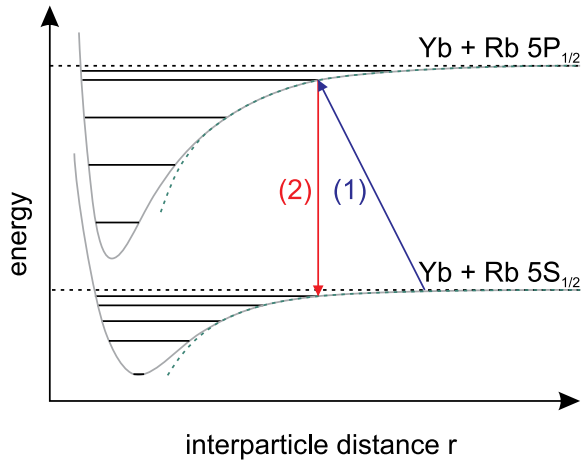

Figure 6.1.: *Principle of Autler-Townes spectroscopy. The probe laser (2) is fixed to a bound-bound transition which induces a splitting of these states. The PA laser (1) is scanned and probes the splitting of the excited state. Adapted from [3].*

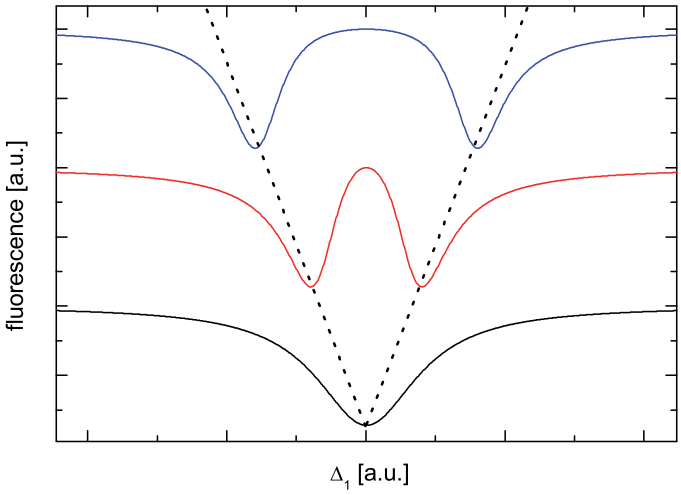

Figure 6.2.: *Principle of Autler-Townes spectroscopy. The black curve shows a typical 1-Photon-Photoassociation resonance without any disturbance. The red and the blue graph show the influence of the probe laser which is resonant to a bound-bound transition and therefore, the resonance splits up into two components according to eqn. (6.1). Note that, in this type of experiment, the PA laser is scanned and therefore, Δ_1 is varied.*

The line shape equation (5.18) was already introduced in chapter 5.4:

$$|S_{1g}|^2 = \frac{(\epsilon/\hbar - \Delta_2)^2 \gamma_p \gamma_s/(2\pi)^2}{((\epsilon/\hbar - \Delta_+)(\epsilon/\hbar - \Delta_-))^2 + (\gamma/4\pi)^2 (\epsilon/\hbar - \Delta_2)^2}$$
$$\text{with} \quad \Delta_\pm = \frac{1}{2}(\Delta_1 + \Delta_2) \pm \frac{1}{2}\sqrt{(\Delta_1 - \Delta_2)^2 + \left(\frac{\Omega}{2\pi}\right)^2}. \tag{6.1}$$

The splitting of the two resonances is then defined as

$$\Delta = \Delta_+ - \Delta_- = \sqrt{\delta^2 + \left(\frac{\Omega}{2\pi}\right)^2} \tag{6.2}$$

with δ being the detuning of the probe laser from the resonance of the bound-bound transition. The Rabi frequency Ω depends on the intensity of the probe laser and the transition strength:

$$\Omega = |\langle a|b\rangle| \, \gamma_1 \sqrt{\frac{I}{4I_{sat}}} \tag{6.3}$$

Here, I is the intensity of the probe laser and I_{sat} is the saturation intensity of the atomic transition with $I_{sat} = \pi hc\gamma_1/(3\lambda^3)$. The overlap integral of the two levels a and b are connected through the Franck-Condon factor

$$f_{\mathrm{FC}} = |\langle a|b\rangle|^2 \tag{6.4}$$

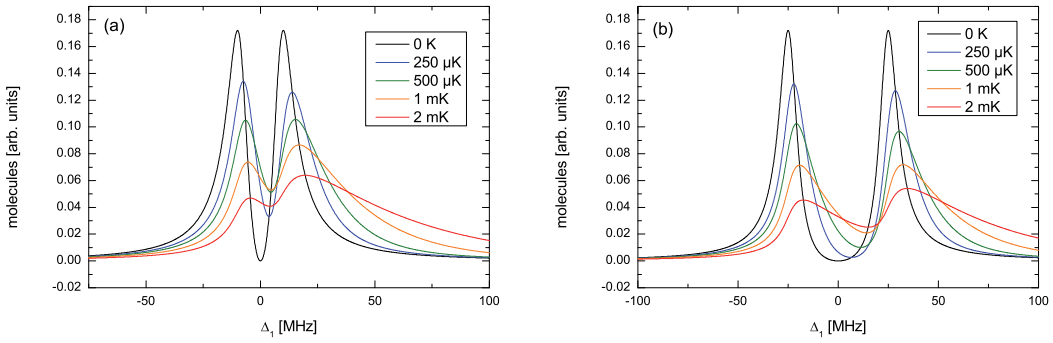

Figure 6.3.: *Temperature dependence of Autler-Townes spectroscopy. (a)* $\Omega = 20$ MHz, *(b)* $\Omega = 50$ MHz. *The splitting differs less than 2 MHz.*

giving the transition probability. Fig. 6.2 shows how a transition splits up in principle. In black, the undisturbed resonance of the 1-Photon-Photoassociation is shown. The red and the blue curve differ only by the intensity of the probe laser showing an increase of the splitting of the transition with increasing intensity. The intensity of the laser in the blue curve is 4 times the intensity in the red curve giving twice the splitting according to a squareroot correlation.

Eqn. (6.1) is only valid for zero temperature. Under typical experimental conditions, thermal averaging has to be taken into account according to [102]

$$K = \frac{1}{hQ_T} \int |S_{1g}|^2 \, e^{-\epsilon/k_B T} d\epsilon \tag{6.5}$$

where $Q_T = (\frac{2\pi k_B T \mu}{h^2})^{3/2}$ is the partition function with μ being the reduced mass. Calculations with different temperatures show that the splitting differs less than 2 MHz in the regime up to 2 mK and can therefore be neglected. Fig. 6.3 shows typical Autler-Townes doublets at different temperatures. Only the shape of the two peaks is changed, but not the splitting if the temperature is increased.

The splitting of the two peaks is not only dependent on the intensity of the probe laser, but also on the detuning of this laser to the resonance. The splitting gets broader according to eqn. (6.2) and the height of each peak is changed[1] if the detuning is increased. In fig. 6.4 some examples with different detunings are shown. The more the probe laser is detuned from the resonance, the lower is the second peak. The deeper peak is approaching the non-disturbed resonance with larger detuning of the probe laser.

6.2. Autler-Townes spectroscopy in ^{176}Yb^{87}Rb

The experimental setup for the Autler-Townes spectroscopy is exactly the same as for the 2-Photon-Photoassociation experiments. The two atom clouds are trapped in a continuously

[1] At zero temperature, this is not true. Only the width of the peaks changes.

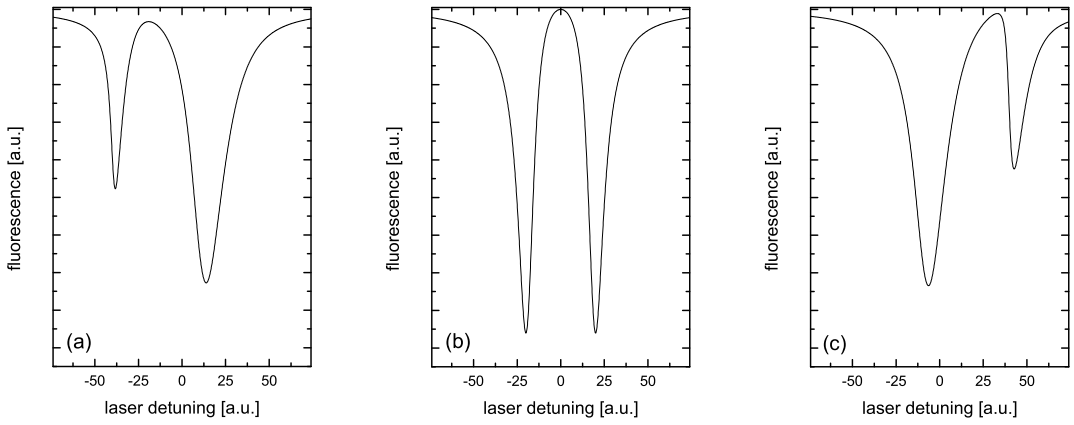

Figure 6.4.: *Principle of Autler-Townes spectroscopy. Shown is the splitting of one resonance at a temperature of* $250\,\mu$K *at different detunings* δ *of Laser 2. (a)* $\delta < 0$*, (b)* $\delta = 0$*, (c)* $\delta > 0$*.*

loaded MOT. The PA laser is scanned and the fluorescence of the two clouds is recorded. Whenever the PA laser hits a resonance, two atoms can associate to a molecule and are lost from the trap. Therefore, at resonance less atoms are in the MOT and less fluorescence is measured. The probe laser is locked to a known bound-bound transition as determined with the 2-Photon-PA measurements. For this, the PA laser is brought onto the desired 1-Photon-PA resonance by observing the Yb fluorescence which is lowest on resonance. Then, the probe is brought onto the 2-Photon-PA resonance. At the resonance, the Yb fluorescence rises to a maximum. The probe laser is then locked and the PA laser will be scanned. The disturbance of the probe laser leads to the described splitting of the state which is probed by the PA laser.

A typical 1-Photon-PA resonance is shown in fig. 6.5 (a). The probe laser will interact with all rotational components and subcomponents of the resonance with a different detuning with respect every component. We already learned (see chapter 5.5.2) that the three subcomponents of the $R' = 1$ component couple to the same ground state level $R = 1$ and that the $R' = 0$ component couples to the different rotational ground state $R = 0$. An example scan is given in fig. 6.5 (b). Here, the probe laser is fixed to the resonance of $R' = 1, \Delta_R = +1 \leftrightarrow R = 1$. This is the only state which splits up visibly. The other components do not split up because of the relatively large detuning of the probe laser: For the other two subcomponents of the $R' = 1$ component, this laser is detuned by the splitting. For the $R' = 0$ component, the detuning is further modified by the rotation since it couples to the $R = 0$ ground state. The same argument holds for the $\Delta_R = -1$ component where only this state splits up (see fig. 6.5 (c)).

In measurements with the probe laser locked to the $\Delta_R = 0$ component, something unexpected happens: In fig. 6.5 (d), it is visible, that not only the desired resonance

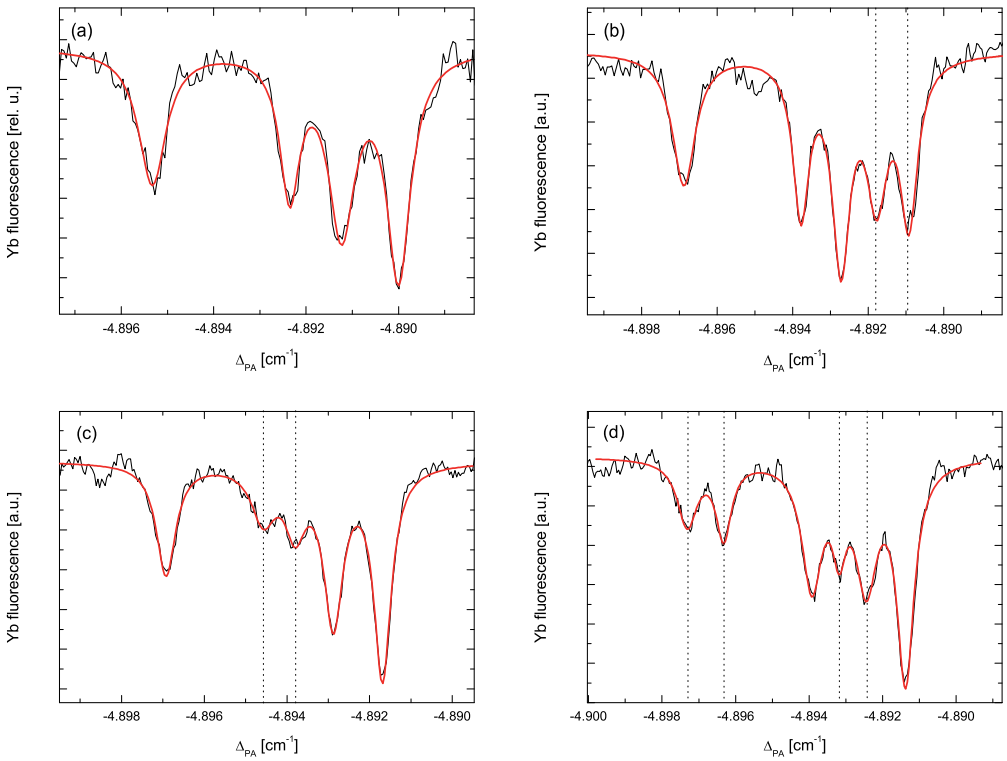

Figure 6.5.: *(a) undisturbed 1-Photon-PA signal. (b), (c) The probe laser fixed to the resonance at the rotational subcomponent (b)$\Delta_R = +1$, (c)$\Delta_R = -1$ leading to a splitting of this state. In (d), the probe laser is locked to the rotational subcomponent $\Delta_R = 0$ leading to a splitting in this state and also the $R = 0$ component splits up. The red curve is a simple fit function with Lorentz shaped resonances.*

splits up, but also the $R' = 0$ component. The splittings of the two components have the same magnitude. An explanation of this behavior is that we used the broadest 2-Photon-Photoassociation resonance we found in this experiment, which is the $F = 1, \Delta v = -6$ vibrational level (when we use level $|II\rangle$ for probing). Since the resonance is such big, the overlap of the wavefunctions of this vibrational level and the excited state must be very high. This means, that the outer turning points must be near to each other and denotes, that the size of the molecule is nearly the same and therefore, the rotational constant has the same magnitude. Thus, the distance between the rotational levels of the ground and excited state must be the same and the probe laser is not only resonant with the $R' = 1, \Delta_R = 0 \leftrightarrow R = 1$ transition, but also with the $R' = 0 \leftrightarrow R = 0$ transition. This is the reason why the two resonances split up. This also confirms the proposal, that the rotational quantum number is not changed in 2-Photon-PA experiments in YbRb (see chapter 5.5.2).

Using the line shape equation (6.1), we can construct the full spectrum with the probe laser present. In fig. 6.6 (a), the equation was used to calculate each resonance for itself.

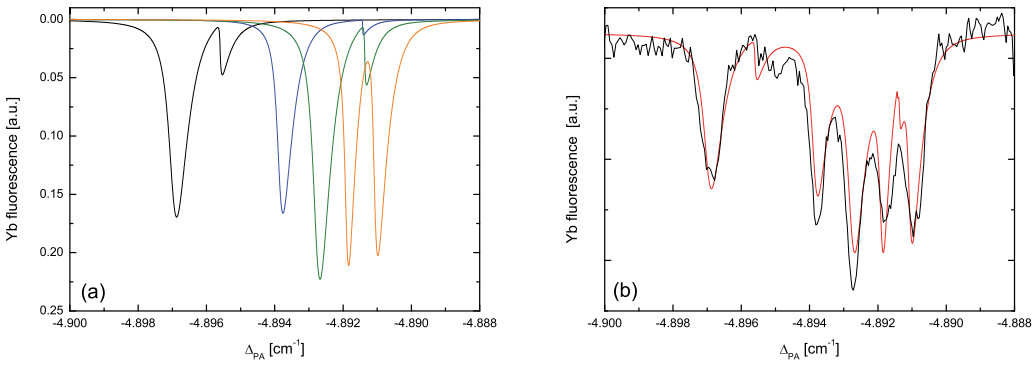

Figure 6.6.: *Theoretical curve of the Autler-Townes spectroscopy with laser 2 locked to the $R' = 1, \Delta_R = +1$ component. In (a), the theoretical curve for each resonance is shown including the detuning. In (b), the measured values are shown in black together with the sum of the 4 curves from (a).*

In (b), the sum of these four curves is shown. This fairly reconstructs the measured data, as shown in the figure. This confirms our theoretical model and explains that the splitting of the other components is not visible. Nevertheless, the more simple function using 5 Lorentz shaped equations gives the same results for the splitting of the states, which is the important information.

In a next step, we varied the intensity of the probe laser to reconstruct the dependence of the splitting to the intensity. The splitting is defined as (see eqn. (6.2))

$$\Delta = \sqrt{\delta^2 + \left(\frac{\Omega}{2\pi}\right)^2} = \sqrt{\delta^2 + |\langle a|b\rangle|^2 \left(\frac{\gamma_1}{2\pi}\right)^2 \frac{1}{4I_{\mathrm{sat}}} I} \tag{6.6}$$

with δ being the detuning from the resonance and I being the intensity of the probe laser. The Rabi frequency $\Omega/2\pi$ is defined through the Franck-Condon factor $f_{\mathrm{FC}} = |\langle a|b\rangle|^2$ of the two states a and b. In fig. 6.7 (a), we locked the probe laser to the transition $|I_1\rangle \leftrightarrow |F = 1, \Delta v = -5, R = 1\rangle$ and varied the intensity of this laser. The black curve represents the experiment with no detuning of this laser while in the red curve we applied a detuning to the resonance of $\delta = 78$ MHz. The lines are fits according to eqn. (6.6). Thus, we find good agreement between the theoretical model and our experimental results.

In a second experiment, we kept the intensity of the probe laser constant and changed the detuning of this laser. The change of detuning was measured with a scanning Fabry-Perot interferometer, where a frequency stabilized laser and the probe laser were injected. The difference between the peaks of the two lasers then gives the relative detuning. This is the same principle that is used to lock the laser. Fig. 6.7 (b) shows the results of this measurement. The line is a fit according to eqn. (6.6).

With the help of the Autler-Townes spectroscopy, it is possible to determine the overlap of the two wavefunctions of the involved levels. The splitting Δ is directly dependent on

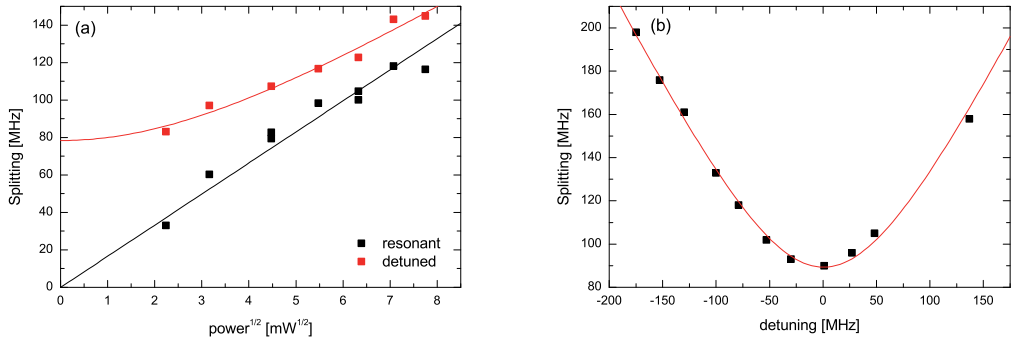

Figure 6.7.: *(a) Autler Townes splitting with different intensities of the probe laser. The probe laser is resonant (black) respectively detuned from resonance (red). (b) Autler Townes splitting with different detunings of the probe laser.*

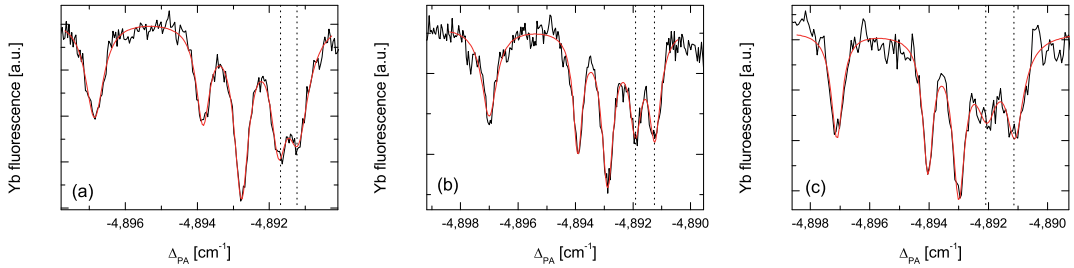

Figure 6.8.: *Example scans with different intensities of laser 2: (a) 1.4 mW, (b) 4 mW, (c) 9.3 mW. Laser 2 is locked to the $R' = 1, \Delta_R = +1$ resonance, the splitting is marked with the dotted lines.*

this factor, see eqn. (6.6). The Franck-Condon factor f_{FC}, only dependent of the overlap of the wavefunctions, gives the transition probability. For the creation of molecules, a large Franck-Condon factor is desirable.

For determination of the Franck-Condon factor, we repeated the measurement with the probe laser resonant to different 2-Photon-PA resonances. The Franck-Condon factor can be calculated from eqn (6.6) as

$$f_{\mathrm{FC}} = |\langle a|b\rangle|^2 = \frac{\Omega^2}{\gamma_1^2}\frac{4I_{sat}}{I} \tag{6.7}$$

with the saturation intensity $I_{\mathrm{sat}} = 1.496\,\mathrm{mW/cm^2}$ for the Rb D_1 transition and $\gamma_1/2\pi = 5.75\,\mathrm{MHz}$ being the linewidth of this transition. Example scans with different intensities of the probe laser are shown in fig. 6.8. The squareroot-dependence of the intensity of the probe laser against the splitting of the resonance is shown in fig. 6.9. In this example, the used transition $|II_1\rangle \leftrightarrow |F = 1, \Delta v = -6\rangle$ leads to a Franck-Condon factor of

$$f_{\mathrm{FC}} = 0.20 \pm 0.02. \tag{6.8}$$

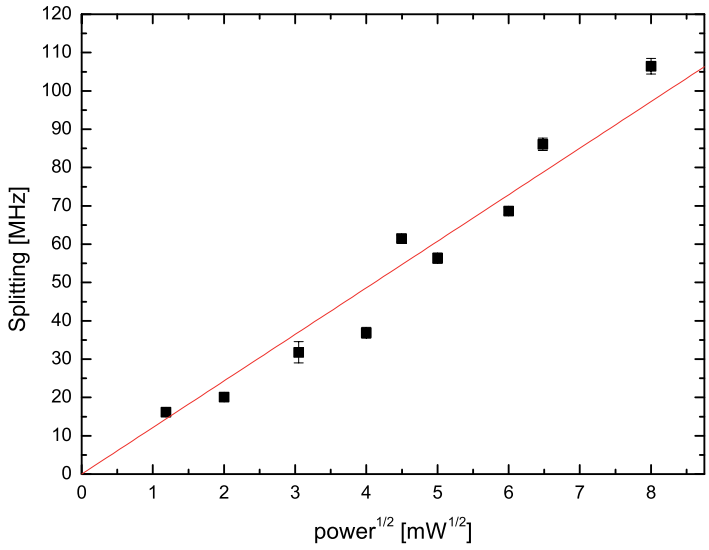

Figure 6.9.: *Splitting vs. squareroot of the intensity*

excited level $\Delta v'$	ground state level Δv	$f_{\mathrm{FC,AT}}$	$f_{\mathrm{FC,2PA}}$
-11	-4 (F=1)	0.034	0.03
	-6 (F=1)	0.29 ± 0.08	0.13
	-6 (F=2)	0.032	0.07
	-7 (F=1)	0.031	0.05
	-7 (F=2)	0.010	0.05
-9	-5 (F=1)	0.37	0.20

Table 6.1.: *Measured Franck-Condon factors for different transitions in $^{176}Yb^{87}Rb$. The last column is giving the Franck-Condon factors as determined in 2-Photon-PA experiments, see chapter 5.6.2 for details.*

The given error bar is the statistical error from the fit function. More measurements on this transition show that the real uncertainties are much higher. They are attributed to the overlap of the two lasers and the intensity distribution of the laser beams over the atomic cloud. In tab. 6.1, the determined Franck-Condon factors for different states are given. Note that the transition probability of the $F' = 2, \Delta v' = -11 \leftrightarrow F = 1, \Delta v = -6$ is different than given in (6.8) because of more measurements for this transition.

7.

Prediction of the positions of Feshbach resonances in YbRb

In samples of ultracold atoms, molecules can be formed with the help of magnetic fields by making use of so-called Feshbach resonances. For this, the atoms need two ground states with a coupling between them. Magnetic Feshbach resonances were reported up to now only in samples of alkali metals and were first reported in homonuclear mixtures with ^{85}Rb [26] and ^{23}Na [27], the first heteronuclear magnetic Feshbach resonances were reported in KRb [10].

It was commonly believed that for a combination of alkali atoms and alkaline earth like atoms, no coupling exists. But, Zuchowski et al.[8] and Brue et al. [9] showed theoretically that a small coupling exists in these mixtures which may be sufficient to form molecules by magnetic fields. In this chapter, calculations for the mixture of Rb and Yb based on the experimental results of the 2-Photon-PA experiments (see chapter 5) will be shown and predictions for Feshbach resonances will be given.

7.1. Introduction

Feshbach resonances can be explained in a simple picture: Consider two molecular potentials, as shown in fig. 7.1 (a). The energetically lower potential will connect for large distances to the case of two free atoms (open channel). This is the entrance channel for the resonance. The second potential (closed channel) must have a bound state near the threshold of the entrance channel. When the magnetic moments of the two states are different, the relative energies can be tuned by magnetic fields. Whenever the energy of a bound state is equal to the energy of the two free atoms, a Feshbach resonance can occur. A coupling between the two states can lead to a strong mixing [109].

Such a magnetically tuned Feshbach resonance also changes the s-wave scattering length according to [110]

$$a(B) = a_{\mathrm{bg}} \left(1 - \frac{\Delta}{B - B_0} \right). \tag{7.1}$$

Here, a_{bg} is the background scattering length which is the scattering length for off-resonant values of the magnetic field B. The parameter B_0 is the resonance position in which the scattering length diverges and Δ is the width of the resonance. This was introduced in

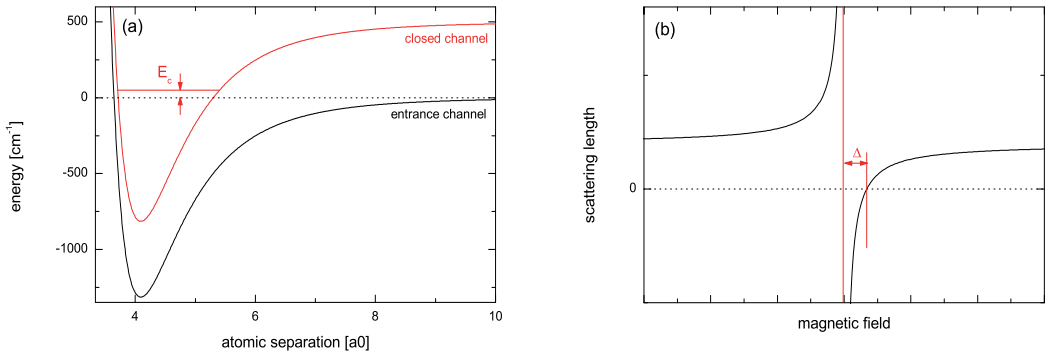

Figure 7.1.: *Scheme for a Feshbach resonance. (a) The two atoms can collide in the entrance channel which is coupled to a molecular bound state E_c (that belongs to the closed channel). Resonant coupling occurs when the energy difference between the entrance channel and the molecular level is zero. This can be achieved by magnetically tuning the two states. Note that the energy difference between the entrance and the closed channel is enhanced here. (b) The scattering length is changing dramatically near a Feshbach resonance. On resonance, it has a pole and changes its sign. The width Δ of a Feshbach resonance is defined as the distance between the pole and the zero crossing.*

[110]. Note that the width Δ can be positive or negative. The width corresponds to the distance between the resonances and the zero crossing of the scattering length which occurs at the magnetic field $B = B_0 + \Delta$. In fig. 7.1 (b), the change of the scattering length around a Feshbach resonance is shown (in this case with a positive width).

In experiments, a Feshbach resonance can be observed by an increased loss of atoms because the scattering length is changing dramatically near the resonance and therefore three-body-recombinations and formation of molecules are enhanced. An observation of a Feshbach resonance was first reported in [26, 27].

A Feshbach resonance can also be used to associate atoms to molecules [24]. By ramping the magnetic field across a Feshbach resonance, it is possible to form so called Feshbach molecules which are molecules in a high vibrational level in the electronic ground state. More on the creation of such molecules will be given in section 8.1.

7.2. Magnetic Feshbach resonances in YbRb

In [8] and [9], it was shown, that there is a coupling between the two ground states in a mixture of an alkali and an alkaline earth metal (respective alkaline earth-like metal like Yb). The possible Feshbach resonances and the widths of these resonances were calculated for the mixture Rb and Sr respective Li and Yb. Since there is only very little knowledge of the ground state potentials of these mixtures, the given positions of the Feshbach resonances are only estimates with huge error bars. In contrast to this, in the mixture of Rb and Yb (which has the same electronic structure as the examined mixtures), we measured the

binding energies of the ground state levels and can give more precise predictions of the positions of Feshbach resonances.

Feshbach resonances that might be used to associate free atoms to molecules occur at magnetic fields where the molecular levels cross the atomic levels. Because Yb has no magnetic moment, the molecular Hamiltonian is nearly diagonal in a basis set of atomic functions, so that the molecular levels lie parallel to the atomic thresholds [9]. Thus, for a calculation of the resonances, we only need to know the atomic thresholds, which can be calculated with the help of the Breit-Rabi formula [111] and the positions of the last vibrational states in the ground state potential of the molecule, which we determined with the 2-Photon-Photoassociation measurements and modeling of the ground state potential (see chapter 5 for details).

7.2.1. Breit-Rabi formula

For weak magnetic fields, the atomic levels split up linear as a function of the magnetic field. This effect is called the anomalous Zeeman effect. For strong fields, the levels split up in the strong-field eigenstates $|J, m_J, I, m_I\rangle$. This is the Paschen-Back effect. For intermediate fields, that we can control here, the energy shift in atoms with a $J = 1/2$ state (e.g. a $^2S_{1/2}$ state) can be calculated with the Breit-Rabi formula [111]:

$$E_{|J=1/2,m_J,I,m_I\rangle} = -\frac{\Delta E_{hfs}}{2\,(2I+1)} + g_I\,\mu_B\,m\,B \pm \frac{\Delta E_{hfs}}{2}\left(1 + \frac{4mx}{2I+1} + x^2\right)^{1/2} \tag{7.2}$$

with $\Delta E_{hfs} = A_{hfs}(I + 1/2)$ being the hyperfine splitting, $m = m_I \pm m_J$ is the magnetic quantum number (in this case: $m = m_I \pm 1/2$) and

$$x = \frac{(g_J - g_I)\,\mu_B B}{\Delta E_{hfs}}. \tag{7.3}$$

Here, g_J and g_I are the Landé factors specific for the atom. The atomic constants for ^{85}Rb and ^{87}Rb are listed in tab. 7.1. Fig. 7.2 shows the behaviour of the energy levels of the Rb ground state in an external magnetic field.

		^{85}Rb	^{87}Rb
Nuclear Spin	I	5/2	3/2
Nuclear g-factor	g_I	-0.000294	-0.000995
Fine Structure Landé g-factor	g_J	2.002331	2.002331
Magnetic Dipole Constant	A_{hfs}	$h \cdot 1.011911$ GHz	$h \cdot 3.417341$ GHZ

Table 7.1.: *Properties of the Rb ground state $^2S_{1/2}$. Here, h is Planck's constant. From [59].*

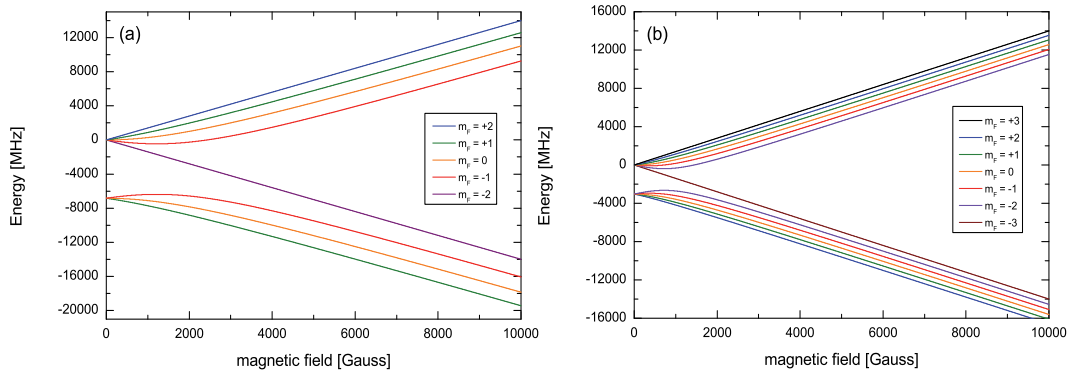

Figure 7.2.: *Energy levels of the (a)^{87}Rb and (b)^{85}Rb ground state in a magnetic field.*

7.2.2. Vibrational levels of the ground state of the YbRb molecule

For the determination of magnetic Feshbach resonances that are experimentally accessible, only molecular vibrational levels that have a binding energy in the range of the hyperfine splitting of Rb have to be considered. The energetic positions of the relevant vibrational levels for all possible isotopic combinations can be calculated solving the Schrödinger equation for the Lennard-Jones potential that was calculated in chapter 5.8

$$V(r) = C_{12}/r^{12} + C_6/r^6 \tag{7.4}$$

with the coefficients

$$\begin{aligned} C_6 &= -2563\,\mathrm{E_h a_0^6}, \\ C_{12} &= 2.7412 \cdot 10^8\,\mathrm{E_h a_0^{12}}. \end{aligned} \tag{7.5}$$

The relevant levels are listed in tab. 7.2.

7.3. Positions of Feshbach resonances in YbRb

For mixtures of Rb and Yb containing bosonic Yb with zero spin, the conservation of angular momenta requires that the m_F projection is conserved for a coupling between atomic and molecular potentials to occur [8]. Therefore, possible magnetic Feshbach resonances can only occur at crossings with $\Delta m_F = 0$. In fig. 7.3, the change of the molecular and atomic levels with mixtures of the bosonic isotopes of Yb and ^{87}Rb in an external magnetic field is shown. Additionally, the open circles denote crossings with the same m_F. These are the positions of potential Feshbach resonances. In mixtures with ^{87}Rb, there are only three resonances for all bosonic Yb isotopes combined within a magnetic field of up to 1500 G that can be reached easily in experiments. Additionally, one of these resonances is in the mixture with ^{168}Yb which has natural abundance of only 0.13 % [60]. The most promising resonance is found in a mixture of ^{170}Yb and ^{87}Rb at 1246 G.

Δv	^{168}Yb^{87}Rb	^{170}Yb^{87}Rb	^{171}Yb^{87}Rb	^{172}Yb^{87}Rb	^{173}Yb^{87}Rb
0	-63	-104	-128	-157	-188
-1	-836	-1034	-1141	-1255	-1375
-2	-3255	-3723	-3968	-4221	-4482
-3	-8255	-9098	-9533	-9977	-10430
-4	-16767	-18086	-18761	-19444	-20136

Δv	^{174}Yb^{87}Rb	^{176}Yb^{87}Rb
0	—	-1.6
-1	-223	-305
-2	-1501	-1770
-3	-4751	-5310
-4	-10891	-11839
-5	-20837	-22265

Δv	^{168}Yb^{85}Rb	^{170}Yb^{85}Rb	^{171}Yb^{85}Rb	^{172}Yb^{85}Rb	^{173}Yb^{85}Rb
0	-1.4	-7.0	-12	-18	-26
-1	-310	-414	-473	-536	-605
-2	-1823	-2141	-2311	-2487	-2670
-3	-5500	-6141	-6474	-6815	-7165
-4	-12294	-13361	-13909	-14465	-15030

Δv	^{174}Yb^{85}Rb	^{176}Yb^{85}Rb
0	-37	-63
-1	-678	-838
-2	-2859	-3258
-3	-7521	-8259
-4	-15603	-16774

Table 7.2.: *Calculated binding energies in MHz of the different vibrational states Δv in the ground state for different isotopes. The accuracy is estimated to* ± 10 MHz.

The situation is different for mixtures with ^{85}Rb. In fig. 7.4, the possible Feshbach resonances are shown. In the range up to 1500 G, many resonances are available making ^{85}Rb the better choice for the investigation of magnetic Feshbach resonances.

The width of possible Feshbach resonances are not known yet and up to now, calculations for Rb and Yb mixtures are not available. But calculations exist for the case of LiYb [9] and RbSr [8], which have the same structure as YbRb. The calculations for Li and Yb [9] show, that these resonances will be extremely narrow. The calculated widths are typically less than 50 μG which will be very hard to explore in experiments. In [8], the width of such resonances in RbSr has been determined to be much broader for states with $m_F < 0$ that cross the atomic level twice with the higher-field resonance being the

broader one. In mixtures with ^{87}Rb, such a case does not occur, but it does occur in ^{172}Yb^{85}Rb and ^{174}Yb^{85}Rb making the two resonances at 1091 G (^{172}Yb^{85}Rb) respective 1346 G (^{174}Yb^{85}Rb) the best choice to search for Feshbach resonances. Additionally for ^{174}Yb^{85}Rb, the $m_F = -1$ state nearly crosses the atomic state with a distance of only about 3 MHz that is below the accuracy of our calculations. So, this state at $B = 361$ G could possibly also provide a resonance with a large width.

An additional mechanism occurs for Yb isotopes with nonzero nuclear spin (^{171}Yb, $I = 1/2$ and ^{173}Yb, $I = 5/2$). Due to hyperfine coupling, a coupling can occur for transitions with $\Delta m_F = \pm 1$ and it has been calculated for LiYb [9], that these resonances are much broader in the range of up to 2.8 mG. In fig. 7.5, the combinations of fermionic Yb and ^{87}Rb are shown. The open circles denote possible Feshbach resonances with $\Delta m_F = 0$ and filled circles denote resonances with $\Delta m_F = \pm 1$ which are predicted to be broader. In fig. 7.6, the same is shown for combinations of various Yb isotopes with ^{85}Rb. Here, in ^{173}Yb^{85}Rb, the $m_F = -1$ ($m_F = -2$) atomic state crosses the $m_F = -2$ ($m_F = -1$) molecular state twice at the filled red (violet) circles, which makes this a very interesting candidate for the investigation of Feshbach resonances in YbRb since two meachnisms for broadening are combined here. The resonances both occur near 762 G and therefore are well below 1000 G and are thus relatively easy to reach in experiments.

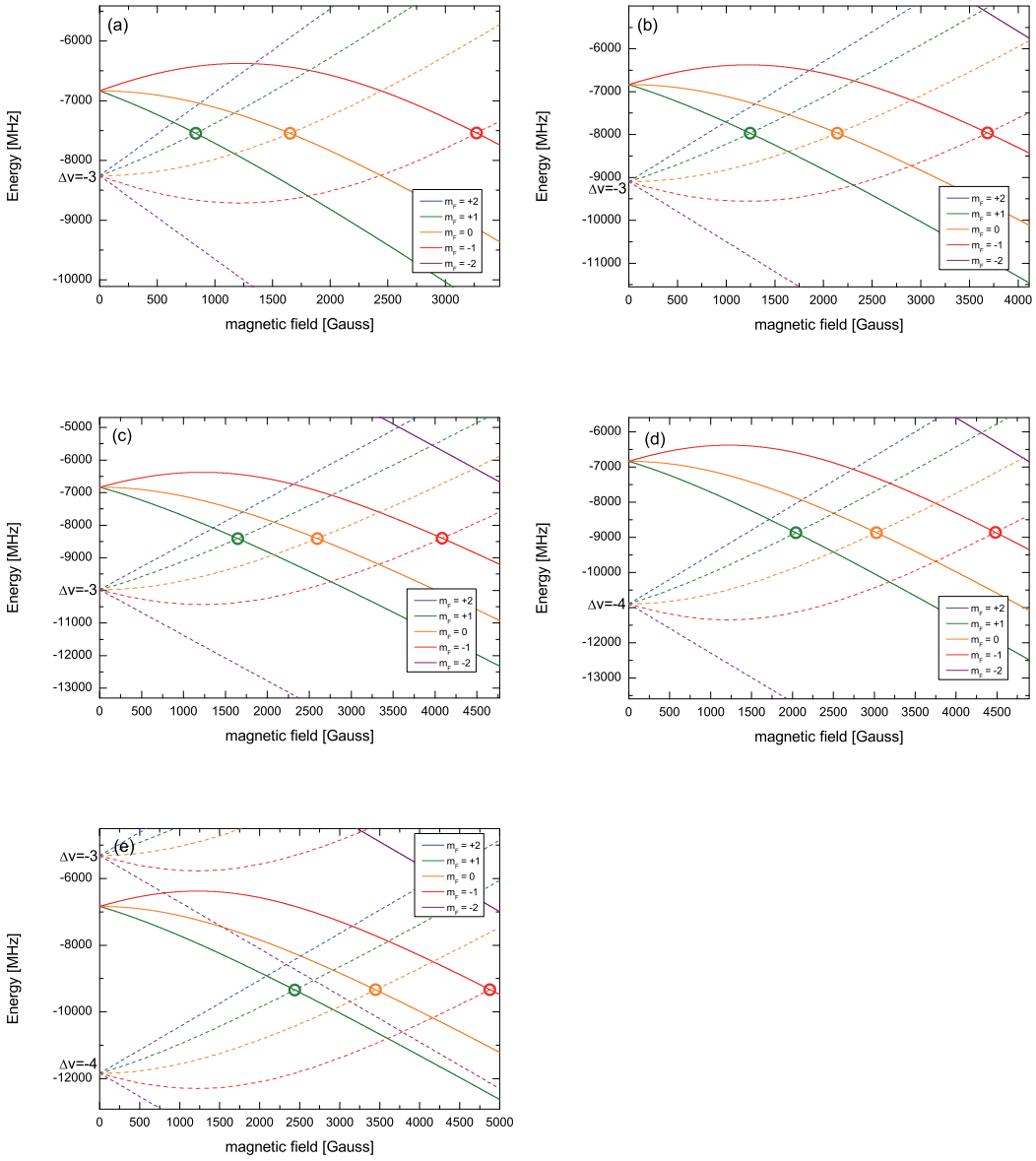

Figure 7.3.: *Plot of the energy levels shifted by the binding energy of the molecular states for ^{87}Rb. The atomic states of ^{87}Rb are shown in solid lines, while molecular levels are shown in broken lines. Depicted are molecular levels for mixtures of ^{87}Rb and the bosonic isotopes (a)^{168}Yb,(b)^{170}Yb,(c)^{172}Yb,(d)^{174}Yb and (e)^{176}Yb with spin zero. Possible Feshbach resonances are marked with open circles ($\Delta m_F = 0$).*

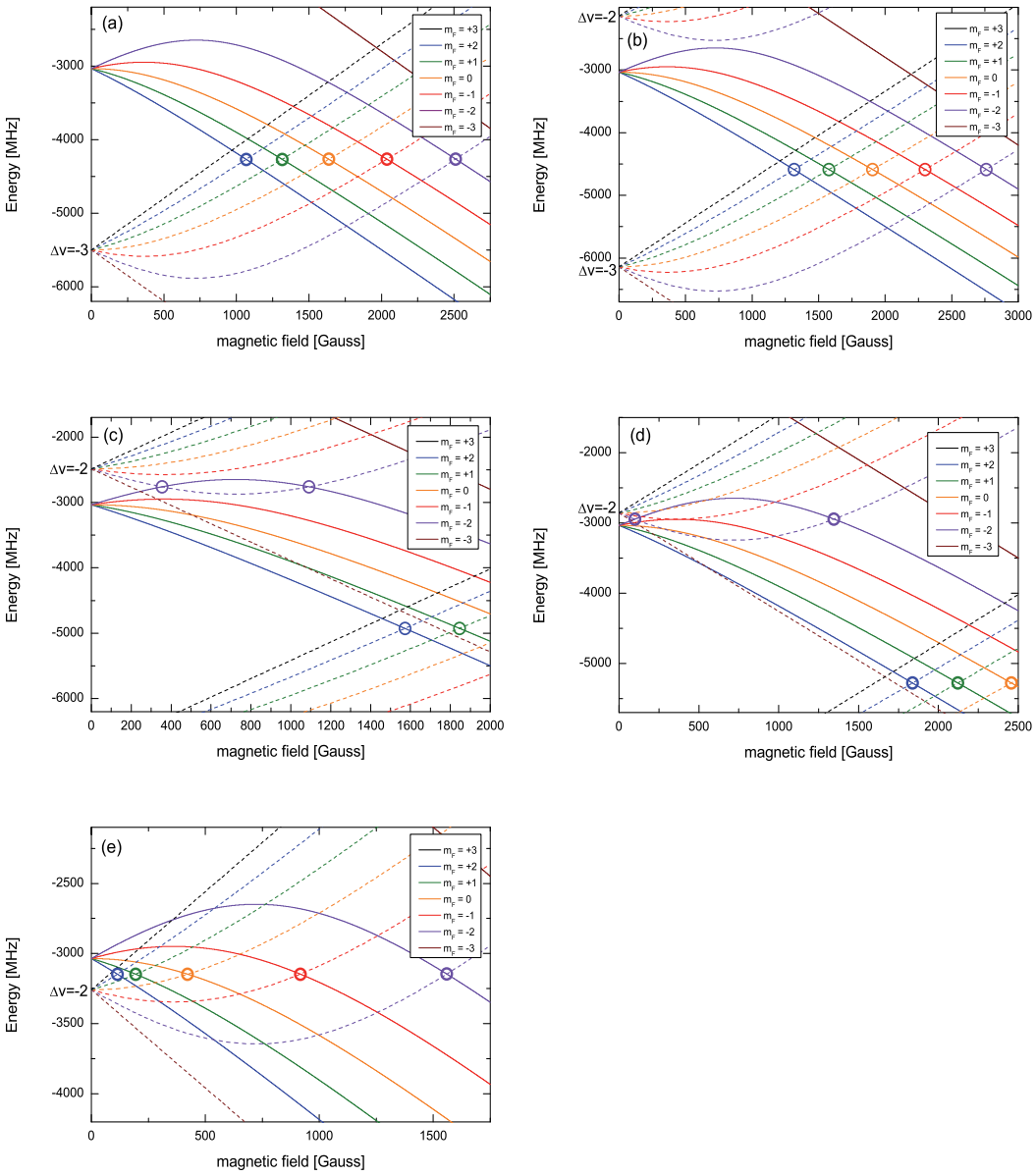

Figure 7.4.: *Possible magnetic Feshbach resonances in mixtures of* ^{85}Rb *and (a)*^{168}Yb*, (b)*^{170}Yb*, (c)*^{172}Yb*, (d)*^{174}Yb *and (e)*^{176}Yb*. The solid lines show the atomic Rb positions, the broken lines denote molecular states. A magnetic Feshbach resonance is possible when* $\Delta m_F = 0$.

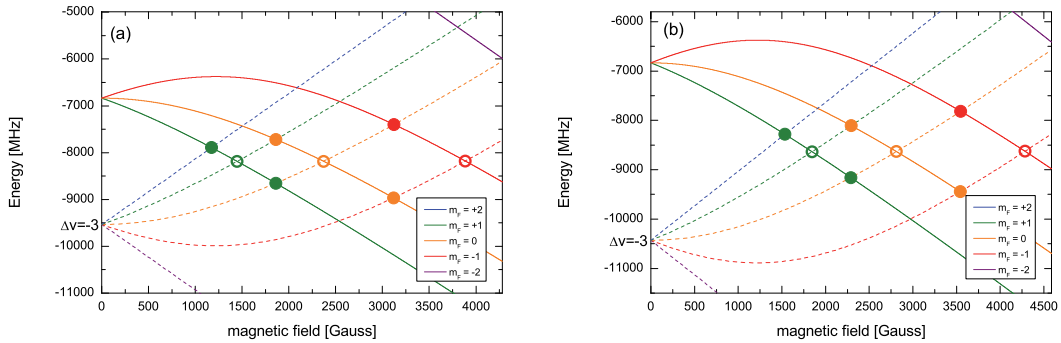

Figure 7.5.: *Plot of the energy levels shifted by the binding energy of the molecular states for ^{87}Rb. The atomic states of ^{87}Rb are shown in solid lines, while molecular levels are shown in broken lines. Depicted are molecular levels for mixtures of ^{87}Rb and the fermionic isotopes (a)^{171}Yb,(b)^{173}Yb. Possible Feshbach resonances are marked with open circles ($\Delta m_F = 0$) respectively full circle ($\Delta m_F = \pm 1$).*

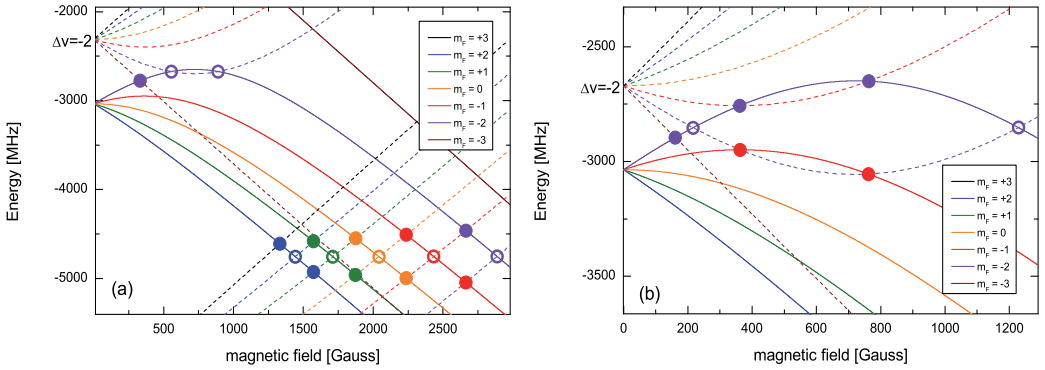

Figure 7.6.: *Possible magnetic Feshbach resonances in mixtures of ^{85}Rb and (a)^{171}Yb, (b)^{173}Yb. The solid lines show the atomic Rb positions, the broken lines denote molecular states. A magnetic Feshbach resonance is possible when $\Delta m_F = 0$ (denoted by open circles) and when $\Delta m_F = \pm 1$ (filled circles).*

system	Δv	m_F	magnetic field	system	Δv	m_F	magnetic field
^{168}Yb^{85}Rb	-3	+2	1067	^{168}Yb^{87}Rb	-4	+1	834
		1	1315			0	1652
		0	1637			-1	3272
		-1	2038				
		-2	2512				
^{170}Yb^{85}Rb	-3	+2	1315	^{170}Yb^{87}Rb	-4	+1	1246
		1	1578			0	2143
		0	1905			-1	3685
		-1	2300				
		-2	2760				
^{172}Yb^{85}Rb	-2	-2	354	^{172}Yb^{87}Rb	-4	+1	1646
		-2	1091			0	2593
	-3	+2	1572			-1	4085
		+1	1846				
		0	2178				
		-1	2569				
		-2	3017				
^{174}Yb^{85}Rb	-2	-2	99	^{174}Yb^{87}Rb	-4	+1	2043
		-2	1346			0	3026
	-3	+2	1838			-1	4481
		+1	2121				
		0	2456				
		-1	2844				
		-2	3282				
^{176}Yb^{85}Rb	-2	+2	114	^{176}Yb^{87}Rb	-4	+1	2439
		+1	194			0	3449
		0	422			-1	4878
		-1	917				
		-2	1559				

Table 7.3.: Positions of possible magnetic Feshbach resonances in mixtures of Rb and the bosonic isotopes of Yb. Given is the vibrational level Δv, as defined in chap. 5 of the molecular ground state of YbRb and the quantum number m_F of Rb. The positions are given in Gauss, the accuracy is ± 5 Gauss.

system	Δv	m_F	magnetic field	system	Δv	m_F	magnetic field
^{171}Yb^{85}Rb	-2	-2	555	^{171}Yb^{87}Rb	-4	+1	1447
		-2	890			0	2371
		$-2 \rightarrow -3$	331			-1	3886
	-3	+2	1443			$1 \rightarrow 2$	1174
		+1	1712			$0 \rightarrow 1$	1863
		0	2041			$-1 \rightarrow 0$	3123
		-1	2434			$1 \rightarrow 0$	1860
		-2	2887			$0 \rightarrow -1$	3119
		$+2 \rightarrow +1$	1573				
		$+1 \rightarrow 0$	1873				
		$0 \rightarrow -1$	2237				
		$-1 \rightarrow -2$	2663				
		$+2 \rightarrow +3$	1331				
		$+1 \rightarrow +2$	1574				
		$0 \rightarrow +1$	1874				
		$-1 \rightarrow 0$	2237				
		$-2 \rightarrow -1$	2664				
^{173}Yb^{85}Rb	-2	-2	216	^{173}Yb^{87}Rb	-4	+1	1845
		-2	1228			0	2811
		$-2 \rightarrow -3$	161			-1	4283
		$-1 \rightarrow -2$	362			$1 \rightarrow 2$	1535
		$-1 \rightarrow -2$	762			$0 \rightarrow 1$	2293
		$-2 \rightarrow -1$	362			$-1 \rightarrow 0$	3546
		$-2 \rightarrow -1$	763			$1 \rightarrow 0$	2290
						$0 \rightarrow -1$	3542

Table 7.4.: Positions of possible magnetic Feshbach resonances in mixtures of Rb and the fermionic isotopes of Yb. Given is the vibrational level Δv, as defined in chap. 5 of the molecular ground state of YbRb and the quantum number m_F of Rb. If the quantum number is changed, the first number is the atomic state and the second one of the molecular state. The positions are given in Gauss, the accuracy is ± 5 Gauss.

7.4. Experimental setup

This section will give an overview how to detect Feshbach resonances. This is currently being prepared in our experimental setup.

The easiest way to detect magnetic Feshbach resonances is to take advantage of their feature of the pole in the scattering length. A very large scattering length is typically accompanied by a large three-body loss coefficient leading to an increased atom loss in the trap. Therefore, whenever the magnetic field is close to the Feshbach resonance, the atoms will be lost much faster from the trap [109].

7.4.1. Magnetic field

For the use of Feshbach resonance, it is required to have a homogeneous magnetic field in the region of the trap. In the current setup of our experiment, a (nearly) homogeneous magnetic field required for Feshbach resonance experiments can be applied using the coils for the magnetic trap and the magneto-optical trap. For trapping purposes, these coils are producing a quadrupole field, but by switching the polarity of two of the coils, a (nearly) homogeneous field can be achieved (see chap. 3.1). The magnetic field at the trap position needs to be calibrated. The easiest way to do this, is to use known magnetic Feshbach resonances in Rb.

7.4.2. Magnetic Feshbach resonances in Rb

Magnetic Feshbach resonances in ^{87}Rb were measured precisely in 2002 by Marte et al.[112]. The experiment was performed in an optical dipole trap with about $4 \cdot 10^6$ atoms prepared in the $|F = 1, m_F = 1\rangle$ state. Note, that this state is not trappable in a magnetic trap. The atom cloud had a temperature of 2 μK, corresponding to a peak density of $2 \cdot 10^{14}$ cm^{-3}. The magnetic field was turned on at a fixed value for typically 50 ms. The broadest found resonances are listed in tab. 7.5.

$B_{\mathrm{exp}}(G)$	depth (%)	Δ (mG)
391.49	63	0.3
406.23	57	0.4
551.47	66	0.2
632.45	77	1.5
685.43	78	17
719.48	77	0.5
831.29	67	0.2
911.74	72	1.3
1007.34	64	170

Table 7.5.: *The broadest Feshbach resonances found in ^{87}Rb in state $|1, 1\rangle$. From [112]*

In ^{85}Rb, Feshbach resonances were also measured, e.g. in [113]. Three Feshbach resonances in the substate $|F = 2, m_F = -2\rangle$ were found:

- $B = 155.041$ G with a width of $\Delta = 10.709$ G [113]
- $B = 220$ G [114]
- $B = 850$ G [115]

7.4.3. Experimental Detection of Feshbach resonances in ^{87}Rb

In ongoing experiments, we observed Feshbach resonances in homonuclear ^{87}Rb by using trap-loss techniques as discussed above. This information is used to calibrate the magnetic field. To investigate the Feshbach resonances, we need to have the atoms in a pure optical trap. After applying the magnetic Feshbach field, the atom number is reduced at te Feshbach resonance.

In order to achieve this, the Rb atoms were transferred from the MOT into a magnetic trap, where $2 \cdot 10^8$ atoms at a temperature of about $150\,\mu$K are trapped. With evaporative cooling, the temperature is decreased to about $10\,\mu$K. The atom number drops at the same time to about $2 \cdot 10^6$ atoms. Subsequently, an infrared laser at 1064 nm with its focus at the center of the magnetic trap is turned on. The atoms are then transferred into the optical trap and the magnetic trap can be switched off. The Feshbach fields are turned on for 1 second. After that, the magnetic fields and the trapping light are turned off and a picture of the atoms after a short time of flight is taken and the atom number is determined. Due to the dramatically change of the s-wave scattering length, the three-body-losses are enhanced near the Feshbach resonance and the atoms are lost from the trap.

Fig. 7.7 shows the first observation of two Feshbach resonances in our experiment. The atom number drops significantly at the resonances at 685 Gauss and 632 Gauss.

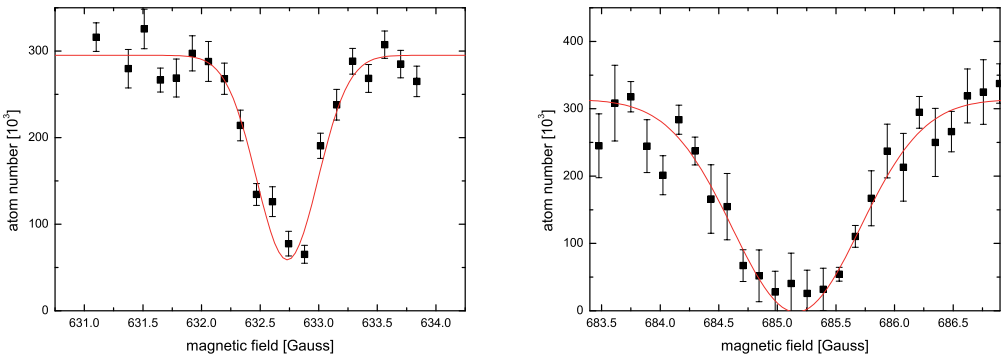

Figure 7.7.: *Our first experimental measured Feshbach resonances in ^{87}Rb at 632 G and 685 G. These two resonances were used to calibrate the magnetic field.*

The position of the resonance helped us to calibrate the magnetic field of the trap with

respect to the current in the coils to

$$B(I)\,[\text{Gauss}] = 2.735 \cdot I\,[\text{Ampere}]. \tag{7.6}$$

The observed loss features which are related to the Feshbach resonances appear much broader than the theoretical elastic width of 17 mG respective 1.5 mG [112]. From the theoretical predictions for LiYb [9] and RbSr [8], we expect elastic widths for the YbRb Feshbach resonances of the same magnitude. Therefore we are confident that our current experimental setup is capable of observing heteronuclear Feshbach resonances.

8.

Future experiments and outlook

This chapter describes the next steps that are required for the creation of ground state YbRb molecules. A two-step procedure appears to be the most promising route: In the first step, ground state molecules in a high vibrational level will be created. This can be done either by a 2-Photon step similar to the 2-Photon-Photoassociation experiments or with the help of magnetic Feshbach resonances as discussed in the previous chapter. The next step will be the transfer from the highly vibrating ground state to the rovibrational ground state. Another 2-Photon process will be the obvious choice. Techniques and possible transitions will be provided.

8.1. Vibrationally excited ground state molecules

To create YbRb molecules in the absolute ground state, two steps will be needed: In a first step, two free atoms have to be associated to molecules in a highlying vibrational level of the ground state. For this step, two possibilities exist: It is possible to use magnetic Feshbach resonances or to use a 2-Photon transition with an auxiliary electronically excited molecular level.

8.1.1. Feshbach molecules

Most common is the use of magnetic field ramps or the application of oscillatory fields [109] to associate two free atoms to a molecule in a highly excited vibrational state. Other possibilities for magnetic association will most likely not be used in our experiment and will not be discussed here. A magnetic ramp for creating Feshbach molecules was proposed in [116, 117, 118]. In a simple picture, the coupling between the open channel and the closed channel leads to a mixing of these states. This can be used to adiabatically convert the free atoms to molecules. At the beginning of the ramp, a magnetic field B is applied with $B > B_0$ where B_0 denotes the Feshbach resonance. This field is then ramped to a value below the Feshbach resonance to associate Feshbach molecules. This is shown in fig. 8.1.

In [119], the first reported creation of Feshbach molecules by a magnetic ramp was reported. The group at JILA created molecules with fermionic ^{40}K at a temperature of 150 nK by using the resonance at 224.2 Gauss with a width of 0.21 G. The magnetic field was ramped from 227.8 G at a rate of 40 μsG^{-1} across the resonance to 216.2 G. After this ramp, the (remaining) atom number was measured and was found to be smaller than

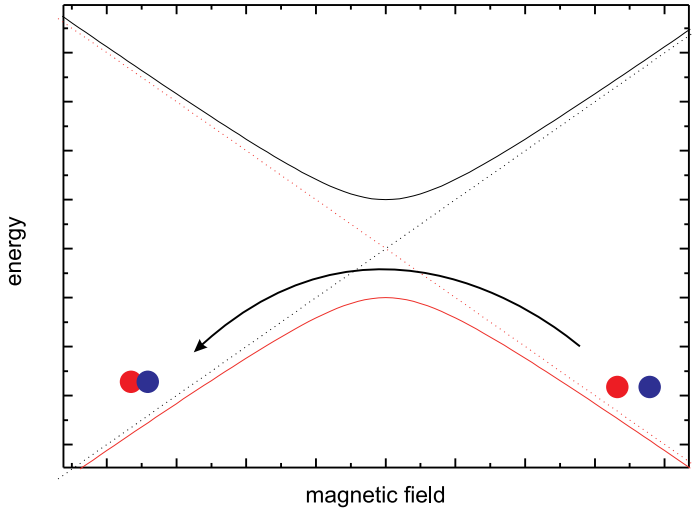

Figure 8.1.: *Simplified picture of creating molecules by a magnetic ramp: A magnetic field higher than the Feshbach resonance is applied to two free atoms (right side of the picture) and slowly ramped over the resonance. The red dotted line shows the energy level of free atoms without disturbance and the black dotted curve of a molecular level without disturbance. The solid black and red curve show the real potential curves with coupling of the two states leading to a mixing where the atoms can be converted adiabatically to molecules (left side).*

explainable by inelastic collisions. When the process of creating molecules was reversed by applying the magnetic ramp in reverse direction, the atoms returned. This could only be explained by a back conversion of the molecules to atoms. With this method, about 50 % of the atoms were converted to molecules. In more recent experiments, e.g. in [120], higher conversion efficiencies of up to 80 % were reported.

Some possibilities to create YbRb molecules with the help of Feshbach resonances were described in chapter 7. The most promising resonances produce molecules in the vibrational level $\Delta v = -2$ or $\Delta v = -3$ in ^{85}Rb or $\Delta v = -4$ in ^{87}Rb mixtures.

The use of an oscillatory field is another method of producing Feshbach molecules, first reported in [121, 122]. In [121], a BEC of ^{85}Rb atoms at a magnetic field of 162 G is created. Then, the magnetic field is ramped in 5 ms to values between 156 and 157 G near the Feshbach resonance at 155.0 G (width 11 G). A sinusoidally oscillating magnetic field with peak-to-peak amplitudes of 130-280 mG was added for up to 50 ms with a frequency close to the molecular binding energy. After that, the magnetic field is ramped back to 162 G and after some decay time in which the molecules decay and leave the trap, the atom number is measured. With this method, efficiencies of 55 % have been reported. A radio-frequency transition in the range of tens of MHz can also be applied instead of an oscillating magnetic field, reported e.g. in [123].

In the mixture of ^{174}Yb and ^{85}Rb, this method could be used to associate molecules in the $m_F = -1$ substate at 361 G: At this magnetic field, the energy of the atomic level

is near the molecular level with an energy difference of about 3 MHz where a transition could be induced by a radio frequency. This would produce Feshbach molecules in the vibrational level $\Delta v = -2$.

8.1.2. Molecule creation by photoassociation

The other possibility to create molecules is to use electronic transitions. The most straightforward way is to associate two free atoms to molecules via 1-Photon-Photoassociation. This excited molecule then decays to either two free atoms or to a ground state molecule. The problem is, that with this method, the molecules will be distributed over many vibrational states and not, as desired, in a specific one. However, from the determined Franck-Condon factors (see chapter 5.6.2 and 6.2) we may deduce that for carefully chosen excited states the transfer into a specific vibrational level can exceed 25 %.

Stimulated Raman Adiabatic Passage (STIRAP) [124] is the most efficient way to transfer atoms or molecules in a state $|1\rangle$ to another state $|3\rangle$. This process uses an auxiliary state $|2\rangle$ and two lasers. The "Pump laser" is resonant with the transition $|1\rangle \rightarrow |2\rangle$ and the "Stokes laser" is resonant with $|3\rangle \rightarrow |2\rangle$. A sketch of this situation is shown on the left side of fig. 8.2.

If we now consider the interaction of a light field to these three states, in analogy to the case of two states as discussed in chap. 5.2, we get [30]:

$$\begin{aligned} \dot{c}_1(t) &= i\frac{\Omega_\mathrm{p}}{2}c_2(t) \\ \dot{c}_2(t) &= i\frac{\Omega_\mathrm{p}}{2}c_1(t) + i\frac{\Omega_\mathrm{s}}{2}c_3(t) \\ \dot{c}_3(t) &= i\frac{\Omega_\mathrm{s}}{2}c_2(t) \end{aligned} \tag{8.1}$$

with Ω_p is the Rabi frequency of the Pump laser and Ω_s is the Rabi frequency of the Stokes laser. The two lasers are considered here to be on resonance. Since in our discussion, the state $|2\rangle$ is the only state that allows spontaneous emission, it is desirable to avoid population of this state. This can be reached by the control of the Rabi frequencies Ω_p and Ω_s, if we assume

$$\begin{aligned} \Omega_p &= \Omega_0(t)c_3(t) \\ \Omega_s &= -\Omega_0(t)c_1(t). \end{aligned} \tag{8.2}$$

This leads to $\dot{c}_2(t) = 0$. This means that this state will never be populated. A sketch of the needed Rabi frequencies is shown on the right side of fig. 8.2 together with the populations of the 3 states.

For a good transfer efficiency, it is essential, that the two Rabi frequencies Ω_p and Ω_s have approximately the same value at their maximum. This can be reached by adjusting the power ratios of the two laser beams since the Rabi frequency depends on the squareroot of the intensity. For transitions from unbound atoms to bound molecules, this will be very

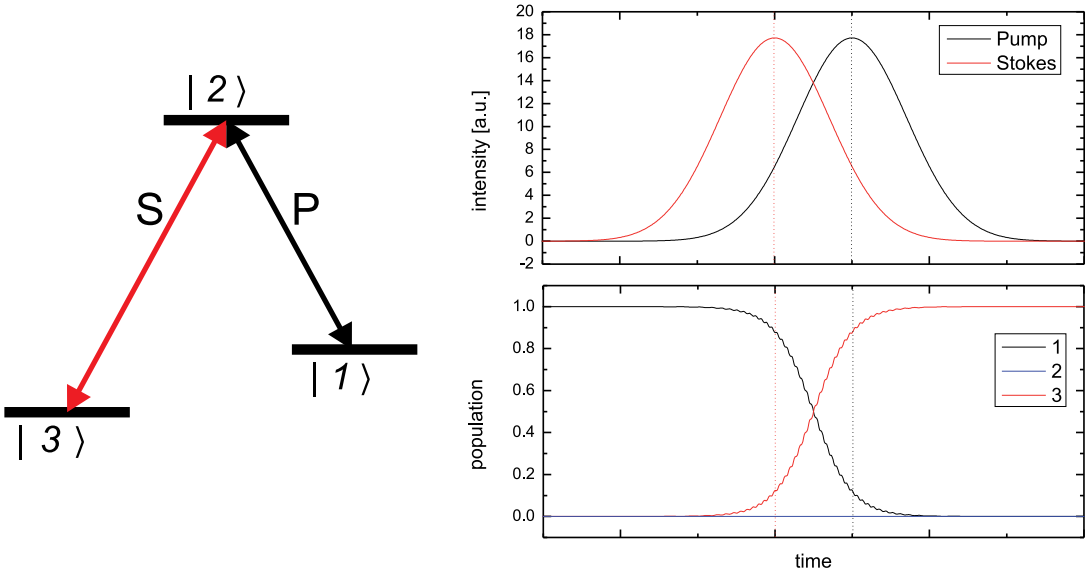

Figure 8.2.: *STIRAP principle. At the beginning, all atoms are in state* $|1\rangle$*. During the transfer to state* $|3\rangle$*, the state* $|2\rangle$ *will not be populated.*

challenging experimentally: In mixtures of Yb and Rb, the Rabi frequency for the pump laser is reported to be in the regime of a few Hz [3]. If the density of the atom cloud can be increased, it may be possible to reach Rabi frequencies in the range of a few kHz. On the other side, the Rabi frequency for the Stokes laser reaches up to 100 MHz (see chapter 6) which may be lowered to 1 MHz with low intensity. But nevertheless, the pump laser needs to be 10^6 times more intense than the Stokes laser to reach similar Rabi frequencies. This is the reason, why the STIRAP process from unbound atoms to bound molecules has not been reported yet.

For a mixture of ^{176}Yb^{87}Rb, there are two possibilities for a STIRAP process which are considerable: The first laser excites the $\Delta v' = -9$ level and the second laser is resonant to the level with the highest overlap, namely the $\Delta v = -5$ level. The other path is the first laser excites to the $\Delta v' = -11$ level and the second laser decays to the $\Delta v = -6$ level.

If this is possible, we would end up with ^{176}Yb^{87}Rb molecules in the $\Delta v = -4$ ground state via Feshbach resonances or in the $\Delta v = -5$ or $\Delta v = -6$ vibrational state via a STIRAP process. For the other isotopes, the result is similar.

8.2. Molecules in rovibrational ground state

The next step is to transfer weakly bound molecules to the rovibrational ground state. Here, a STIRAP process is needed. This technique is used in many experiments successfully, e.g. in ^{40}K^{87}Rb [34] where Feshbach molecules are converted to the absolute ground state with a STIRAP process with an efficiency of more than 50 %. In [33], an efficiency of more than 80 % was reported in conversion of Cs_2 Feshbach molecules to a deeply bound vibrational

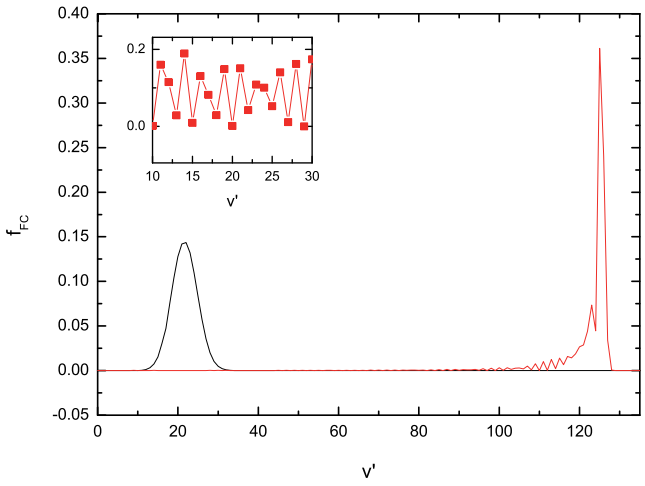

Figure 8.3.: *Calculated Franck-Condon factors of the rovibrational ground state $v = 0$ (black) and the highly vibrational state $\Delta v = -6$ (red) to vibrational level of the excited state $^2\Pi_{1/2}$. The inset shows the Franck-Condon factors of the highly vibrational state in the region near $v = 21$. Here, the Franck-Condon factors are multiplied with a factor of 10^3. The line is only a guideline for the eye.*

level.

For YbRb molecules, no experimental data for deeply bound vibrational level is available. Therefore, we can only use the ab-initio calculations [55] and the calculations performed in chapter 5.8, where the ground state potential was calculated. For the excited state $^2\Pi_{1/2}$, we know the C_6 value from the 1-Photon-PA experiments and a C_{12} value can in principle be calculated with the same methods as was done for the ground state. This was done leading to values of

$$\begin{aligned} C_6 &= -5684\,\mathrm{E_h a_0^6}, \\ C_{12} &= 2.28105 \cdot 10^8\,\mathrm{E_h a_0^{12}}. \end{aligned} \tag{8.3}$$

This potential has a potential depth of $V'_{\mathrm{min}} \approx -7700\,\mathrm{cm}^{-1}$ similar to the depth calculated in [55]. The known highlying vibrational levels are reproduced approximately. This needs more verification. Therefore, the following calculations will only give a hint where to search for deeply bound vibrational levels. With the help of a Mathematica script [108], the overlap of the wavefunctions from the vibrational levels of the ground state and the excited state was calculated.

In fig. 8.3, the calculated Franck-Condon factors for transitions from the rovibrational ground state (black) and the $\Delta v = -6$ ground state (red) to a vibrational level of the excited $^2\Pi_{1/2}$ state. It is clearly visible, that the ground state has a good overlap with vibrational levels near $v' = 21$ of the excited state while the highly vibrational level has a good overlap with states near $v' = 130$. For the STIRAP process, a good overlap with one

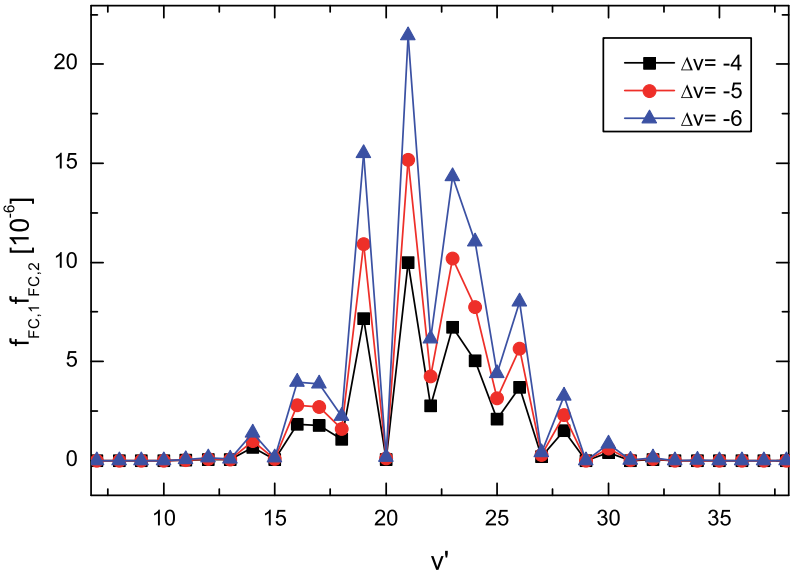

Figure 8.4.: *The Franck-Condon overlap between the rovibrational ground state $v = 0$ and a highly vibrational state Δv. Given is the product of the Franck-Condon factors against the vibrational state v' of the excited state $^2\Pi_{1/2}$. It is interesting to note, that indepedent from the highly vibrating state, the $v' = 21$ state is always favorable.*

excited state with both ground states is needed. Fig. 8.4 shows the product of the two Franck-Condon factors $|\langle v = 0|v'\rangle|^2 \cdot |\langle \Delta v|v'\rangle|^2$.

It is interesting to note, that for each of the three possible vibrational levels to start with, it is always the $v' = 21$ excited level that has the best overlap to both states. For the given potentials, this means, that the following wavelengths are needed for the STIRAP process:

$$\begin{aligned} \lambda_1 &= 1275\,\text{nm} \\ \lambda_2 &= 1525\,\text{nm} \end{aligned} \tag{8.4}$$

The wavelength λ_1 depends on the highly vibrating molecule that needs to be created in the first step. It has to be noted that these calculations rely on the shape and the depth of the involved potentials. The calculated ground state potential reproduces the measured vibrational levels well, but it is not known if this is still true for the deeply bound vibrational levels. The same argument holds for the excited state potential which even does not reproduce the already known vibrational levels within the accuracy. For more exact calculations, more experimental data is needed. This has to be seen as a hint where to search for resonances.

Ab-initio calculations[55] discussed the possibility to use a two-step STIRAP with the second step starting from a highly vibrating ground state and using the excited state $^2\Pi_{1/2}$

with wavelengths of

$$\begin{aligned} \lambda_1 &= 1345\,\mathrm{nm}, \\ \lambda_2 &= 1514\,\mathrm{nm}. \end{aligned} \tag{8.5}$$

Here, the intermediate vibrational level $v = 24$ is used with a Franck-Condon overlap of $3.1 \cdot 10^{-6}$.

For more exact values for the Franck-Condon overlap and for the positions of the vibrational levels, more experimental input is needed. First experiments in this direction may be done in molecular spectroscopy [125], which will hopefully give more information about the structure of the YbRb molecule and will help to reach the absolute ground state in this molecule.

A.

Potentials of the YbRb molecule

In this chapter, an overview over calculated potentials of the YbRb molecule will be given. Ab-initio calculations were performed in [55]. With the 1-Photon-Photoassociation, additional information about the excited state $^2\Pi_{1/2}$ state are available. We performed 2-Photon-Photoassociation spectroscopy on the ground state $^1\Sigma_{1/2}$.

A.1. Ground state $^2\Sigma_{1/2}$

With the help of the experimentally determined vibrational states of the YbRb ground state, it was possible to calculate the potential and with this, all vibrational levels of the ground state.

In the approximation of a Lennard-Jones potential, the potential is given by

$$V(r) = C_{12}/r^{12} + C_6/r^6 \tag{A.1}$$

with the coefficients

$$\begin{aligned} C_6 &= -(2563 \pm 50)\ \mathrm{E_h a_0^6}, \\ C_{12} &= 2.7412 \cdot 10^8\ \mathrm{E_h a_0^{12}} \end{aligned} \tag{A.2}$$

This potential holds 66 vibrational levels for ^{174}Yb^{87}Rb and ^{176}Yb^{87}Rb and 65 levels for the other combinations. The binding energies for the vibrational levels for ^{176}Yb^{87}Rb are listed in tab. A.1.

The s-wave scattering lengths for all isotopic combinations of Rb and Yb as derived from this potential are listed in tab. A.2

vib. state	Δ_{bind} in cm^{-1}	vib. state	Δ_{bind} in cm^{-1}	vib. state	Δ_{bind} in cm^{-1}
1	-1286.4	23	-391.68	45	-48.212
2	-1230.8	24	-365.83	46	-41.779
3	-1176.7	25	-341.10	47	-35.939
4	-1124.0	26	-317.49	48	-30.665
5	-1073.0	27	-294.95	49	-25.929
6	-1023.4	28	-273.48	50	-21.703
7	-975.29	29	-253.05	51	-17.961
8	-928.65	30	-233.63	52	-14.672
9	-883.45	31	-215.20	53	-11.809
10	-839.68	32	-197.75	54	-9.3432
11	-797.32	33	-181.25	55	-7.2454
12	-756.35	34	-165.66	56	-5.4866
13	-716.74	35	-150.98	57	-4.0373
14	-678.48	36	-137.17	58	-2.8681
15	-641.56	37	-124.22	59	-1.9492
16	-605.94	38	-112.09	60	-1.2508
17	-571.62	39	-100.76	61	-0.7427
18	-538.57	40	-90.212	62	-0.3949
19	-506.77	41	-80.413	63	-0.1771
20	-476.20	42	-71.340	64	-0.0590
21	-446.84	43	-62.966	65	-0.0102
22	-418.67	44	-55.266	66	-1.6 MHz

Table A.1.: *Vibrational levels for $^{176}Yb^{87}Rb$ calculated with a $C_6 = -2563\,\text{E}_\text{h}\text{a}_0^6$ and $C_{12} = 2.7412 \cdot 10^8\,\text{E}_\text{h}\text{a}_0^{12}$(see chapter 5.8)*

	^{168}Yb	^{170}Yb	^{171}Yb	^{172}Yb	^{173}Yb	^{174}Yb	^{176}Yb
^{85}Rb	240	141	118	100	85	71	41
^{87}Rb	41	-5	-47	-131	-431	1398	225

Table A.2.: *S-wave scattering lengths for all isotopic combinations of Yb and Rb. The lengths are given in bohr radii.*

A.2. The excited state $^2\Pi_{1/2}$

In the limiting case of separated atoms, this state will asymptotically connect to the excited $^2P_{1/2}$ state of Rb and the ground state $^1S_0$ of Ytterbium. This state was first photoassociated in our experiment in 2009 [3]. This data was used to determine a C_6 value of

$$C_6 = -(5684 \pm 98)\,\mathrm{E_h a_0^6} \tag{A.3}$$

In ab-initio calculations [55], a Morse potential

$$V(r) = E_D \cdot \left(1 - e^{-\omega_r (r - R_e)}\right)^2 \tag{A.4}$$

was calculated with

$$\begin{aligned} E_D &= 7735\,\mathrm{cm}^{-1} \\ R_e &= 7.40 a_0 \\ \omega_r &= 69.294\,\mathrm{cm}^{-1} \end{aligned} \tag{A.5}$$

for this state. In the calculations performed in chapter 8, a Lennard-Jones potential with approximately the same potential depth was introduced which reproduces the known vibrational states approximately. More input is needed here. The C_{12} value was calculated to

$$C_{12} = 2.28105 \cdot 10^8\,\mathrm{E_h a_0^{12}}. \tag{A.6}$$

This has to be seen as a toy potential for calculating Frank-Condon factors (see chap. A.4) to try to get a hint for finding the deeply bound vibrational levels.

A.3. The excited states $^2\Pi_{3/2}$ and $^2\Sigma_{1/2}$

The asymptotic case of these two potentials is the $^2P_{3/2}$ state of Rb and the $^1S_0$ ground state of Yb. We tried some photoassociation experiments on this transition, but there is not sufficient data to calculate a potential for that. But, ab-initio calculations were done by Sørensen [55]. They approximated the potential by a Morse potential with

$$\begin{aligned} E_D &= 7164\,\mathrm{cm}^{-1} \\ R_e &= 7.43 a_0 \\ \omega_r &= 69.322\,\mathrm{cm}^{-1} \end{aligned} \tag{A.7}$$

for the $^2\Pi_{3/2}$ state and

$$\begin{aligned} E_D &= 4423\,\mathrm{cm}^{-1} \\ R_e &= 8.43 a_0 \\ \omega_r &= 52.789\,\mathrm{cm}^{-1} \end{aligned} \tag{A.8}$$

for the $^2\Sigma_{1/2}$ state.

A.4. Franck-Condon factors

The Franck-Condon factors have been calculated for the ground state $^2\Sigma_{1/2}$ and the vibrational levels calculated by the toy potential for the excited state $^2\Pi_{1/2}$. The Franck-Condon matrix is shown in fig. A.1.

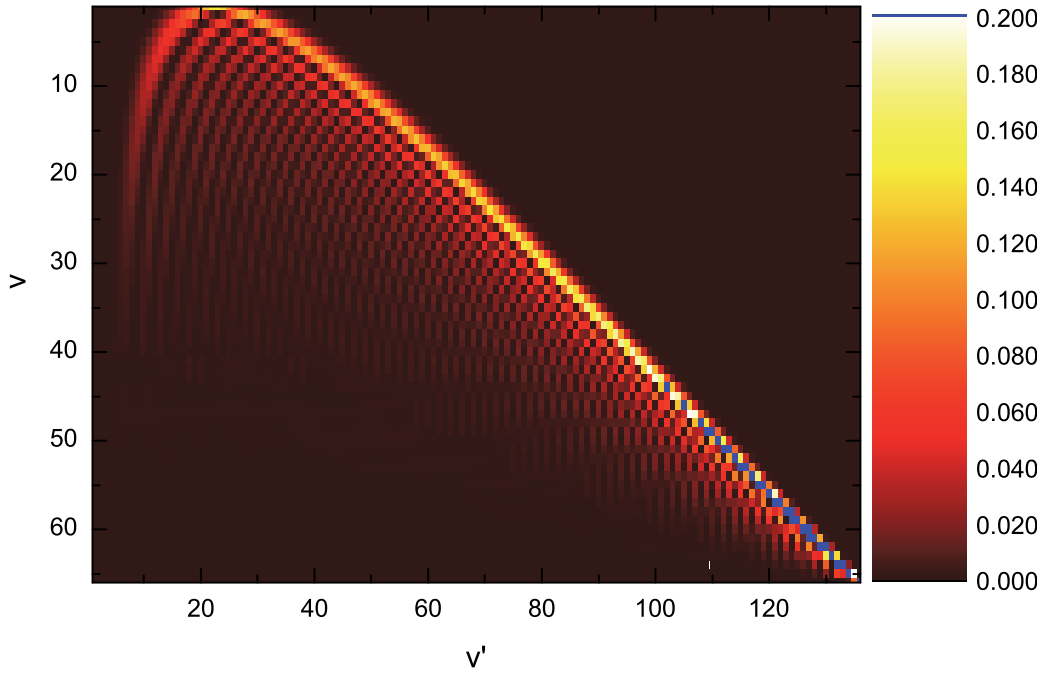

Figure A.1.: *Franck-Condon matrix of the ground state $^2\Sigma_{1/2}$ (Y axis) and the excited state $^2\Pi_{1/2}$ (X axis).*

B.

The Li-Yb experiment in Seattle

In 2010, I visited the group of Prof. Gupta in Seattle, Washington, USA for 5 months. The experiment there deals with a mixture of Lithium and Ytterbium and is thus closely related to the work performed at the university in Düsseldorf. The two species are cooled to ultracold temperatures by laser cooling. During my time there, we prepared the atoms in a optical dipole trap and examined the scattering properties to each other. With these experiments, it was possible to determine the interspecies s-wave scattering length to $|a_{^6\mathrm{Li}-^{174}\mathrm{Yb}}| = (13 \pm 3)\, a_0$. *In the next step, the mixture of Li and Yb will be used to create LiYb molecule in a similar way as discussed in this thesis with YbRb.*

In this chapter, I explain the main features of the experiment and the results we got during my time there.

B.1. The experiment

In the experiment in Seattle, Lithium and Ytterbium are cooled each with its own Zeeman slower. Fig. B.1 shows a sketch of the chamber. All cooling and imaging of Li is performed on the $|^2S_{1/2}\rangle \rightarrow |^2P_{3/2}\rangle$ transition at 671 nm. A tapered amplifier is used to providing the light for trapping and imaging Li atoms. For slowing, an injection-seeded diode laser, similar to our setup for Rb, is used.

For slowing and imaging of Yb, a frequency-doubled Titan:Sapphire laser[1] with an output wavelength of 399 nm (transition $|^1S_0\rangle \rightarrow |^1P_1\rangle$) is used. For trapping, a frequency-doubled fiber laser is used wich produces light at the intercombination line $|^1S_0\rangle \rightarrow |^3P_1\rangle$ at 556 nm. This scheme is nearly the same as our scheme for trapping Yb. All lasers are locked using saturated absorption spectroscopy schemes.

A typical experimental scheme is working as follows: At first, Yb is laser cooled and trapped in a MOT. After some time of loading, the Li is cooled and loaded into the same MOT. During a varying (short) loading time, an optical dipole trap (ODT) consisting of one (or two overlapping) laser beams from a linearly polarized fiber laser at 1064 nm is switched on and the atoms are transferred to this trap. During the loading time of Li, the Yb MOT is compressed due to the different magnetic field gradients which are required for the operation of Yb and Li MOTs respectively. In this time, the MOT loses Yb atoms,

[1] In 2011, this laser is replaced by a frequency-doubled tapered amplifier setup.

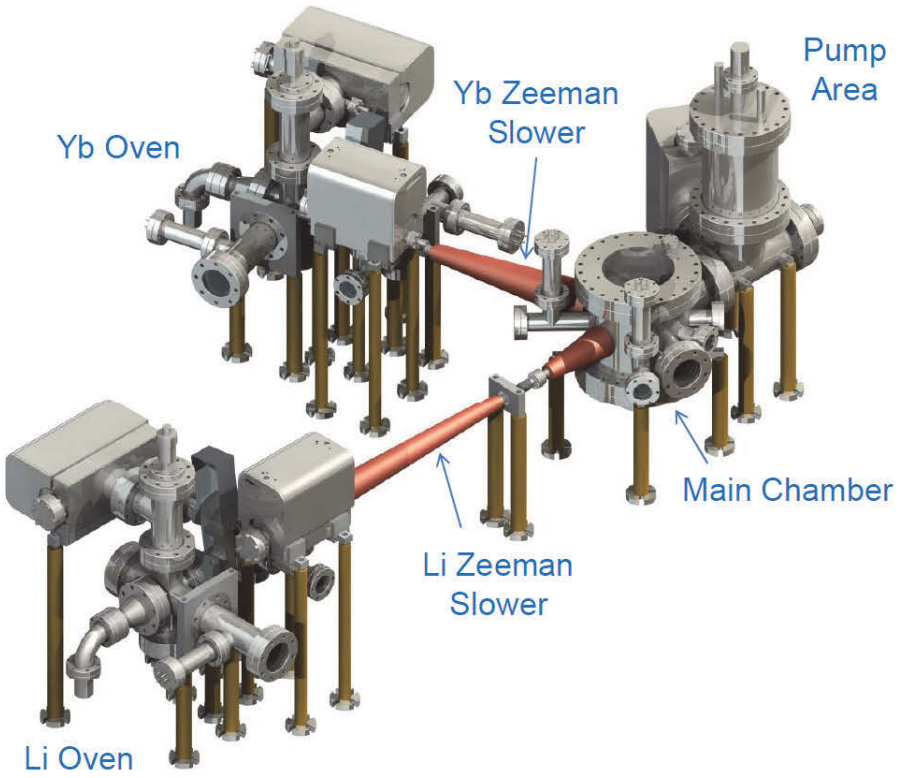

Figure B.1.: *Sketch of the vacuum chamber of the Li-Yb experiment. From [126].*

but gain Li atoms. This is shown in fig. B.2. By this, it is possible to adjust the atom number ratio of the two species.

B.2. Sympathetic cooling

For the thermalization measurements, a single beam ODT with a $1/e^2$ radius of 30 μm is used. ^{174}Yb is transferred with a temperature of about 30 μK to the ODT at a calculated trap depth of $U_{\mathrm{Yb}} = 220\,\mu\mathrm{K}$. The depth is increased during the loading time of ^{6}Li to a depth of $U_{\mathrm{Yb}} = 500\,\mu\mathrm{K}$. Due to the wavelength of 1064 nm of the dipole trap laser, the trap is deeper for Li ($U_{\mathrm{Li}} = 1.1\,\mathrm{mK}$). This leads to a trap geometry which is perfectly suited for thermalization measurements where the cold Yb atoms cool down Li atoms. The measurements were performed with a near-zero magnetic field.

The atom numbers are observed via absorption imaging on different parts of the same CCD camera. After a varying waiting time in the ODT, we measured the atom number and the temperature of the two species, either in separate single-species experiments or

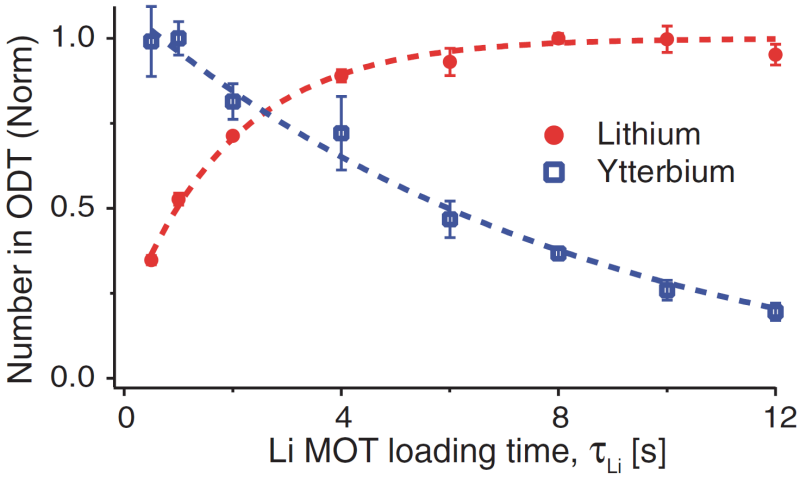

Figure B.2.: *Atom number during loading of Li. Due to the compression of the MOT, Yb atoms are lost from the MOT while Li loads. This can be used to tune the ratio of the two atom species. From [11]*

when they are brought in thermal contact. The initial temperatures are

$$\begin{aligned} T_{\mathrm{Yb}} &= 35\,\mu\mathrm{K}, \\ T_{\mathrm{Li}} &= 110\,\mu\mathrm{K}. \end{aligned} \tag{B.1}$$

The atom numbers are $N_{\mathrm{Yb}} = 1.1 \cdot 10^6$ and $N_{\mathrm{Li}} = 1.4 \cdot 10^5$ at the beginning of the measurements in the ODT. For each species for itself, the temperature in the ODT is not changing within the lifetime of about 30 s. When both species are loaded, the Li atoms are getting colder without losing atoms and reach the temperature of the Yb cloud in about 5 s. The Yb temperature does not significantly change due to the much higher atom number, see fig. B.3.

In the analysis of the data, we assumed pure s-wave scattering which is justified in this temperature regime since the calculated p-wave threshold is 2.5 mK [11]. The thermalization rate γ_{th} can be calculated as

$$\gamma_{\mathrm{th}} = -\frac{1}{\Delta T}\frac{d(\Delta T)}{dt} = \frac{\xi}{\alpha}\bar{n}\sigma_{\mathrm{LiYb}}\bar{v}. \tag{B.2}$$

Here, $\alpha = 2.7$ is the average number of collisions needed for thermalization for equal masses and $\xi = \frac{4m_{\mathrm{Li}}m_{\mathrm{Yb}}}{(m_{\mathrm{Li}}+m_{\mathrm{Yb}})^2} = 0.13$ is the mass correction factor [127], ΔT is the temperature difference between Li and Yb,

$$\bar{v} = \sqrt{\frac{8k_B}{\pi}\left(\frac{T_{\mathrm{Li}}}{m_{\mathrm{Li}}} + \frac{T_{\mathrm{Yb}}}{m_{\mathrm{Yb}}}\right)} \tag{B.3}$$

is the mean relative velocity and $\bar{n} = \left(\frac{1}{N_{\mathrm{Li}}} + \frac{1}{N_{\mathrm{Yb}}}\right)\int n_{\mathrm{Li}}n_{\mathrm{Yb}}d^3r$ is the overlap density. The s-wave cross section can be calculated as

$$\sigma_{\mathrm{LiYb}} = \frac{2\pi a^2}{\left(1 - \frac{1}{2}k^2 r_e a\right)^2 + k^2 + a^2} \tag{B.4}$$

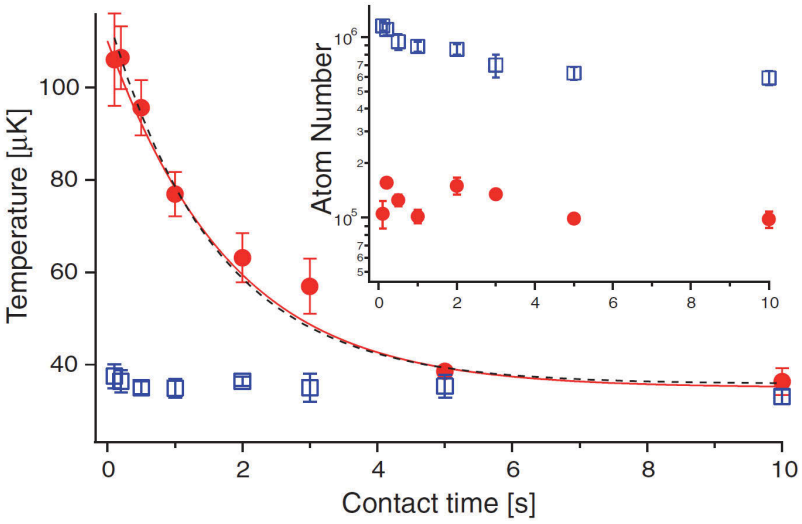

Figure B.3.: *Thermalization measurements of a mixture of ^{174}Yb (blue) and ^{6}Li (red). The red solid line is the result of the thermalization model with a scattering length of $|a_{^6\mathrm{Li}-^{174}\mathrm{Yb}}| = (13 \pm 3)\, a_0$. The inset shows the atom number of the two species. From [11].*

including an energy dependence [128] where $\hbar k$ is the relative momentum and r_e is the effective range. The numbers for $\bar{n}$ and $\bar{v}$ change with the temperature of Li, therefore a numerical procedure was used for modeling the thermalization process. In fig. B.3, the result of this numerical calculation is shown in the red solid line.

From the numerical simulation, a s-wave scattering length of

$$|a_{^6\mathrm{Li}^{174}\mathrm{Yb}}| = (13 \pm 3)\, a_0 \tag{B.5}$$

is obtained with a_0 being the Bohr radius. Recent measurements by another group [129] give similar results for this value of $|a| = 18.9 \pm 3.8 a_0$.

B.3. Outlook

This technique was expanded to forced evaporative sympathetic cooling [130]. The ODT beam was expanded to a crossed dipole trap by adding a second beam that intersects the first beam at an angle of 10°. By lowering the trap depth, the Yb atoms get cooled evaporatively. Since the trap depth for Li atoms is much higher, this species is not cooled evaporatively but sympathetically by collisions with the Yb atoms.

In the experiment, bosonic ^{174}Yb atoms and fermionic ^{6}Li atoms were both loaded as described before from the MOT phase into the optical trap and after an evaporation time of about 12 s, an Yb Bose-Einstein condensate was created and the Li atoms were below the Fermi temperature. By this, simultaneous quantum degeneracy was achieved.

In the next steps, this mixture will be used to search for magnetic Feshbach resonances as proposed in [9] and photoassociation experiments as described in this work will be

performed to learn more about the potential of the LiYb molecule.

Bibliography

[1] A. Batär, *Erzeugung und Charakterisierung ultrakalter Rubidium- und Ytterbiumatome – auf dem Weg zu einem gemischten Quantengas*, Dissertation, Universität Düsseldorf (2005).

[2] S. Tassy, *Sympathetische Kühlung von Ytterbium mit Rubidium*, Ph.D. thesis, Universität Düsseldorf (2007).

[3] N. Nemitz, *Production and spectroscopy of ultracold YbRb* molecules*, Dissertation, Universität Düsseldorf (2008).

[4] F. Baumer, *Isotope dependent interactions in a mixture of ultracold atoms*, Dissertation, Universität Düsseldorf (2010).

[5] F. Münchow, *Photoassoziationsspektroskopie an einem ultrakalten RbYb-Gemisch*, Diplomarbeit, Universität Düsseldorf (2008).

[6] R. J. LeRoy and R. B. Bernstein, *Dissociation Energy and Long-Range Potential of Diatomic Molecules from Vibrational Spacings of Higher Levels*, J. Chem. Phys. **52**, 3869 (1970).

[7] F. Baumer, F. Münchow, A. Görlitz, S. E. Maxwell, P. S. Julienne, and E. Tiesinga, *Spatial separation in a thermal mixture of ultracold ^{174}Yb and ^{87}Rb atoms*, Phys. Rev. A **83**, 040702 (2011).

[8] P. S. Zuchowski, J. Aldegunde, and J. M. Hutson, *Ultracold RbSbr Molecules Can Be Formed by Magnetoassociation*, Phys. Rev. Lett. **105**, 153201 (2010).

[9] D. A. Brue and J. M. Hutson, *Magnetically Tunable Feshbach Resonances in Ultracold Li-Yb Mixtures*, Phys. Rev. Lett. **108**, 043201 (2012).

[10] S. Inouye, J. Goldwin, M. L. Olsen, C. Ticknor, J. L. Bohn, and D. S. Jin, *Observation of Heteronuclear Feshbach Resonances in a Mixture of Bosons and Fermions*, Phys. Rev. Lett. **93**, 183201 (2004).

[11] V. V. Ivanov, A. Khramov, A. H. Hansen, W. H. Dowd, F. Münchow, A. O. Jamison, and S. Gupta, *Sympathetic Cooling in an Optically Trapped Mixture of Alkali and Spin-Singlet Atoms*, Phys. Rev. Lett. **106**, 153201 (2011).

[12] J. V. Prodan, W. D. Phillips, and H. Metcalf, *Laser Production of a Very Slow Monoenergetic Atomic Beam*, Phys. Rev. Lett. **49**, 1149 (1982).

[13] W. Phillips and H. Metcalf, *Laser Deceleration of an Atomic Beam*, Phys. Rev. Lett. **48**, 596–599 (1982).

[14] W. D. Phillips, *Nobel Lecture: Laser cooling and trapping of neutral atoms*, Rev. Mod. Phys. **70**, 721– (1998).

[15] K. B. Davis, M.-O. Mewes, M. Joffe, M. R. Andrews, and W. Ketterle, *Evaporative Cooling of Sodium Atoms*, Phys. Rev. Lett. **74**, 5202 (1995).

[16] M. H. Anderson, J. R. Ensher, M. R. Matthews, C. E. Wieman, and E. A. Cornell, *Observation of Bose-Einstein-Condensation in a Dilute Atomic Vapor*, Science **269**, 198–201 (1995).

[17] K. B. Davis, M.-O. Mewes, M. R. Andrews, N. J. van Druten, D. S. Durfee, D. M. Kurn, and W. Ketterle, *Bose-Einstein Condensation in a Gas of Sodium Atoms*, Phys. Rev. Lett. **75**, 3969 (1995).

[18] C. C. Bradley, C. A. Sackett, J. J. Tollett, and R. G. Hulet, *Evidence of Bose-Einstein Condensation in an Atomic Gas with Attractive Interactions*, Phys. Rev. Lett. **75**, 1687 (1995).

[19] N. S. Bose, *Plancks Gesetz und Lichtquantenhypothese*, Zeitschrift für Physik **26**, 178 (1924).

[20] The Official Web Site of the Nobel Foundation, *The Nobel Prize in Physics 1997*, URL `http://nobelprize.org/nobel_prizes/physics/laureates/1997/index.html`.

[21] The Official Web Site of the Nobel Foundation, *The Nobel Prize in Physics 2001*, URL `http://nobelprize.org/nobel_prizes/physics/laureates/2001/index.html`.

[22] Y. Takasu, K. Maki, K. Komori, T. Takano, K. Honda, M. Kumakura, T. Yabuzaki, and Y. Takahashi, *Spin-Singlet Bose-Einstein Condensation of Two-Electron Atoms*, Phys. Rev. Lett. **91**, 040404 (2003).

[23] E. S. Shuman, J. F. Barry, D. R. Glenn, and D. DeMille, *Radiative Force from Optical Cycling on a Diatomic Molecule*, Phys. Rev. Lett. **103**, 223001 (2009).

[24] T. Köhler, K. Góral, and P. S. Julienne, *Production of cold molecules via magnetically tunable Feshbach resonances*, Rev. Mod. Phys. **78**, 1311– (2006).

[25] K. M. Jones, E. Tiesinga, P. D. Lett, and P. S. Julienne, *Ultracold photoassociation spectroscopy: Long-range molecules and atomic scattering*, Rev. Mod. Phys. **78**, 483–535 (2006).

[26] P. Courteille, R. S. Freeland, D. J. Heinzen, F. A. van Abeelen, and B. J. Verhaar, *Observation of a Feshbach Resonance in Cold Atom Scattering*, Phys. Rev. Lett. **81**, 69–72 (1998).

[27] S. Inouye, M. R. Andrews, J. Stenger, H.-J. Miesner, D. Stamper-Kurn, and W. Ketterle, *Observation of Feshbach Resonances in a Bose-Einstein Condensate*, Nature **392**, 151–154 (1998).

[28] C. A.Stan, M. W. Zwierlein, C. H. Schunck, S. M. F. Raupach, and W. Ketterle, *Observation of Feshbach Resonances between Two Different Atomic Species*, Phys. Rev. Lett. **93**, 143001 (2004).

[29] A. Fioretti, D. Comparat, A. Crubellier, O. Dulieu, F. Masnou-Seeuws, and P. Pillet, *Formation of Cold* Cs_2 *Molecules through Photoassociation*, Phys. Rev. Lett. **80**, 4402–4405 (1998).

[30] K. Bergmann, H. Theuer, and B. W. Shore, *Coherent population transfer among quantum states of atoms and molecules*, Rev. Mod. Phys. **70**, 1003– (1998).

[31] T. Rom, T. Best, O. Mandel, A. Widera, M. Greiner, T. W. Hänsch, and I. Bloch, *State Selective Production of Molecules in Optical Lattices*, Phys. Rev. Lett. **93**, 073002 (2004).

[32] F. Lang, K. Winkler, C. Strauss, R. Grimm, and J. H. Denschlag, *Ultracold Triplet Molecules in the Rovibrational Ground State*, Phys. Rev. Lett. **101**, 133005– (2008).

[33] J. G. Danzl, E. Haller, M. Gustavsson, M. J. Mark, R. Hart, N. Bouloufa, O. Dulieu, H. Ritsch, and H.-C. Nagerl, *Quantum Gas of Deeply Bound Ground State Molecules*, Science **321**, 1062–1066 (2008).

[34] K.-K. Ni, S. Ospelkaus, M. H. G. de Miranda, A. Pe'er, B. Neyenhuis, J. J. Zirbel, S. Kotochigova, P. S. Julienne, D. S. Jin, and J. Ye, *A High Phase-Space-Density Gas of Polar Molecules*, Science **322**, 231–235 (2008).

[35] A. J. Kerman, J. M. Sage, S. Sainis, T. Bergeman, and D. DeMille, *Production and State-Selective Detection of Ultracold RbCs Molecules*, Phys. Rev. Lett. **92**, 153001 (2004).

[36] J. M. Sage, S. Sainis, T. Bergeman, and D. DeMille, *Optical Production of Ultracold Polar Molecules*, Phys. Rev. Lett. **94**, 203001 (2005).

[37] J. Deiglmayr, A. Grochola, M. Repp, K. Mörtlbauer, C. Glück, J. Lange, O. Dulieu, R. Wester, and M. Weidemüller, *Formation of Ultracold Polar Molecules in the Rovibrational Ground State*, Phys. Rev. Lett. **101**, 133004 (2008).

[38] T. Lahaye, J. Metz, B. Fröhlich, T. Koch, M. Meister, A. Griesmaier, T. Pfau, H. Saito, Y. Kawaguchi, and M. Ueda, *d-Wave Collapse and Explosion of a Dipolar Bose-Einstein Condensate*, Phys. Rev. Lett. **101**, 080401– (2008).

[39] M. Lu, N. Q. Burdick, S. H. Youn, and B. L. Lev, *Strongly Dipolar Bose-Einstein Condensate of Dysprosium*, Phys. Rev. Lett. **107**, 190401 (2011).

[40] L. Santos, G. V. Shlyapnikov, P. Zoller, and M. Lewenstein, *Bose-Einstein Condensation in Trapped Dipolar Gases*, Phys. Rev. Lett. **85**, 1791 (2000).

[41] S. Ospelkaus, N. K.-K., M. H. G. de Miranda, B. Neyenhuis, D. Wang, S. Kotochigova, P. S. Julienne, D. S. Jin, and J. Ye, *Ultracold polar molecules near quantum degeneracy*, Faraday Discuss. **142**, 351 (2009).

[42] D. DeMille, *Quantum computation with trapped polar molecules*, Phys. Rev. Lett. **88**, 067901 (2002).

[43] A. André, D. DeMille, J. M. Doyle, M. D. Lukin, S. E. Maxwell, P. Rabl, R. J. Schoelkopf, and P. Zoller, *A coherent all-electrical interface between polar molecules and mesoscopic superconducting resonators*, Nature Physics **2**, 636 (2006).

[44] K. Góral, L. Santos, and M. Lewenstein, *Quantum Phases of Dipolar Bosons in Optical Lattices*, Phys. Rev. Lett. **88**, 170406 (2002).

[45] M. Baranov, L. Dobrek, K. Goral, L. Santos, and M. Lewenstein, *Ultracold dipolar gases – a challenge for experiments and theory*, Physica Scripta **T102**, 74–81 (2002).

[46] G. Pupillo, A. Micheli, H. P. Büchler, and P. Zoller, *Condensed Matter Physics with Cold Polar Molecules*, Preprint-Archiv arXiv: arXiv:0805.1896v1 (2008).

[47] R. V. Krems, *Molecules near absolute zero and external field control of atomic and molecular dynamics*, Internat. Rev. Phys. Chem. **24**, 99 (2005).

[48] J. J. Hudson, B. E. Sauer, M. R. Tarbutt, and E. A. Hinds, *Measurement of the Electron Electric Dipole Moment Using YbF Molecules*, Phys. Rev. Lett. **89**, 023003 (2002).

[49] M. R. Tarbutt, J. J. Hudson, B. E. Sauer, and E. A. Hinds, *Prospects for measuring the electric dipole moment of the electron using electrically trapped polar molecules*, Faraday Discuss. **142**, 37 (2009).

[50] E. R. Meyer and J. L. Bohn, *Electron electric-dipole-moment searches based on alkali-metal- or alkaline-earth-metal-bearing molecules*, Phys. Rev. A **80**, 042508– (2009).

[51] S. Ospelkaus, K.-K. Ni, D. Wang, M. H. G. de Miranda, B. Neyenhuis, G. Quemener, P. S. Julienne, J. L. Bohn, D. S. Jin, and J. Ye, *Quantum-State Controlled Chemical Reactions of Ultracold Potassium-Rubidium Molecules*, Science **327**, 853–857 (2010).

[52] J. G. Danzl, M. J. Mark, E. Haller, M. Gustavsson, R. Hart, J. Aldegunde, J. M. Hutson, and H.-C. Nägerl, *An ultracold high-density sample of rovibronic ground-state molecules in an optical lattice*, Nucl. Phys. **6**, 265 (2009).

[53] H. P. Büchler, E. Demler, M. Lukin, A. Micheli, N. Prokof'ev, G. Pupillo, and P. Zoller, *Strongly Correlated 2D Quantum Phases with Cold Polar Molecules: Controlling the Shape of the Interaction Potential*, Phys. Rev. Lett. **98**, 060404 (2007).

[54] A. Micheli, G. K. Brennen, and P. Zoller, *A toolbox for lattice-spin models with polar molecules*, Nat Phys **2**, 341–347 (2006).

[55] L. K. Sørensen, S. Knecht, T. Fleig, and C. M. Marian, *Four-Component Relativistic Coupled Cluster and Configuration Interaction Calculations on the Ground and Excited States of the RbYb Molecule*, The Journal of Physical Chemistry A **113**, 12607–12614 (2009).

[56] H. Metcalf and P. van der Straten, *Laser Cooling and Trapping* (Springer–Verlag, New York, 1999).

[57] P. Meystre, *Atom Optics* (Springer–Verlag, New York, 2001).

[58] G. Herzberg, *Molecular Spectra and Molecular Structure, volume I. Spectra of Diatomic Molecules.* (Van Nostrand Reinhold, 1950).

[59] D. A. Steck, *Rubidium 87 D Line Data*, Los Alamos National Laboratory, http://george.ph.utexas.edu/~dsteck/alkalidata/rubidium87numbers.pdf (2003).

[60] D. R. Lide, *Handbook of Chemistry and Physics* (CRC Press, 2001), 82nd edn.

[61] S. Kroboth, *Laserkühlung von Ytterbiumatomen*, Diplomarbeit, Universität Stuttgart (2002).

[62] S. Chu, L. Hollberg, J. E. Bjorkholm, A. Cable, and A. Ashkin, *Three-Dimensional Viscous Confinement and Cooling of Atoms by Resonance Radiation Pressure*, Phys. Rev. Lett. **55**, 48 (1985).

[63] P. D. Lett, W. D. Phillips, S. L. Rolston, C. E. Tanner, R. N. Watts, and W. C. I., *Optical molasses*, J. Opt. Soc. Am. B **6**, 2084 (1989).

[64] P. Ungar, D. Weiss, S. Chu, and E. Riis, *Optical Molasses and Multilevel Atoms — Theory*, J. Opt. Soc. Am. B **6**, 2058–2071 (1989).

[65] D.S.Weiss, E.Riis, Y.Shevy, P.J.Ungar, and S.Chu, *Optical molasses and multilevel atoms: experiment*, J. Opt. Soc. Am. B **6**, 2072 (1989).

[66] E. L. Raab, M. Prentiss, A. Cable, S. Chu, and D. E. Pritchard, *Trapping of Neutral Sodium Atoms with Radiation Pressure*, Phys. Rev. Lett. **59**, 2631 (1987).

[67] C. G. Townsend, N. H. Edwards, C. J. Cooper, K. P. Zetie, C. J. Foot, A. M. Steane, P. Szriftgiser, H. Perrin, and J. Dalibard, *Phase-space density in the Magneto-Optical Trap*, Phys. Rev. A **52**, 1423–1440 (1995).

[68] C.J.Cooper, G.Hillenbrand, J.Rink, C.G.Townsend, K.Zetie, and C.J.Foot, *The Temperature of Atoms in a Magneto-optical Trap*, Europhys. Lett. **28**, 397 (1994).

[69] J. Dalibard and C. Cohen-Tannoudji, *Laser cooling below the Doppler limit by polarization gradients: simple theoretical models*, J. Opt. Soc. Am. B **6**, 2023 (1989).

[70] A. L. Migdall, J. V. Prodan, W. D. Phillips, T. H. Bergemann, and H. J. Metcalf, *First Observation of Magnetically Trapped Neutral Atoms*, Phys. Rev. Lett. **54**, 2596 (1985).

[71] T. Bergeman, G. Erez, and H. J. Metcalf, *Magnetostatic trapping fields for neutral atoms*, Phys. Rev. A **35**, 1535 (1987).

[72] D. E. Pritchard, *Cooling Neutral Atoms in a Magnetic Trap for Precision Spectroscopy*, Phys. Rev. Lett. **51**, 1336 (1983).

[73] T. Loftus, J. R. Bochinski, and T. W. Mossberg, *Magnetic trappping of ytterbium and the alkaline-earth metals*, Phys. Rev. A **66** (2002).

[74] S. Chu, J. E. Bjorkholm, A. Ashkin, and A. Cable, *Experimental Observation of Optically Trapped Atoms*, Phys. Rev. Lett. **57**, 314 (1986).

[75] R. Grimm, M. Weidemüller, and Y. B. Ovchinnikov, *Optical Dipole Traps for Neutral Atoms*, Advances in Atomic, Molecular and Optical Physics **42**, 95–170 (2000).

[76] J. Brown and A. Carrington, *Rotational Spectroscopy of Diatomic Molecules* (Cambridge University Press, 2003).

[77] M. Marinescu and H. Sadeghpour, *Long-range potentials for two-specis alkali-metal atoms*, Phys. Rev. A **59**, 390 (1999).

[78] J. E. Lennard-Jones and A. F. Devonshire, *The Interaction of Atoms and Molecules with Solid Surfaces*, Proc. Roy. Soc. London Ser. A **156**, 6 (1936).

[79] P. M. Morse, *Diatomic Molecules According to the Wave Mechanics. II. Vibrational Levels*, Phys. Rev. **34**, 57 (1929).

[80] F. Hund, *Allgemeine Quantenmechanik des Atom- und Molekelbaues*, Handbuch der Physik **24**, 561 (1933).

[81] R. Patel, N. J. A. Jones, and H. H. Fielding, *Observation of the Stark effect in $v^+ = 0$ Rydberg states of NO with a matrix-diagonalization analysis*, J. Phys. B: At. Mol. Opt. Phys. **40**, 1369 (2007).

[82] M. Madalinski, *Zweiphotonen-Photoassoziationsspektroskopie in einem Gemisch aus Ytterbium und Rubidium*, Master's thesis, Universität Düsseldorf (2011).

[83] D. Comparat, *Improved LeRoy-Bernstein near-dissociation expansion formula, and prospect for photoassociation spectroscopy*, J. Chem. Phys. **120**, 1318 (2004).

[84] M. Gilowski, C. Schubert, M. Zaiser, W. Herr, T. Wübbena, T. Wendrich, T. Müller, E. M. Rasel, and W. Ertmer, *Narrow bandwidth interference filter–stabilized diode laser systems for the manipulation of neutral atoms*, Opt. Comm. **280**, 443 (2007).

[85] L. Ricci, M. Weidemüller, T. Esslinger, A. Hemmerich, C. Zimmermann, V. Vuletic, W. König, and T. W. Hänsch, *A compact grating-stabilized diode laser system for atomic physics*, Opt. Comm. **117**, 541 (1995).

[86] W. Demtröder, *Laserspektroskopie* (Springer Verlag, Berlin, 1993).

[87] T. Walker, D. Sesko, and C. Wieman, *Collective behavior of optically trapped neutral atoms*, Phys. Rev. Lett. **64**, 408– (1990).

[88] W. Ketterle, K. B. Davis, M. A. Joffe, A. Martin, and D. E. Pritchard, *High densities of cold atoms in a dark spontaneous-force optical trap*, Phys. Rev. Lett. **70**, 2253– (1993).

[89] M. H. Anderson, W. Petrich, J. R. Ensher, and E. A. Cornell, *Reduction of light-assisted collisional loss rate from a low-pressure vapor-cell trap*, Phys. Rev. A **50**, 3597 (1994).

[90] W. Ketterle, D. Durfee, and D. Stamper-Kurn, *Making, probing and understanding Bose-Einstein condensates*, in *Proceedings of the International School of Physics - Enrico Fermi*, edited by M. Inguscio, S. Stringari, and C. Wieman, p. 67 (IOS Press, 1999).

[91] M. Madalinski, *Aufbau eines Lasersystems für die Photoassoziationsspektroskopie an YbRb*, Bachelor's Thesis, Universität Düsseldorf (2009).

[92] S. Zilio, L. Marcassa, S. Muniz, R. Horowicz, V. Bagnato, R. Napolitano, J. Weiner, and P. Julienne, *Polarization Dependence of Optical Suppression in Photoassociative Ionization Collisions in a Sodium Magneto-optic Trap*, Phys. Rev. Lett. **76**, 2033 (1996).

[93] N. Nemitz, F. Baumer, F. Münchow, S. Tassy, and A. Görlitz, *Production of heteronuclear molecules in an electronically excited state by photoassociation in a mixture of ultracold Yb and Rb*, Phys. Rev. A **79**, 061403–4 (2009).

[94] R. Napolitano, J. Weiner, C. Williams, and J. P.S., *Line Shapes of High Resolution Photoassociation Spectra of Optically Cooled Atoms*, Phys. Rev. Lett. **73**, 1352 (1994).

[95] E. R. I. Abraham, W. I. McAlexander, C. A. Sackett, and R. G. Hulet, *Spectroscopic Determination of the s-Wave Scattering Length of Lithium*, Phys. Rev. Lett. **74**, 1315 (1995).

[96] S. H. Autler and C. H. Townes, *Stark Effect in Rapidly Varying Fields*, Phys. Rev. **100**, 703– (1955).

[97] C. Cohen-Tannoudji, J. Dupont-Roc, and G. Grynberg, *Atom–Photon Interactions – Basic Processes and Applications*, Chapter VI (Wiley, New York, 1992).

[98] A. Görlitz, *Quantum Optics*, Lecture, winter term 2005.

[99] C. Cohen-Tannoudji, *Amazing Light: a volume dedicated to Charled Hard Townes on his 80th birthday*, Chapter The Autler-Townes effect revisited (Springer, 1996).

[100] F. Münchow, C. Bruni, M. Madalinski, and A. Görlitz, *Two-photon photoassociation spectroscopy of heteronuclear YbRb*, Phys. Chem. Chem. Phys. **13**, 18734 (2011).

[101] J. Bohn and P. Julienne, *Semianalytic treatment of two-color photoassociation spectroscopy and control of atoms*, Phys. Rev. A **54**, 4637 (1996).

[102] Y. N. Martinez de Escobar, P. G. Mickelson, P. Pellegrini, S. B. Nagel, A. Traverso, M. Yan, R. Côté, and T. C. Killian, *Two-photon photoassociative spectroscopy of ultracold* ^{88}Sr, Phys. Rev. A **78**, 062708 (2008).

[103] G. F. Gribakin and V. V. Flambaum, *Calculation of the scattering length in atomic collisions using the semiclassical approximation*, Phys. Rev. A **48**, 546– (1993).

[104] R. LeRoy, *Dependence of the Diatomic Constant Bv on the Long-Range Internuclear Potential*, Can. J. Phys. **50**, 953 (1972).

[105] S. E. Maxwell and E. Tiesinga, *Ultracold Rb + Yb collisions and near-threshold bound states*, in preparation (2010).

[106] B. Gao, *Quantum-defect theory of atomic collisions and molecular vibration spectra*, Phys. Rev. A **58**, 4222– (1998).

[107] X. Liu, X. Liu, Z. Zhou, P. Ding, and S. Pan, *Numerical Solution of One-Dimensional Time-Independet Schrödinger Equation by Using Symplectic Schemes*, Int. J. Quant. Chem. **79**, 343 (2000).

[108] D. Farkas, *Franck Condon Sympletic Integrator*, Yale University Physics Dept., http://www.yale.edu/demillegroup/sharedfiles/Franck%20Condon%20Symplectic%20Integrator.nb (2007).

[109] C. Chin, R. Grimm, P. Julienne, and E. Tiesinga, *Feshbach Resonances in Ultracold Gases*, Rev. Mod. Phys. **82**, 1225 (2010).

[110] A. J. Moerdijk, B. J. Verhaar, and A. Axelsson, *Resonances in ultracold collisions of Li6, Li7, and Na23*, Phys. Rev. A **51**, 4852– (1995).

[111] G. Breit and I. I. Rabi, *Measurement of Nuclear Spin*, Phys. Rev. **38**, 2082 (1931).

[112] A. Marte, T. Volz, J. Schuster, S. Dürr, G. Rempe, E. van Kempen, and B. Verhaar, *Feshbach Resonances in Rubidium 87: Precision Measurement and Analysis*, Phys. Rev. Lett. **89**, 283202 (2002).

[113] N. R. Claussen, *Dynamics of Bose-Einstein condensates near a Feshbach resonance in* ^{85}Rb, Dissertation, University of Colorado (2003).

[114] P. A. Altin, N. P. Robins, R. Poldy, J. E. Debs, D. Döring, C. Figl, and J. D. Close, *Measurement of inelastic losses in a sample of ultracold* ^{85}Rb, Phys. Rev. A **81**, 012713 (2010).

[115] S. Händel, *Experiments on ultracold quantum gases of* ^{85}Rb *and* ^{87}Rb, Dissertation, Durham University (2011).

[116] E. Timmermans, P. Tommasini, M. Hussein, and A. Kerman, *Feshbach resonances in atomic Bose-Einstein condensates*, Phys. Rep. **315**, 199 (1999).

[117] F. A. van Abeelen and B. J. Verhaar, *Time-dependent Feshbach resonace scattering and anomalous decay of a Na Bose-Einstein condensate*, Phys. Rev. Lett. **83**, 1550 (1999).

[118] F. H. Mies, E. Tiesinga, and P. S. Julienne, *Manipulation of Feshbach resonances in ultracold atomic collisions using time-dependent magnetic fields*, Phys. Rev. A **61**, 022721 (2000).

[119] C. A. Regal, C. Ticknor, J. L. Bohn, and D. S. Jin, *Creation of ultracold molecules from a Fermi gas of atoms*, Nature **424**, 47 (2003).

[120] E. Hodby, S. T. Thompson, C. A. Regal, M. Greiner, A. C. Wilson, D. S. Jin, and E. A. Cornell, *Production efficiency of ultra-cold Feshbach molecules in bosonic and fermionic systems*, Phys. Rev. Lett. **94**, 120402 (2005).

[121] S. T. Thompson, E. Hodby, and C. E. Wieman, *Ultracold molecule production via a resonant oscillating magnetic field*, Phys. Rev. Lett. **95**, 190404 (2005).

[122] T. M. Hanna, T. Köhler, and K. Burnett, *Association of molecules using a resonantly modulated magnetic field*, Phys. Rev. A **75**, 013606 (2007).

[123] J. J. Zirbel, K. K. Ni, S. Ospelkaus, T. L. Nicholson, M. L. Olson, C. E. Wieman, J. Ye, D. S. Jin, and P. S. Julienne, *Heteronuclear molecules in an optical dipole trap*, Phys. Rev. A **78**, 013416 (2008).

[124] U. Gaubatz, P. Rudecki, M. Becker, S. Schiemann, M. Külz, and K. Bergmann, *Population switching between vibrational levels in molecular beams*, Chem. Phys. Lett. **149**, 463 (1988).

[125] E. Tiemann, private communication (2012).

[126] S. Gupta, *Ultracold Atoms, Mixture, and Molecules*, Presentation at NW APS Meeting, 02 Oct 2010.

[127] M. Mudrich, S. Kraft, K. Singer, R. Grimm, A. Mosk, and M. Weidemüller, *Sympathetic Cooling with Two Atomic Species in an Optical Trap*, Phys. Rev. Lett. **88**, 253001 (2002).

[128] V. V. Flambaum, G. F. Gribakin, and C. Harabati, *Analytical calculation of cold-atom scattering*, Phys. Rev. A **59**, 1998 (1999).

[129] H. Hara, A. Takasu, Y. Yamaoka, J. M. Doyle, and Y. Takahashi, *Quantum Degenerate Mixture of Alkali and Alkaline-Earth-Like Atoms*, Phys. Rev. Lett. **106**, 205304 (2011).

[130] A. H. Hansen, A. Khramov, W. H. Dowd, A. O. Jamison, V. V. Ivanov, and S. Gupta, *Quantum degenerate mixture of ytterbium and lithium atoms*, Phys. Rev. A **84**, 011606 (2011).

Danksagung

Für das Gelingen dieser Arbeit möchte ich mich hier bei allen bedanken, die mich dabei tatkräftig unterstützt haben. Mein Dank gilt natürlich allen Mitarbeitern des Instituts für Experimentalphysik an der Uni Düsseldorf. Besonders nennen möchte ich

- Axel Görlitz, in dessen Arbeitsgruppe meine Arbeit entstanden ist. Seine offene und fachlich kompetente Art hat dieses Experiment immer weiter vorangebracht, so dass diese Arbeit überhaupt entstehen konnte. Ich bedanke mich auch für das Korrekturlesen vor der Abgabe und der Übernahme des Hauptberichts.
- Bei Herrn Prof. Dr. Dr. Carsten Müller bedanke ich mich für die Übernahme des Mitberichts.
- Bei meinen beiden Vorgängern Florian Baumer und Nils Nemitz habe ich das Experiment kennen und schätzen (und manchmal auch verfluchen) gelernt. Ich bedanke mich bei euch für die schöne Zeit mit euch im und außerhalb des Labors. Die Arbeit hat extrem viel Spaß gemacht mit euch.
- Gleiches gilt für die Mitstreiter während die hier vorgestellten Ergebnisse entstanden sind. Danke an Cristian Bruni, Maximilian Madalinski und dem zum Ende meiner Arbeit hinzugekommenen Ali Al-Masoudi. Ich bedanke mich auch dafür, dass ihr das Projekt erfolgreich weitergeführt habt während meiner Zeit in Seattle.
- Danke auch an Ralf Stephan, unser Techniker, der immer alle Fragen zu Elektronik, Technik und Aufbauten beantworten und schnell lösen kann. Ohne dich hätte alles viel viel länger gedauert.
- Die restlichen Mitglieder der Arbeitsgruppe Gregor Mura, Tobias Franzen und Charbel Abou Jaoudeh möchte ich für die netten gemeinsamen Stunden im Labor (auch wenn auf der anderen Seite des Vorhangs) und außerhalb danken.
- Für die 5 Monate, die ich am Experiment in Seattle verbringen durfte, möchte ich mich beim DAAD für die finanzielle Unterstützung und Subhadeep Gupta für die Aufnahme in seine Gruppe danken. Mein Dank gilt auch den anderen Mitgliedern Alexander Khramov, Vladyslav Ivanov, Anders Hansen, Alan Jamison und William Dowd für die schöne Zeit, die ich mit euch verbringen durfte.
- Desweiteren möchte ich all meinen Freunden, besonders Dir, Eva, für die viele Zeit außerhalb der Physik danken.
- Außerdem bedanke ich mich bei meinen Eltern, die mich während des Studiums und der Doktorarbeit immer unterstützt haben.